TVE 10 021
Examensarbete 30 hp
December 2010

Experimental study of Cu2ZnSnS4 thin films for solar cells

Hendrik Flammersberger

Institutionen för teknikvetenskaper
Department of Engineering Sciences

UPPSALA
UNIVERSITET

Teknisk- naturvetenskaplig fakultet
UTH-enheten

Besöksadress:
Ångströmlaboratoriet
Lägerhyddsvägen 1
Hus 4, Plan 0

Postadress:
Box 536
751 21 Uppsala

Telefon:
018 – 471 30 03

Telefax:
018 – 471 30 00

Hemsida:
http://www.teknat.uu.se/student

Abstract

Experimental study of Cu2ZnSnS4 thin films for solar cells

Hendrik Flammersberger

Cu2ZnSnS4 (CZTS) is a semiconductor with a direct band gap of about 1,5 eV and an absorption coefficient of 10^4 cm^-1, and is for this reason a potential thin film solar cell material. Demonstrated efficiencies of up to 6,8% as well as use of cheap and abundant elements make CZTS a promising alternative to current solar cells.
The aim of this study was to fabricate and characterize CZTS films and to evaluate their performance in complete solar cells. For the fabrication of CZTS we applied a two-step process consisting of co-sputtering of the metal or metal-sulphur precursors, and subsequent sulphurization by heating at 520°C in sulphur atmosphere using sealed quartz ampoules.
The work included a systematic comparison of the influence of composition on quality and efficiency of CZTS solar cells. For this purpose films with various metallic ratios were produced. The results show that the composition has a major impact on the efficiency of the solar cells in these experiments. Especially zinc-rich, copper-poor and tin-rich films proved to be suitable for good cells. The worst results were received for zinc-poor films. An increase in efficiency with zinc content has been reported previously and was confirmed in this study. This can be explained by segregation of different secondary phases for off-stochiometric compositions. According to the phase diagram, zinc-poor films segregate mainly copper sulfide and copper tin sulfide compounds which are conductive and therefore detrimental for the solar cell. Zinc sulfide, that is supposed to be present in the other regions of the phase diagram examined in this study, could be comparatively harmless as this secondary phase is only isolating and by this 'just' reduces the active area. This is less disadvantageous than the shunting that can be caused by copper sulfides. Contrary to the efficiency results, metal composition had no major impact on the morphology.
A comparison of the composition before and after the sulphurization revealed that metal precursors showed higher tin losses than sulphur containing precursors. A possible explanations for this was given.
Another central point of this work was the examination of the influence of sulphur in the precursor. Less need of additional sulphur in the film might lead to better material quality. This is based on the assumption that the film is subjected to less diffusion of the elements and so to less dramatic changes within the film, which might result in fewer voids and defects. However, our experiments could find only a weak trend that sulphur in the precursor increases the performance of the solar cells; concerning morphology it was observed that more compact films with smaller grains develop from metal-sulphur-precursors.
The best efficiency measured within this work was 3,2%.

Handledare: Tomas Kubart
Ämnesgranskare: Charlotte Platzer-Björkman
Examinator: Nora Maszzi
UPTEC FRIST10 021

Contents

1 Introduction 1

2 Theory 3
2.1 Solar cells . . . 4
2.1.1 Solar radiation . . . 4
2.1.2 Intrinsic, p– and n–type semiconductor . . . 4
2.1.3 Fermi energy, valence and conduction band . . . 6
2.1.4 Formation of the space charge region at the p–n–junction . . . 7
2.1.5 Currents in a diode . . . 8
2.1.6 IV characteristics of a diode . . . 9
2.1.7 The illuminated diode . . . 11
2.1.8 Equivalent circuit of a solar cell . . . 13
2.1.9 Losses in solar cells . . . 14
2.2 Thin film solar cells . . . 17
2.2.1 Device structure and fabrication techniques . . . 17
2.2.2 Possible materials . . . 19
2.3 CZTS . . . 21
2.3.1 Properties . . . 21
2.3.2 The ternary phase diagram (TPD) . . . 22
2.3.3 Secondary phases . . . 23
2.3.4 Reaction path for formation of CZTS . . . 25
2.3.5 Previous studies . . . 26
2.3.6 Aim of this study . . . 29

3 Experimental 31
3.1 Fabrication techniques . . . 31
3.1.1 Precursor deposition by sputtering . . . 31
3.1.2 Sulphurization . . . 33
3.1.3 Processing of the solar cell . . . 34
3.2 Analysis techniques . . . 35
3.2.1 Scanning Electron Microscopy (SEM) . . . 35
3.2.2 Energy Dispersive X-ray Spectroscopy (EDS/EDX) . . . 35
3.2.3 X-ray Photoelectron Spectroscopy (XPS) . . . 39
3.2.4 X-Ray Diffraction (XRD) . . . 39

3.2.5 Quantum efficiency (QE) measurements . . . 40
3.2.6 Current–voltage (IV) measurements . . . 42

4 Results and discussion 43
4.1 Sputtering of precursors . . . 43
4.1.1 Composition . . . 43
4.1.2 Structure . . . 45
4.1.3 Special settings . . . 46
4.1.4 Conclusions . . . 48
4.2 Properties of sulphurized films . . . 49
4.2.1 Data set . . . 49
4.2.2 Composition . . . 49
4.2.3 Morphology . . . 55
4.2.4 Conclusions . . . 73
4.3 Solar cells . . . 75
4.3.1 Efficiency . . . 75
4.3.2 QE measurements . . . 83
4.3.3 IV measurements . . . 89
4.3.4 Conclusions . . . 93

5 Conclusions and suggestions for future work 95

Bibliography 99

List of Abbreviations 104

List of Figures 107

List of Tables 109

A Appendix 111
A.1 Trends in photovoltaics . . . 111
A.2 XPS measurements . . . 112

1 Introduction

In recent years, climate change and a sustainable development of energy resources were put into the limelight to a greater extend. Among other things, the United Nations Framework Conventions on Climate Change[1] made the broad public aware that the finiteness of primary fossil fuels like coal and oil on the one hand, and the climate change as a result of the CO_2–emission by the use of burning those fuels on the other hand [1], lead to an indispensable change from fossil fuels to renewable energies. As there is only a certain amount of fossil fuels, there is already now an increasing trend of prices (Fig. 1.1).

Furthermore, already now the maximum of the oil production could have been reached (so called peak oil). That means, sooner or later one has to search for alternatives. At the same time, the world's energy consumption increases massively , especially in countries like China. It is also a question of equity that countries for example from the Third World

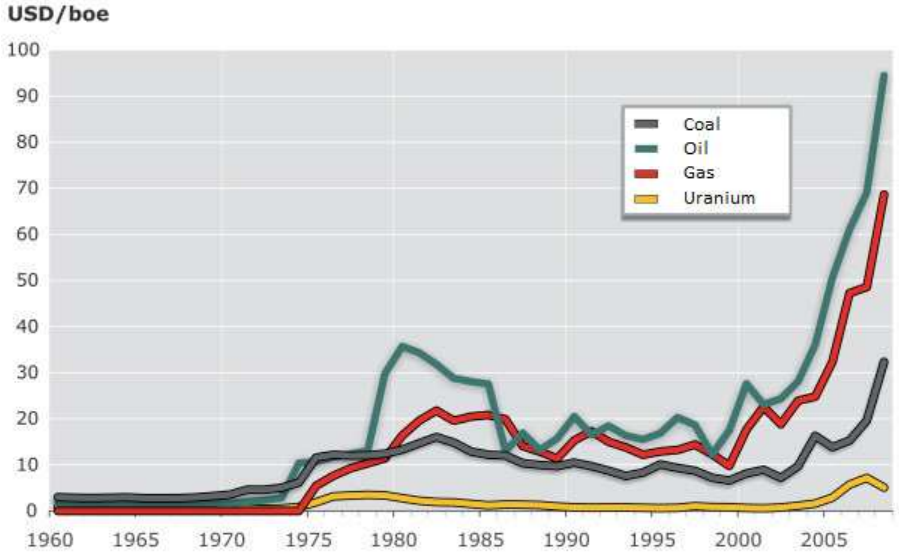

Figure 1.1: Increase of prices for the non-renewable resources coal (black line), oil (blue), natural gas (red) and uranium (yellow). Units: US-Dollar per barrel of oil equivalent (equates ca. 6 GJ). From [2].

1 Weltklimagipfel

achieve the standard of western civilization, which requires much more energy as well.

Consequently, other energy sources, that both accomplish the increasing energy consumption and present a CO_2–neutral technology, are essential. One famous CO_2–free technology is the nuclear power plant. Due to several aspects, this is not a real long term alternative. Of course, uranium – as coal, oil and every other fuel – is of limited availability. Furthermore, there is still the unsolved problem of final storage for the radioactive waste. So far, no country in the world has storage for the ultimate waste disposal of high-level radioactive waste [3]. Needless to mention the omnipresent danger of nuclear accidents.

So what is needed is real renewable energy, i.e. technologies based on energy that is inexhaustible. Thereof are available on earth geothermal energy, energy from interaction of earth and moon (tidal forces), and solar energy. The latter can be subdivided in hydropower, wind power, biomass/biofuel and photovoltaic/solar thermal power plants/solar heating systems (eventually all these forms of energy are created by the sun, i.e. solar energy).

The perhaps most promising renewable energy is solar energy, as it can potentially cover the world's energy consumption [4]. However, photovoltaics today have not yet reached so called grid parity, which means electricity from solar cells is more expensive than energy from conventional sources like coal or gas. Consequently, there is further research essential to increase the efficiency of solar cells and to make them cheaper. One approach to this is the thin film solar cell. Thin film solar cells have a thickness of only few micrometers (regarding the absorber), which means that much less material is used (saves energy and money). Further possible savings result from the easier production process, which means it is very much automatable. For example is the absorber material directly applied to the substrate (by sputtering, evaporation or the like), so that a complicated and material-consuming process like the sawing of silicon wafers from ingots can be omitted.

So far, three thin film materials have become industrially produced solar cells: Amorphous silicon (a-Si), Cadmium telluride (CdTe) and Copper-Indium-Gallium-Selenide/Sulfide (CIGS), whereof CIGS reached the highest efficiencies and can compete with polycrystalline silicon [5]. Admittedly also CIGS will have to face some difficulties. One problem is that Indium is a rare element and could run low within the next 10-20 years, while the price is already now increasing rapidly [6].

That means that further research has to be done, and one approach is the material CZTS, which is the topic of this diploma thesis. CZTS is an abbreviation for Cu_2ZnSnS_4, i.e. it is a compound semiconductor made of copper, zink, tin and sulphur, which are in each case for the time being sufficiently abundant elements, none of them harmful to the environment in the used amounts. Although it is a comparatively new material, there are already promising results that indicate that CZTS could be used as a solar cell absorber material. The world record today is 6,8% achieved by IBM [7].

The aim of this study is to fabricate Cu_2ZnSnS_4 by sputtering the metal precursor and subsequent annealing in sulphur atmosphere. The influence of parameters like metal composition or the presence of sulphur in the precursor before annealing will be studied for example regarding grain size, surface smoothness and homogeneity. At the end, applicative material will be used to fabricate complete solar cells.

2 Theory

Within the renewable energies, solar energy is the most promising. As can be seen from Fig. 2.1, the direct sunlight presents the by far biggest source of renewable energy. The technically usable potential of renewable energies is by the factor six higher than what is needed today, whereof solar energy amounts to 65%.

One of the most promising techniques are solar cells, which combine several advantages. They can be used more or less in any dimension, from the small one in a calculator up to solar power plants in the GW range. This also makes solar cells an autonomous source of energy. It is possible to cover the energy demand of small villages or street lamps at bus stops, which is especially interesting if it is not possible or too expensive to connect them to the grid. Moreover, it is a technology that is quiet, has no emissions and that has no moving parts, which makes it a technology with a quite long lifetime. Producer give guaranties of 20–25 years, but in principle much longer lifetimes are possible [8]. For this reasons, solar cells are part of a growing industry [9] (see Appendix, Fig. A.2) with a decreasing development of costs [10].

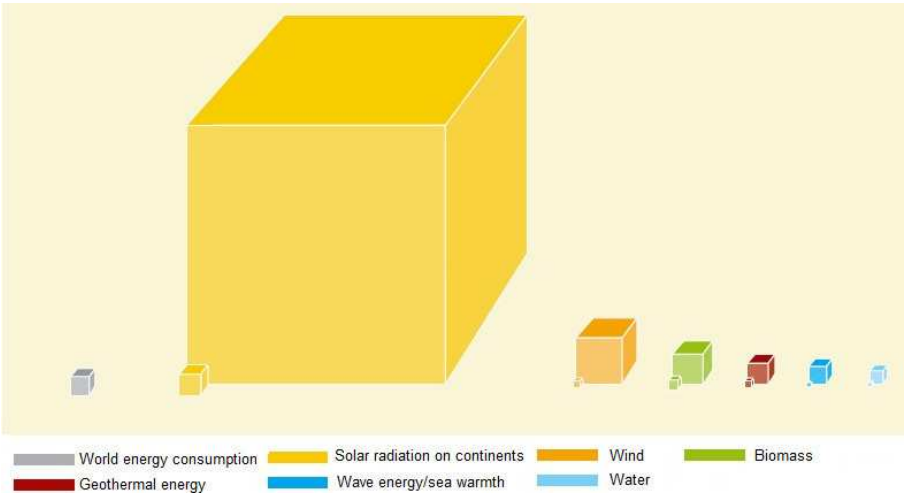

Figure 2.1: Worldwide energy demand (grey), existing (big cubes) and usable (small cubes) renewable energies. The latter includes structural and ecological restrictions, as well as limited efficiencies of the available techniques. Solar energy on its own would be enough to cover world's energy consumption. From [4].

2.1 Solar cells

Solar cells directly convert radiation into electricity. All solar cells are based on semiconductors. The radiation produces electron-hole-pairs in the semiconductor, which are segregated by a voltage. Those charge carriers can then perform work when the solar cell is connected to a load. In the following it will be explained how the needed voltage is generated, and on which principles a solar cell is based.

2.1.1 Solar radiation

The sun presents from the physical point of view a black body, which means it absorbs all kinds of radiation completely and itself emits a characteristic, temperature-dependent black body radiation. For the temperature on the surface of the sun, the spectrum looks like the orange line in Fig. 2.2. The maximum radiation intensity is around 500 nm. However, the sun is not an ideal black body, and so the spectrum that reaches the earth's atmosphere looks like the black curve. The radiation power there is 1353 $\mathrm{W/m^2}$ [11], and the radiation on earth but outside of the atmosphere is denoted with *AM0*. *AM* stands for Air Mass and indicates how far the radiation has to travel trough the atmosphere, so in this case 0. The radiation on earth's surface with perpendicular incidence of light is denoted with *AM1*. Crucial for a solar cell is of course the actual incoming light, and the standard spectrum for measurements on solar cells is *AM1,5*, which means an angle of incidence of ca. 48°. Standard test conditions (STC) used for certification of solar cells and modules is the AM1,5 spectrum with a power of 1000 $\mathrm{W/m^2}$ and cell temperature of 25°C. The AM1,5 spectrum is the lowermost, blue line in Fig. 2.2. Absorption by water, oxygen, ozone and other molecules in the atmosphere causes the peak pattern. In that way also the wavelength for the maximum photon number shifts slightly. Of course it is necessary to make optimal use of the sunlight, so that a solar cell is optimized (for example by anti-reflection coating) for its application (space, satellite, roof tops, etc.).

2.1.2 Intrinsic, p– and n–type semiconductor

In all semiconductor solar cells, the voltage occurs in the contact area of a p- and an n-type semiconductor. This shall be shown here using the example of silicon, as it is particularly good understandable here how a p- and an n-type semiconductor are formed.

Silicon is a tetravalent element. In a 2D-projection of a silicon crystal, silicon atoms form a lattice like shown in Fig. 2.3 a). Every atom has four bindings. If a silicon atom is substituted by a pentavalent atom (group V element) like phosphor or arsenic, there is one electron left that cannot form a covalent bond (Fig. 2.3 b)). This electron is only

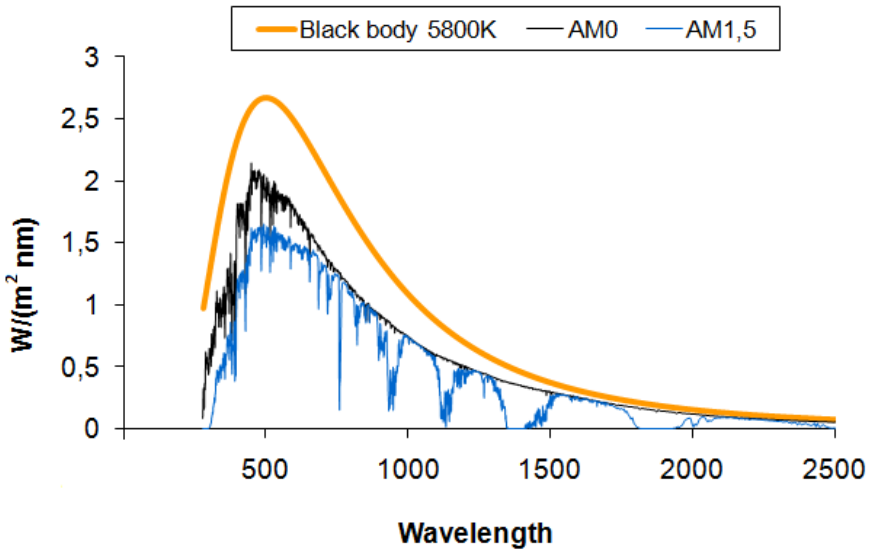

Figure 2.2: Spectral irradiance of the sun for different wavelengths. The orange line is the spectrum of a perfect black body at the temperature of the sun (5800 K), the black one is for extraterrestrial radiation from the sun (AM0), and the lowermost curve (blue) shows the sun spectrum that reaches earth under an angle of ca. 48° (AM1,5). Data from NREL [12].

very weakly bonded[1], so that it is possible to remove it from its atom with little energy, i.e. room temperature can be sufficient. If a fraction of the silicon atoms in a silicon crystal is substituted by pentavalent atoms, this is referred to as *n-type doping*. *n* stands for negative, as there are negative charges (electrons) that can be removed easily from their atoms. That is also why the doping atoms on the n-side are called *donors*. Note that the n-type doped material itself is neutral, not negatively charged!

If a silicon atom is on the other hand substituted by an element with three valence electrons, there is something called *hole*, because there is one electron missing to form four bonds (Fig. 2.3 c)). Such a trivalent atom in silicon is called *acceptor*, because it would be able to accept one more electron. If electrons move over to this vacancy, it can be treated like a positive charge because it looks like the hole moves in the opposite direction. Materials that exhibit quasi free positive charges (holes) are called *p-type doped*, because

1 Formula for energy level of an H-atom: $E = \frac{m_e \cdot e^4}{2(4\pi\varepsilon_0\hbar)^2} \cdot \frac{1}{n^2}$, with m_e: electron mass, e: elemental charge, n: shell. For n=1, the ionization energy is 13,6 eV. In this particular case, the electron mass has to be substituted by the effective mass $m^* = 0{,}3\, m_e$, because it is not a free electron but influenced by the lattice, and the dielectric coefficient of the vacuum ε_0 has to be substituted by the one of Si. From this it follows that the ionization energy is ≈ 30 meV. From [13].

of the positive hole. As for n-type semiconductors, p-type semiconductors do not exhibit excess positive charges.

If no doping is carried out the semiconductor is called *intrinsic* (Fig. 2.3 a)).

2.1.3 Fermi energy, valence and conduction band

In theory, a crystal is an infinitely continued sequence of unit cells. The infiniteness leads to some unique phenomena; one of those is the formation of bands.[1] As there are numberless amounts of energy levels in an atom, there is also a large number of bands in a crystal. Anyway, only the bands around the Fermi level are interesting.[2] All states up to the Fermi level are occupied with electrons. The highest band where electrons are present at zero temperature is called *valence band*, the next band above (empty at zero temperature) is called *conduction band* [13]. If the valence band is completely occupied, electrons cannot take up any small amount of energy, which means that no current can

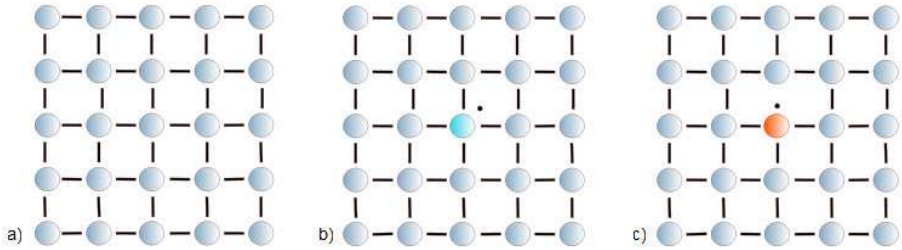

Figure 2.3: a) Intrinsic, b) n-doped and c) p-doped silicon lattice. Donors (n-type) have one an electron that does not have a partner to form a bond and which can easily be removed from the atom. Acceptors (p-type) form one bond less compared to the intrinsic case as they have too few electrons. The remaining vacancy is called hole.

1 The deeper reason for this is the following: In an atom, all electrons sit on so called energy levels, which means they cannot have just any energy when bounded to an atom. Each level can only be filled with one electron or rather with two electrons of different spin, according to Pauli Exclusion Principle that says that no two equal electrons may have the same energy (more precisely: same quantum numbers). However, in a bond of equal atoms (like it is the case in silicon), electrons on the same energy level come very near to each other, so that the energy levels have to split up slightly. In a perfect, infinite crystal, though, there are so many electrons, that all the slightly splitted energy levels form quasi continuous bands. The different bands, belonging to different energy shells, can be divided by so called *band gaps* E_g, i.e. energetic regions where electrons are not allowed to be.

2 The electrons in a crystal (like in an atom) fill up the energy levels/free states, of course beginning with the lowest. As only two Fermions (which electrons are) may occupy the same level (Pauli Exclusion Principle), higher energy levels have to be filled up as well; only two electrons can sit on the lowest level. In that way, little by little from the bottom up all energy levels are filled up until the last electron has found a place. The energy that the last electron needs to occupy a place is called *Fermi energy* or *Fermi level*.

flow. If the conduction band is 'considerably' (often means E_g more than 3 eV) apart from the valence band, this refers to an *insulator*. If valence and conduction band overlap or the valence band is occupied only partly, this is called a *conductor*. A *semiconductor* is a case in between, when a band gap between valence and conduction band is existing (at zero temperature an insulator), but it is so small that some electrons are lifted up to the conduction band at room temperature so that it is occupied with some few electrons [13].

2.1.4 Formation of the space charge region at the p–n–junction

In an intrinsic silicon crystal, only very few electrons are in the conduction band at room temperature. To increase the charge carrier density the material is doped. In n-doped material, electrons are the majority carriers, which means that at room temperature predominantly electrons carry the current. The same is the case in p-doped material for holes. Fig. 2.4 shows the band structure of a semiconductor. The red line is the Fermi level, the dashed line the doping level. For the n-side, the energy level for the doping atoms is called E_D, for the p-side E_A. The blue balls symbolize electrons in the conduction band, the purple ones holes in the valence band. To the left in a) there is an n-type semiconductor. As most electrons come from the doping level just under the conduction band, electrons represent the majority carrier (only few holes in the valence band). The Fermi level is between doping level and the conduction band as there is the highest occupied electron level at zero temperature now. The same applied to the case of p-type semiconductor in the middle (b)), with holes and valence band instead, though. To the right (c)) the intrinsic band scheme is shown, with the Fermi level in the middle of valence and conduction band. It isexactly in the middle in case of zero temperature and equal density of states.

If the n-doped and the p-doped semiconductor are interconnected – called *p-n-junction* –, the following happens: the Fermi level has to be the same everywhere in the crystal as we consider thermodynamic equilibrium. The relative position of the bands with respect to the Fermi level does of course not change. Consequently, a band bending occurs (Fig. 2.5). The deeper physical reason for this is that electrons from the n-type semiconductor move

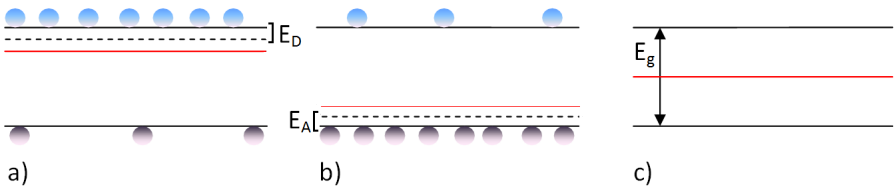

Figure 2.4: a) n-doped, b) p-doped and c) intrinsic semiconductor. The blue balls symbolize electrons in the conduction band, the purple ones holes in the valence band. The dashed lines are the doping levels, i.e. E_D for the n-doped and E_A for the p-doped semiconductor. The red line is E_F and the energy difference between valence and conduction band is E_g.

to lower energetic levels in the p-type material. By this, an electron excess in the p-type semiconductor is generated (at the same time an electron depletion in the n-type material near the contact, Fig. 2.6), which leads to a voltage that raises the bands of the p-type side. This voltage is the crucial point: It falls across the region where the ionized n-doping atoms lost their weakly bonded electrons to the p-region where the electrons ended up. This region is called the *space charge region* (SCR) or *depletion region*, as it is depleted of free carriers.

Looking at Fig. 2.5, one can directly see what happens with electrons that are generated in the p-type material and reach (by diffusion) the space charge region: they fall down the hill, or physically expressed drift in the built-in field of the space charge region. In this way the separation of charges takes place.

This electrical component is called *diode*.

2.1.5 Currents in a diode

In equilibrium there are two currents in the described system. One flows from the p- to the n-side. It is caused by electrons that are generated in the p-side and reach by diffusion the space charge region, where they feel the voltage and drift to the n-side. For this reason the current is called *drift current* or *reverse current* j_R.

On the n-side of the semiconductor, the concentration of free electrons is considerably larger than on the p-side. This difference in concentration causes a diffusion current from the n-side to the p-side and is consequently called *diffusion current* or *forward current* j_F.

As we consider equilibrium, the two currents are equal.

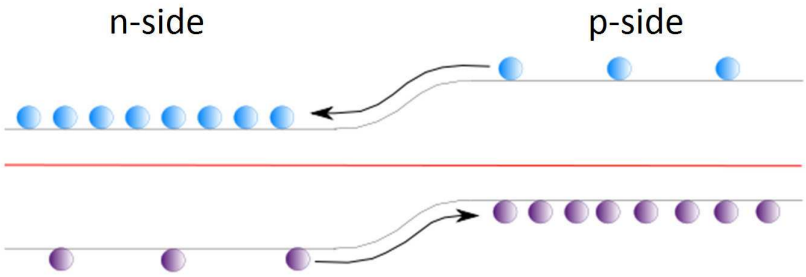

Figure 2.5: Band-bending at the p-n-junction. To the left is the n-side, to the right the p-side. Electrons (blue) on the p-side – which are minority carriers there – flow to the n-side if they reach the space charge region and feel the electric field. The same applies for the holes (purple) on the n-side.

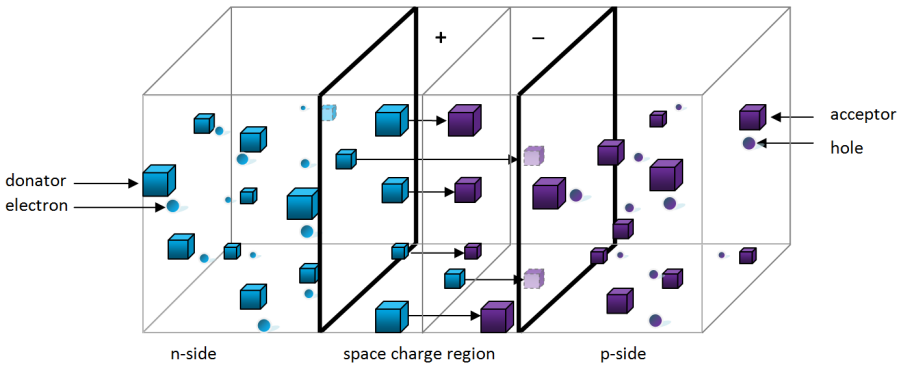

Figure 2.6: p-n-junction and space charge region. The blue cubes are positively charged donors, the blue balls electrons, the purple cubes negatively charged acceptors and the purple balls represent holes. The space charge region consists of ionized donors and acceptors, which originate from the electrons that moved from the n-side to the energetic lower levels of the acceptors at the n-side. Between the ionized atoms an electric field occurs (symbolized by arrows).

2.1.6 IV characteristics of a diode

If a voltage V is applied to a diode there is no equilibrium anymore and so a net current can flow. There are two situations possible, referring to the two possible polarities.

Situation A: The negative pole at the p-side (reverse direction)

The p-side in the space charge region already has an excess of electrons and is negatively charged (we are talking about net charges, not about the amount of electrons in the conduction band, see chapter 2.1.4). This leads to an increase of the conduction band on the p-side compared to the n-side (see Fig. 2.7 a)), namely about the value $e \cdot V$. By this, the energy barrier for the electrons on the n-side becomes even bigger, so that the diffusion current vanishes at some point. The drift current, however, is not influenced by the voltage. Electrons that reach the space charge region are attracted as before. These considerations lead to the formula

$$j\left(V_{ex}\right) = -\left(j_R\left(C\right) + j_R\left(V\right)\right) \tag{2.1}$$

(with $j(V_{ex})$: current in the diode for the voltage V_{ex}; $j_R(C)$: drift current in the **c**onduction band; $j_R(V)$: drift current in the **v**alence band).

This polarity is called *reverse direction*.

> This applied voltage leads furthermore to an increase of the space charge region, as in this situation more electrons from the n-side are pulled to the (negative) p-side. Considering Fig. 2.6, this means more positively charged donors and

negatively charged acceptors and therefore a larger space charge region. For good material this effect makes no difference for the performance of a solar cell, but for bad material with low diffusion lengths of the electrons this increases the number of collected electrons and in doing so the current, as more electrons can reach the larger SCR. This phenomenon is referred to as *voltage dependent carrier collection* and causes a deviation from the standard diode curve since an increasing (negative) voltage results in an increasing (negative) current.

Situation B: The negative pole at the n–side (forward/conducting direction)

If the negative pole is connected to the n-side, the band bending is reduced (Fig. 2.7 b)). More free electrons from the conduction band on the n-side can now diffuse to the p-side because the potential holding them back is lower. That means the diffusion/forward current j_F increases, and that exponentially:

$$j = -j_R \cdot e^{\frac{e \cdot V_{ex}}{k_B \cdot T}} \tag{2.2}$$

(with V_{ex}: applied voltage, k_B: Boltzmann-constant, T: temperature).

At the same time, the drift current is unchanged as long as some of the voltage drop between p- and n-side is left, but it becomes with increasing voltage negligible as the forward current increases exponentially. This is called *forward* or *conducting direction* of the diode.

The resulting formula, taking into account that there are both electron and hole currents, is

$$j\left(V_{ex}\right) = -\left(j_R\left(C\right) + j_R\left(V\right)\right) \cdot \left(e^{\frac{e \cdot V_{ex}}{k_B \cdot T}} - 1\right)^1 \tag{2.3}$$

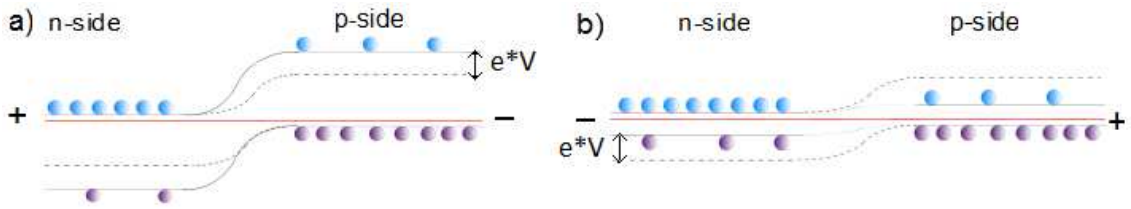

Figure 2.7: Band bending as a result of an applied voltage V. a) shows the negative pole on the p-side. The potential wall increases and the diffusion current decreases. b) Negative pole on the n-side, the barrier decreases and the diffusion current increases exponentially. The drift current is in both cases not influenced (as long as some potential gradient from the p- to the n-side is left).

($j_R(C)$: reverse current from the conduction band, $j_R(V)$: reverse current from the valence band).

The resulting curve can be seen in Fig. 2.8.

A more precise formula includes the current from the space charge region:

$$j = -\left(j_R\left(C\right) + j_R\left(V\right)\right) \cdot \left(e^{\frac{e \cdot V_{ex}}{k_B \cdot T}} - 1\right) - \left(j_R\left(C\right) + j_R\left(V\right)\right) \cdot \left(e^{\frac{e \cdot V_{ex}}{2 \cdot k_B \cdot T}} - 1\right) \tag{2.4}$$

2.1.7 The illuminated diode

Another non equilibrium situation is when the device is illuminated. The incoming light produces electron-hole-pairs. Those that are minorities (i.e. electrons in the p-type and holes in the n-type material, respectively) drift to the other side and are available as external current, if they can reach the space charge region.

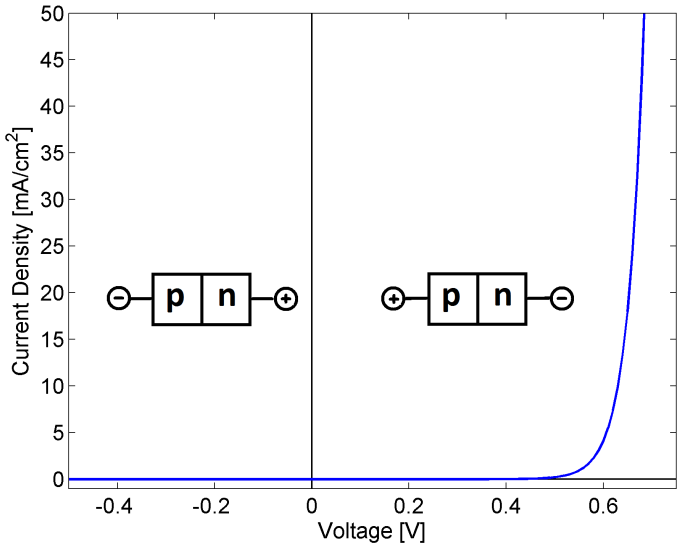

Figure 2.8: Behavior of a diode under external voltage (IV characteristics). If the negative pole is applied to the p-side only a very small drift current flows. This is the reverse direction of the diode. The opposite polarity leads to an exponential growth of the current.

1 The "-1" stands for the forward current j_F. As it is equal to j_R in equilibrium, this formula can be written like this instead of $j(V_{ex}) = -(j_R(C) + j_R(V)) \cdot e^{\frac{e \cdot V_{ex}}{k_B \cdot T}} + (j_F(C) + j_F(V))$, so that the formula looks much clearer.

That has three consequences for the final solar cell: First, the space charge region should be as wide as possible, as all charge carriers that are already in the space charge region can feel the potential and add to the current; second, the space charge region should be near the surface or rather near to where the light comes in, because much light is already absorbed near the surface; third, the diffusion length of charge carriers in the bulk has to be as large as possible (which requires good material quality, i.e. large grains, few defects...), so that many minority carriers can reach the space charge region.

The current that can be reached under illumination when the device is short-circuited is referred to as *short circuit current* I_{sc}. The theoretical maximum can be calculated as follows: assuming that all photons reaching the solar cell per second create each one electron-hole pair, this number times e (elemental charge: $1{,}6 \cdot 10^{-19}\,\mathrm{C}$) is the current that is possible without any losses. This calculation depends on the band gap, as all photons with energy below the band gap produce no electron-hole-pairs [14]. For our band gap of roughly 1,5 eV (see chapter 4.3.2.2) we assume around 22-24$\frac{mA}{cm^2}$.

If the circuit is not closed a voltage is established under illumination. This maximum voltage that is possible to achieve under illumination is referred to as *open circuit voltage* V_{oc}. The maximum V_{oc} that is theoretically possible is difficult to estimate. Note that not the whole band gap can be gained as V_{oc} but only the built in voltage of the pn-junction V_{bi}:

$$V_{bi} = q \cdot (E_g - \Delta E_D - \Delta E_A), \tag{2.5}$$

i.e. the band gap E_g minus the distance of the doping levels from the conduction (E_D) and valence band (E_A), respectively. This voltage is further reduced by recombination losses in the bulk of the semiconductor and at interfaces.

This means for the diode curve that it is shifted down by the open circuit current and intercepts the x-axis at V_{oc}. That can be seen in Fig. 2.9.

Hence, the equation for the illuminated diode is now

$$j\,(V_{ex}) = -\left(j_R\,(C) + j_R\,(V)\right) \cdot \left(e^{\frac{e \cdot V_{ex}}{k_B \cdot T}} - 1\right) - j_R\,(solar) \tag{2.6}$$

(with $j_R(solar)$: current density under illumination without voltage; i.e. $j_R(solar) \cdot A = -I_{SC}$, A: device area).

Nevertheless, the current that can be used is never I_{sc}, as a circuit needs both current and voltage. Thus, a point on the curve is searched that has the highest power (current times voltage) that is possible. This operating point is called *maximum power point*, and the associated voltage and current are V_{mp} and I_{mp}, respectively. The ratio between the theoretical power $I_{sc} \cdot V_{oc}$ and the maximal possible power is called *fill factor FF*:

$$FF = \frac{I_{mp} \cdot V_{mp}}{I_{sc} \cdot V_{oc}}. \tag{2.7}$$

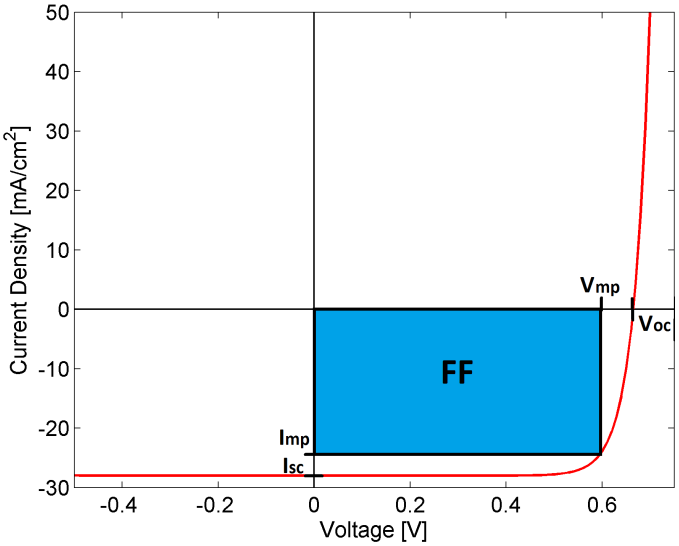

Figure 2.9: IV characteristics of an illuminated diode. The curve is shifted down by the light-induced current I_{sc} and intercepts the voltage axis at V_{oc}. The maximum power is received for I_{mp} and V_{mp}. The rectangle at this point is called fill factor FF and is aimed to be as large as possible, corresponding to the maximum power that is possible to get.

That means a fill factor as high as possible is aimed for. Graphically, the fill factor is the area of a rectangle within the IV-curve, determined by the maximum power point (which is represented by V_{mp} and I_{mp}), see Fig. 2.9. The efficiency of a solar cell, i.e. how much of the incoming light can be converted into electrical energy, is

$$\eta = \frac{P_{out}}{P_{in}} = \frac{I_{mp} \cdot V_{mp}}{P_{light}} = \frac{FF \cdot I_{sc} \cdot V_{oc}}{P_{light}} \tag{2.8}$$

(with P_{out}: gained electric power, $P_{in} = P_{light}$: incoming power in form of light). $I_{sc}, V_{oc}, I_{mp}, V_{mp}, FF$ and η are the important parameter that characterize a solar cell. FF and η are redundant, though, but allow often a quick comparison of solar cells.

2.1.8 Equivalent circuit of a solar cell

Real solar cells cannot be described by equation 2.6. The reason for that is that a real cell has resistances: the resistance of the bulk of the semiconductor material, of the contact between metal and semiconductor and of the metal contacts themselves. These resistances are in summary called *series resistance* R_S and shall be as small as possible. Furthermore, the cell can be shunted, which means that short-circuits exist across the p-n-junction in the form of defects (crystal defects, impurities and precipitates), which is characterized by the *shunt resistance* R_{SH}. This one is supposed to be as small as possible.

That is, while an ideal solar cell could be modeled by a diode in parallel with a current source, for a real solar cell a series and a shunt resistance have to be added [14]. The equivalent circuit for a solar cell looks then like in Fig. 2.10.

A further approximation to the real solar cell is the two-diode modell, but this is not discussed here.

2.1.9 Losses in solar cells

As already brought up in the last chapter, there are several losses that reduce the possible output of a solar cell or its efficiency, respectively. They are described below.

1. Optical losses

   Processes that inhibit that photons actually can produce electron-hole-pairs in the cell are summarized as optical losses. As charge carriers that are never produced cannot contribute to a current, these losses reduce the current I_{sc}.

   - *Reflection*: As long as the solar cell is not completely black, always some light is reflected. The glass that is customarily on modules reflects light as well. Reflection losses can be reduced by antireflexion coating and non-reflecting glass.
   - *Shading*: Silicon cells usually have a metal grid on the top to contact the cell. This shades the active area of the cell between 5 and 15% [14]. CIGS thin film cells do not have such a grid; they lose light by a *TCO* (*transparent conductive oxide*), though, which is not completely transparent but absorbs some light. Further area losses result from frames and interconnect zones in a module.
   - *Transmission*: Especially photons with long wavelengths can be transmitted through the absorber. All photons that have an energy lower than the band gap

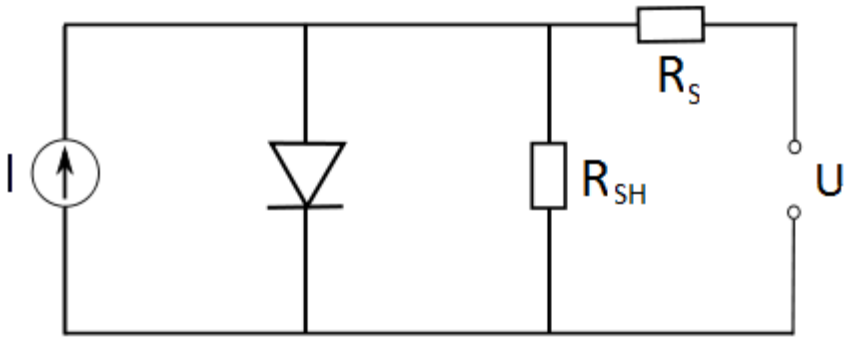

Figure 2.10: Equivalent circuit of a solar cell. It includes next to the diode and a current source I a series resistance R_S and a parallel resistance R_{SH}. According to [14].

are always lost, they cannot produce electron-hole-pairs and transmit the cell. But also light that in principle could generate charge carriers can be transmitted if the cell is too thin. The absorption coefficient is a factor that tells how strong the absorption per depth is. It is for example for CZTS $10^4\,\mathrm{cm}^{-1}$, i.e. a one centimeter thick film of CZTS reduces the intensity by the factor 10^4.

Anyway, every solar cell is wished to be as thin as possible to save material and with it costs. One solution for this is a reflecting back-contact. For silicon, aluminium is widely-used [15], for CIGS zirconium nitride (ZrN) is possible [16]. Nevertheless, thicker cells or back contacts can never completely inhibit losses, as charge carriers can only travel a certain distance before they recombine, that means they have to be able to reach the space charge region. That leads to the next loss.

2. *Recombination*

   Imperfections in the cell lead to recombination of the charge carriers, i.e. electron and hole recombine and send out a photon. Those charge carriers are then lost for the current, which means that this effect also reduces I_{sc}. But it also has a big influence on the voltage V_{oc} which is the higher the lower the recombination is.

   Recombination can occur at so called traps, which means impurity atoms like iron. They simplify the recombination process as it is more likely for an electron to loose its energy in small portions than completely at once. Especially traps in the middle of the band gap (which are e.g. for silicon: copper, iron and gold [15]) are very bad for a solar cell. Further recombination centers are crystal defects like grain boundaries.

   Recombination in the depletion region reduces also the fill factor.

3. *Thermalization*

   Photons that exhibit energy higher than the band gap can nevertheless only produce one electron-hole-pair. The excess energy is lost by thermalization, which means that the created electron in the conduction band emits photons that only heat up the device. Impact ionization, that is that one of the emitted photons creates a second or even more electron-hole-pairs, is negligible.

   Thermalization and Transmission (see point 1. Optical losses) present an optimization problem. On the one hand, the band gap should be as high as possible, to reduce thermalization. On the other hand, a low band gap would be desirable to collect as many photons as possible witout loosing them by transmission. The optimum band gap is somewhere around 1,4-1,5 eV, which would allow a theoretical efficiency of around 30% [14]. The only possibility to avoid this problem is a multijunction cell, i.e. several cells with different band gaps stacked.

4. *Electrical losses*

   As mentioned in the last chapter, series resistance R_S (which results from the internal resistance of the used materials) and shunt resistance R_{SH} (which results from short circuits across the p-n-junction) decrease the efficiency of a cell. At a series resistance the voltage drops. The parallel resistance results in a reduction of the FF since the diode curve is influenced by an ohmic resistance in parallel. For very low R_{SH} there is also a loss in V_{oc} (see Fig. 2.11).

   As can be seen from Fig. 2.11, the fill factor is reduced by both resistances.

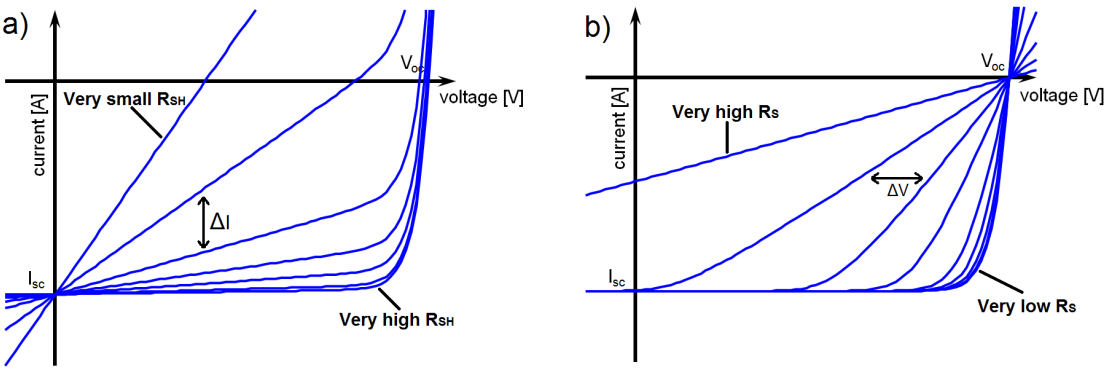

Figure 2.11: Impact of a) R_{SH} and b) R_S on the diode curve. a) If a diode is shunted, the current can partly flow back within the diode, i.e. this resistance lowers I: $\Delta I = V/R_{SH}$. If the diode is (almost) completely shunted it is a ohmic resistance. This means also a drop of the V_{oc}. b) At a series resistance the voltage drops: $\Delta V = I \cdot R_S$. The voltage drop for currents smaller than I_{sc} leads to more linear IV-curves. In cases of very large series resistances, I_{sc} can be reduced.
In both cases the loss of the rectangular form of the diode curve results in a loss of the FF. Figure according to [17].

2.2 Thin film solar cells

All the advantages of solar cells should not hide the fact that there are still some issues that have to be worked on. Like wind power, photovoltaics base on an inconstant energy supply, which poses the problem of energy storage. Furthermore, so far solar electricity is more expensive than conventional produced electricity. There is until today no so called grid parity [15]. To solve the latter problem, solar cells have to become cheaper to shorten the economical payback period and make electricity cheaper. One approach is to use less material, which leads to thin film solar cells. Compared to crystalline silicon solar cells, much less material is expended. While crystalline silicon needs $200\,\mathrm{cm}^3$ ($200\,\mu\mathrm{m} \cdot 1\mathrm{m} \cdot 1\mathrm{m}$) material for $1\,\mathrm{m}^2$ solar cell, only $1\,\mathrm{cm}^3$ is needed for thin film material (the production of the pure feedstock requires the main part of energy consumption during the production process of a solar cell). Furthermore, silicon has losses of more than 50% of the material when it is sawn from the ingots [15].[1]

Another advantage of thin film solar cells is the monolithic integration. That means that the serial connection of the cells in a module (which is always necessary because of the low voltage in one cell) is directly done during the fabrication of the cells and does not need an individual production step, saving money and time.

One more advantage is that it is possible to adjust the band gap in some materials like CIGS ($\mathrm{CuInGaS(e)_2}$) by varying the composition. By this, the solar spectrum can be utilized much better and a higher efficiency can be reached, because the theoretical possible efficiencies depend strongly on the band gap, as can be seen from Fig. 2.12.

As thin film solar cells today can compete in efficiency at least with polycrystalline silicon (20,4% efficiency for multicrystalline Si and 19,4% for CIGS, [5]), the proportion of thin films of the whole photovoltaic module production is increasing [9].

2.2.1 Device structure and fabrication techniques

In spite of the differences of the various semiconductor materials, many thin film solar cells have a similar device structure, which shall be shown here with CIGS as an example. Fig. 2.13 shows a cross section of a basic CIGS solar cell as described below.

As thin film solar cells are so thin and to protect the back side, they have to be deposited on a *substrate*. One advantage of the thin films is that they can be deposited on flexible materials like metal foils or polimides (plastic), which allows completely new applications. Anyway, still the most common substrate is glass.

On the substrate, some kind of *back contact* is needed. The demands for a back contact are good conductivity, a good work function and stability against corrosion, oxidation etc..

1 Mass yield ingot to column: 70%, mass yield column to wafer: 60%. ⇒ ca. 58% loss. Indeed do thin film techniques have losses in the order of 50% as well, as not only the substrates are coated but also the surrounding area, but this is as well 50% of $2\,\mathrm{cm}^3$ compared to 50% of $400\,\mathrm{cm}^3$. In both cases, the material can quite easy be recycled.

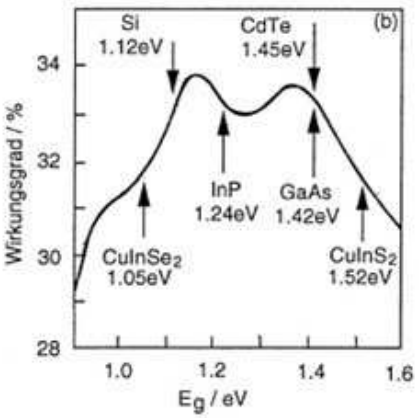

Figure 2.12: Theoretical efficiencies of solar cells for different band gaps. One maximum is around 1,4 eV. Band gaps of different solar cell materials are marked. From [18].

For CIGS, molybdenum has proven suitable. The thickness is about half a micrometer and the molybdenum is commonly sputtered on the glass.

On top of the back contact follows the most important part of a solar cell, the *absorber*, where the main part of the electron-hole-pair production takes place. It is eponymous for a solar cell. Both CdTe and CIGS are p-doped, the latter by intrinsic defects and not by extrinsic doping like in Si. Various techniques are possible to deposit the material: (co-)evaporation, (reactive) sputtering, CVD (chemical vapor deposition) and several more [18]. For CIGS, co-evaporation of the four components (Cu, In, Ga, S/Se) is perhaps the most prevalent method. Other methods like sputtering require after the deposition a second step called sulphurization/selenization, to form the final material from the metal precursor. The final absorber has a thickness of about 2–4 µm.

On the absorber often follows some kind of *buffer layer*. It can have several functions, for example improving the lattice matching between the absorber and the n-doped-layer on the top. For CIGS, the buffer layers are cadmium sulfide (CdS; n-type buffer layer) and intrinsic zinc oxide (i-ZnO); the reason for improved performance by adding these layers is nevertheless not yet completely understood [19]. CdS is normally deposited by chemical bath deposition (CBD) and has a thickness of ca. 50 nm; ZnO with an approximately double thickness of 100 nm can again be sputtered.

The buffer layer(s) are then capped by the n-layer. This is done to form the p-n-junction, but at the same time it is used in CIGS, CdTe and a-Si cells to carry away the charge carriers, while they are not allowed to absorb to much of the incoming light. This layer is mostly a *TCO* (*transparent conducting oxide*), a so called window layer. The name results from the transmissibility for visible light. In case of CIGS this is done with heavily Al-doped ZnO (ZnO:Al), band gap $\approx 3{,}3$ eV [18]); the heavy doping provides the needed good conductivity. The ca. 300–500 nm thick layer can be deposited by sputtering.

For further improvement, an *anti-reflection coating* is possible, to increase the amount of incoming light. Moreover, a *reflecting back contact* (as described in chapter 2.1.9) could be added to have less loss by transmission. Fig. 2.13 a) shows a cross section of a basic CIGS solar cell as described above, in b) a cross section of a CZTS film can be seen.

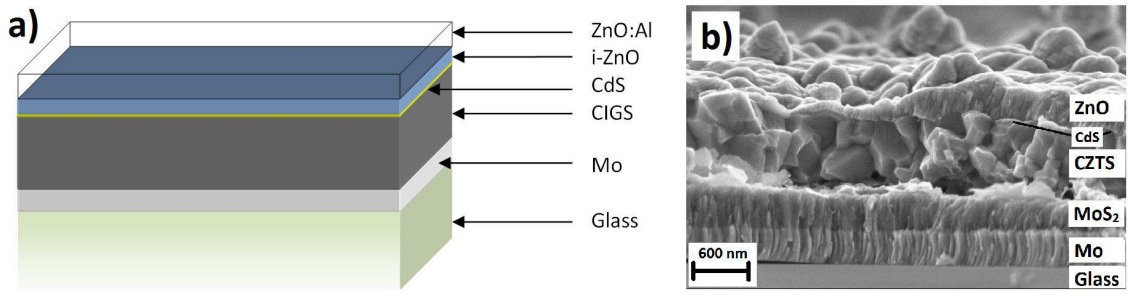

Figure 2.13: a) Cross section of a typical CIGS solar cell with the different layers (schematic). b) SEM cross section of a CZTS film.

2.2.2 Possible materials

Material for thin film solar cells has to fulfill some important conditions to be usable. An essential precondition is of course a large absorption coefficient, as all (suitable) light should be absorbed in only a few micrometers. Furthermore, the band gap should be in the range of roughly 1–1,6 eV (see Fig. 2.12) to provide the theoretical opportunity to reach sufficient efficiencies. Anyway, quite a lot materials fulfill these conditions (see Fig. 2.14). On the basis of silicon, one can deduce at first the III–V– (like GaAs) and II–VI–semiconductors (like CdTe) [18]. Further compound semiconductor can be formed by substituting in the latter one half of the group-II element with a group-I and one half with a group-III element. A common example for such an I–III–VI-compound semiconductor is CIS ($CuInS_2$) or – replacing partly the Indium by Gallium to modify the band gap – CIGS ($CuInGaS_2$/$CuInGaSe_2$). Various more substitutions are possible, for example replacing half of the group-III element with a group-II element and half with a group-IV element. For CIGS, substituting In/Ga with Zn and Sn, this leads to **CZTS** (Cu_2ZnSnS_4).

Nevertheless, not all thinkable compounds give viable solar cell materials. A lot more conditions have to be fulfilled, like availability, producibility in industrial scale, costs and environmental safety (e.g. toxicity). Thus only few materials actually made the step from an interesting semiconductor to a solar cell ready for the broad market: amorphous silicon (a-Si), cadmium telluride (CdTe) and copper indium (gallium) sulfide or selenide, respectively, (CIGS).

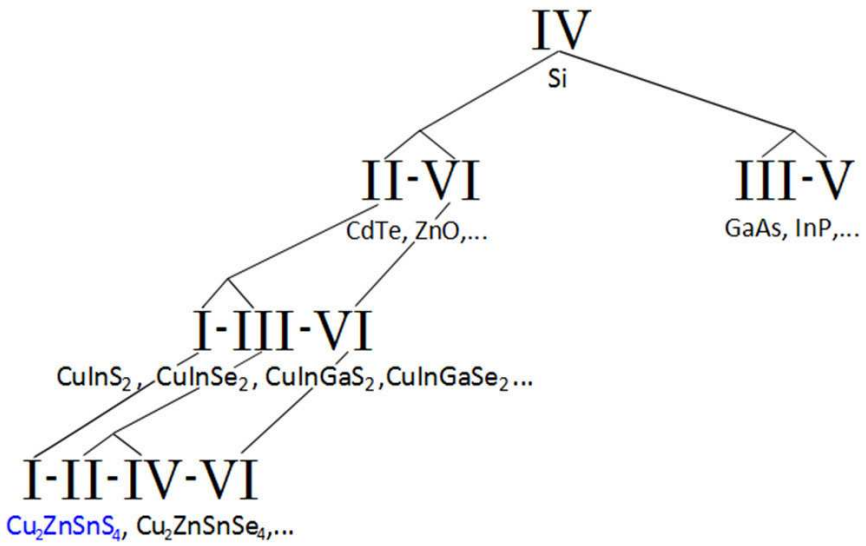

Figure 2.14: Various possible compound semiconductors, obtained by gradual substitution of elements by elements of groups from higher and lower group numbers. According to [18].

CIGS is at the moment the industrial used thin film material with the highest efficiency and can compete with multicrystalline silicon [5]. The production technique is a bit more difficult than for CdTe, but still cheaper and less material consuming than for silicon. But although only little material is used, availability of needed material could become one of the big problems for CIGS thin film solar cells. Especially indium will run low within the next years. The consumption is already now higher than the production, which cannot just be increased because it is only a by-product of zinc mining. According to estimates there are reserves for 6 years and resources for approximately 15 years [6]. In this context the price for indium increased massively, for example about 463% from 2001 to 2004 [6]. Of course the present situation will be intensified in future by the fact that other industries use those resources as well; just as an example, indium is very much used in flat screens (ITO, Indium Tin Oxides).

The named problems of the current thin film solar cell materials indicate that further research has to be done, and one approach is the material *CZTS*. CZTS is a compound semiconductor made of **c**opper, **z**ink, **t**in and **s**ulphur, which are in each case for the time being sufficiently abundant elements, none of them harmful to the environment in the used amounts. Although it is a comparatively new material, there are already promising results that indicate that CZTS could be used as a solar cell absorber material. The next chapter deals with the theoretical foundations of CZTS.

2.3 CZTS

2.3.1 Properties

Cu_2ZnSnS_4 (CZTS) is a p-type semiconductor with a direct band gap of approximately 1,5 eV. It is suitable for thin film solar cells due to its high absorption coefficient of more than $10^4\,cm^{-1}$ [1] [20].

As mentioned before, CZTS is derived from the CIGS structure by the isoelectronic substitution of two In (or Ga, respectively) atoms by one Zn and one Sn atom. As a consequence, CZTS has some similar properties as CIGS. One main advantage of this is that the standard device structure of the solar cells, shown in Fig. 2.13, can be adopted. Of course it is not sure that the combination of CZTS with CdS and ZnO yields the best results that are possible for this absorber material, but it allows starting directly without spending too much time in searching for a working device structure. Instead one can concentrate on the properties of CZTS and leave subtleties of the solar cell structure for future work.

The crystal structure of CZTS is shown in Fig. 2.15. It is referred to as *kesterite* (space group $I\overline{4}$) and can be derived from the sphalerite[2] structure by duplicating the unit cell. The kesterite structure was found to be the most stable phase of CZTS [21]. The lattice constants for CZTS are a = 0,54 nm and c = 1,09 nm [22]; from that one can calculate with the atomic masses of Cu, Zn, Sn and S [23] the density of CZTS, which is $\approx 4{,}6\,\frac{g}{cm^3}$.

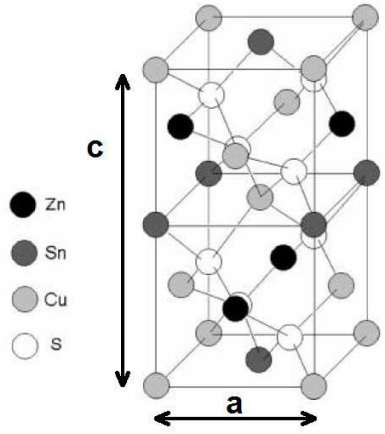

Figure 2.15: Kesterite structure in which CZTS crystallizes. It is derived from the sphalerite structure by duplicating the unit cell. From [24].

1 That means, for example, that a CZTS film with a thickness of 1 µm absorbs 99% of the incoming light.
2 Zinkblende

The doping of this material occurs by internal defects. Cu-atoms sitting on the places of Zn atoms (Cu on Zn antisite) causes p-conductivity [25]. That means that one would not necessarily aim for stoichiometric CZTS. Small deviations from stoichiometry lead also to the formation of secondary phases, though. Which secondary phases may develop can be seen from a phase diagram. It shows the phases that can be present in equilibrium for certain temperatures and material contents.

2.3.2 The ternary phase diagram (TPD)

Such a phase diagram is of course possible for CZTS as well, but since it consists of four kinds of atoms this would need a three dimensional diagram. However, one can assume that always the right amount of sulphur is in the film as the sulphur is introduced by the reactions with the metals and therefore depends on how much of those are present. This assumption will be supported by our measurements where all of our samples contained $\approx 50\%$ sulphur.

This reduces the degrees of freedom of the system to three and the phase diagram can be simplified to a ternary phase diagram (TPD). In this study the TPD developed by Scragg [26] on the basis of comprehensive measurements done by Olekseyuk et al. [27] is used. It should be noted that this phase diagram is valid in equilibrium at 400°C. Both is strictly speaking not the case for the experiments performed in this work. Anyhow, as the sulphurization process used in this work comprised very slow ramping ($< 0{,}15\,°\mathrm{C/s}$) and a long dwell time (2h at 520°C) we assume to have a quasi-equilibrium. Furthermore, other experiments at comparable conditions (e.g. [28]) obtained secondary phases that are predicted by this phase diagram. Therefore we will use it on a number of occasions, mostly just to depict the compositions of the samples (i.e. not taking into account any precondition except of having the right amount of sulphur), but partly also to support or deduce assumptions concerning composition and secondary phases.

The ternary phase diagram is shown in Fig. 2.16. As can be seen from the scale this is only a part of the whole diagram. In order to provide a better overview and as no samples with a metallic ratio outside this section were produced, it will always be shown a zoomed in version.

There are ten fields drawn in the phase diagram. Each field means the presence of CZTS plus the one or two secondary phases that are noted. The eleventh region quite in the middle (marked with an asterisk) means that only CZTS is supposed to be existing. All secondary phases contain sulphur. As a sufficient amount of sulphur is provided during the sulphurization process it is assumed that no metallic phases form but only sulfides. However, not all secondary phases that have been found in the diverse studies have been found by Olekseyuk, probably due to different conditions. One important secondary phase that will play a role in this work as well is SnS_2. It was for example found by Schurr et al. [29] and could be found for films with Sn excess.

Talking about regions in the phase diagram it is very helpful to divide it into regions that are labeled in an unambiguous way and that already indicates which secondary phases

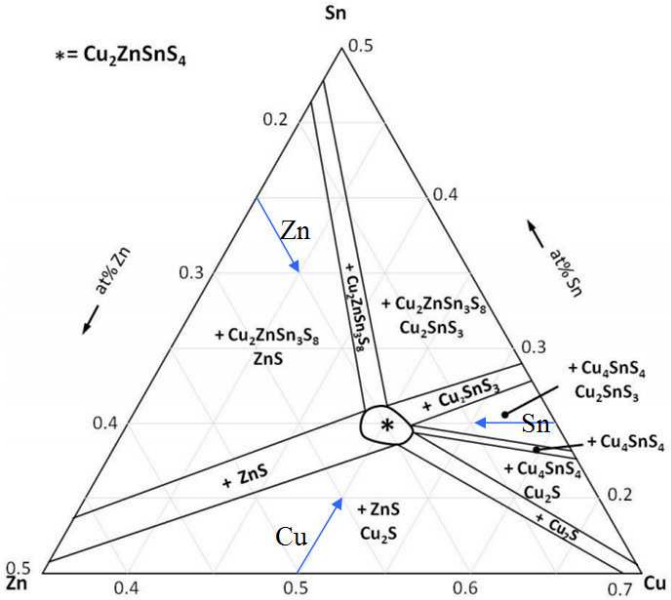

Figure 2.16: Ternary phase diagram of CZTS. A fraction of 50% sulphur is assumed. In the different regions indicated in the phase diagram, secondary phases appearing next to CZTS are given. In the middle (marked with an asterisk) only pure CZTS occurs. Blue arrows indicate lines of constant Zn, Sn or Cu ratio, respectively, in this case chosen for the ratios that mean stoichiometry. According to [26].

can be expected. This shall be done according to the notation of Scragg (Fig. 2.17). In the Zn-rich region, for example, ZnS is the expected (main) secondary phase formed by the excess Zn. The Zn-poor region covers several fields with various possible secondary phases. It should be noted that this notation is very clear, but different to the notations used in most publications, where for example only Cu-poor and Cu-rich are distinguished (e.g. [29]), not taking into account the ratio between the remaining metals.[1]

2.3.3 Secondary phases

As secondary phases can of course – depending on their fraction – have a big impact on the characteristics of the cell, the most relevant for this thesis shall be specified in the following.

1 Example: Schurr [29] describes a film with the ratios Cu/(Zn+Sn)=0,9 and Cu/Sn=2 as 'Cu-poor'. Indeed this sample contains an excess of Zn, while the Cu/Sn ratio is stoichiometric. This is why this sample would according to Scragg be referred to as 'Zn-rich', and this is how it will be done in this work as well.

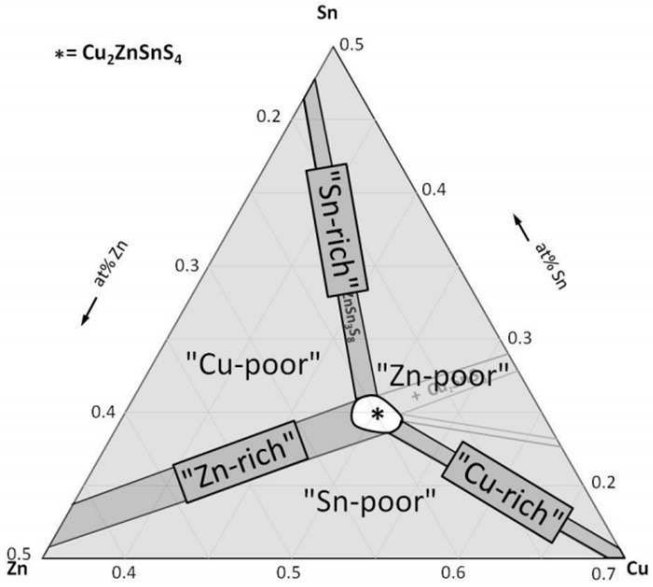

Figure 2.17: Ternary phase diagram with different regions of composition. The labeling is done according to Scragg [26].

2.3.3.1 $Cu_{(2)}S$

Copper sulfides can be expected in the Cu-rich as well as in the Sn- and Zn-poor region. These secondary phases are metals, or semiconductors that are heavily doped by intrinsic defects so that they act as metals ([30], [31]). The major hazard of $Cu_{(2)}S$ is that it shunts the cell, meaning that front and back contact are connected within the cell so that the current cannot be used for an external load. However, the copper sulfide has not to have grains reaching through the whole cell to reduce the performance significantly. Conducting phases within a solar cell can present a serious problem as they enhance recombination.

2.3.3.2 SnS_2

Tin sulfide (SnS_2) is a n-type semiconductor with a band gap of 2,2 eV [32]. This secondary phase could work as an insulator, but if existing in larger amounts it is also possible that it forms a second diode with opposite polarity to CZTS, which would act as a barrier to carrier collection and reduce the fill factor.

SnS_2 is not noted in the TPD but could be found in films with Sn-excess, i.e. especially for Sn-rich and Cu-poor (and partly for Zn-poor) samples in the TPD.

As Weber found out [28] do tin sulfides due to their high vapour pressure evaporate from CZTS films during sulphurization if they are not prevented from that (for example by being covered by other phases).

2.3.3.3 ZnS

Zinc sulfide is a secondary phase in the Sn- and Cu-poor as well as in the Zn-rich region. Due to the high band gap this material could even be called insulator (3,54 eV), and this means that the presence of ZnS can both reduce the active area (i.e. the area where electron-hole-pairs are produced) and inhibit the current conduction in the absorber.

It crystallizes in the sphalerite and the wurtzite structure and presents in both cases a semiconductor with a wide band gap of 3,54 or 3,68 eV, respectively [23]. As mentioned before is the crystal structure very similar to the CZTS one. CZTS, as the compound CTS (Cu_2SnS_3), is a superlattice to sphalerite. This results in a serious problem concerning XRD measurements, which are one analyzing method in this thesis. Actually, ZnS, CTS and CZTS are not possible to distinguish by XRD, they are therefore in literature commonly summarizing referred to as Σ–signal. Indeed do CZTS and CTS have an additional peak compared to ZnS, but that means that ZnS as well as CTS can never be excluded to be present only from XRD measurements. Only a look on the phase diagram might give a hint which secondary phase is more likely; ZnS and CTS do not appear in the same region of the phase diagram together but ZnS for Zn-rich/Cu-poor and CTS for Zn-poor compositions.

2.3.3.4 CTS

Cu_2SnS_3 (CTS) is a secondary phase that should according to the TPD appear for Zn-poor phases. CTS shows metallic properties [33] which makes it like copper sulfides a very detrimental secondary phase. As mentioned before can CTS in our experiments never be proven or excluded, as XRD is our only method to identify secondary phases. It is only possible to assume that CTS can be avoided by producing films that are further away from being Zn-poor.

The phases $Cu_2ZnSn_3S_8$ and Cu_4SnS_4 are not discussed here. The former was not reported besides the studies of Olekseyuk, the latter is supposed to be found only in regions of the phase diagram where we did not produce any samples.

Summing up one can state that $Cu_{(2)}S$ and CTS would probably be the most detrimental phases, while ZnS and SnS_2 might be less harmful. However, CTS and ZnS will in our study never be proven or excluded for sure.

2.3.4 Reaction path for formation of CZTS

Even though several experiments have been made on the reaction paths for CZTS (e.g. [29], [26], [28]), for example by in-situ XRD, there is not one universally valid reaction path known. First, all studies were done with different precursors and sulphurization conditions. Second, as mentioned phases like CZTS, CTS and ZnS are hard to distinguish, even if several analyzing methods are combined. Third, there are procedural uncertainties, like the assumption that the situation can be "frozen" by rapid cooling and that the phases present at a certain temperature can be analysed in the cooled state [26].

What they have in common is, however, that the reaction path starts with the elements (or the compounds like ZnS) in the precursor, via formation of binary compounds (Cu_6Sn_5, SnS_2, ZnS, $Cu_{(2)}S$, Cu_5Zn_8, etc.) to more complex compounds like CTS and CZTS. Due to the very similar crystal structure it is plausible that the final CZTS is formed of ZnS and CTS ([28], [29]). The reaction path requires of course the interdiffusion of all elements, which depending on the precursor type is not always given from the beginning.

Another interesting aspect that could be shown is the diffusion of Cu to the surface [34]. As Cu has a high diffusion rate, especially compared to sulphur [26], it does more or less completely diffuse to the surface to form copper sulfides. This phenomenon means also that copper sulfides are often found at the surface and can be removed by etching [26]. The major problem is, however, that this process forms voids that are left by the Cu atoms, even if the copper sulfides in a later stage react with the remaining phases to CZTS.

To tackle this problem, one approach is the integration of sulphur already in the precursor. As the reason for the Cu diffusion to the surface is the affinity of Cu to react with sulphur, this issue can be alleviated if the Cu can at least partly react with sulphur in the bulk directly from the beginning. The consequence would be less diffusion of the elements and hence less dramatically changes within the film. Another beneficial effect associated would be less expansion of the film due to less diffusion of sulphur into the film. Considering that the film expands by a factor of more than two ([35]) and a lot of stresses and cracks can occur during this, the sulphur in the precursor from the beginning could lead to a more homogeneous growth of CZTS and in doing so to bigger grains and less voids. Katagiri [36] could in this way improve grain size, uniformity and adhesion of the film substantially. The best CZTS solar cells published until today included S in the precursor ([7], [37]).

The above described means that phases in and composition of the final film depend on the precursor and the sulphurization process. According to the degree of diffusion of the elements, the content of sulphur and several more aspects, the formation of CZTS might be slower or faster and in doing so allow more or less loss of elements/secondary phases by evaporation as well as influence the segregation of secondary phases (e.g. as conglomerates).

A hypothesis about a possible reaction path for these experiments is derived in the analysis part of this thesis.

2.3.5 Previous studies

In recent years the number of publications on CZTS rose. This is accompanied with an increase of the best efficiency that could be found for this material. The current record is 6,8% by IBM [7]. The years before, Katagiris group dominated the progress for CZTS and hold the world record with 6,7% [37]. Fig. 2.18 shows the development of efficiencies for CZTS. It should be noted that the graph contains all fabrication methods, and for this reason the efficiencies spread a lot. Besides that a clear trend to better efficiencies is obvious.

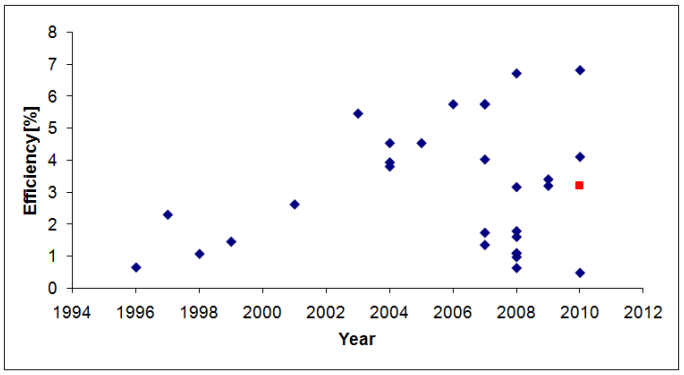

Figure 2.18: Development of the efficiencies published for CZTS. The red point shows the highest efficiency measured in this study. Note that the graph shows only publications were an efficiency was given, the total number of published CZTS related papers was higher.

There are various methods for fabrication of CZTS. Some produce directly CZTS (so called single-stage processes, like thermal evaporation), but most processes use two steps: First, the fabrication of what is referred to as *precursor* is done, a film that contains only the metals or metals plus some amount of sulphur. The deposition of the precursor can be performed by any physical or chemical method (see Table 2.1 for a list of several methods including the maximum efficiency reached with this method so far). The elements can be deposited as stacked layers (i.e. for example one layer of Cu, one of Zn and one of Sn) or for all elements at the same time. The latter is indicated with a "co-", for example "co-sputtering" where all elements that are supposed to be in the precursor are sputtered at the same time and are hence alloyed.

The second step is the *sulphurization*, a process where the sample is annealed to temperatures mostly in the region of 500°C in an atmosphere containing sulphur. This can be elemental sulphur or for example H_2S.

The so far highest efficiencies were reached by a two-step-process with co-deposition of the precursor: co-evaporation (6,8%) and co-sputtering (6,7%). This might be due to the formation of stable alloy phases instead of losses by evaporation of elements/compounds (see chapter 2.3.4). For this reason such a process (co-sputtering) was used for this work.

Next to the deposition method, manifold more aspects were studied (examples without reference will be discussed in more detail below): The order of the layers in stacked precursors [38], the influence of sulphur in the precursor, the composition of the precursor, the sulphurization process (temperature, ramping, dwell time, pre-annealing,...), in-situ measurements to reveal the reactions during sulphurizations [29], etching to remove secondary phases from the CZTS film, and some more. The most important results shall be briefly mentioned.

Electrochemical deposition	3,4% [39]
Sol-gel	1,6% [40]
Evaporation	5,5% [41]
Thermally co-evaporated	6,8% [7]
Co-Sputtering	6,7% [37]

Table 2.1: Some common deposition methods for CZTS and their reached maximum efficiency.

- Katagiri's group studied among other things the influence of the temperature [42]. The optimum temperature turned out to be 520°C.
- The composition of the films was subject to several studies. However, most concentrated only on the influence of Cu and gave as a result that films with Cu deficiency gave the best results concerning efficiency and optoelectronic properties ([42], [43]).
- Grain size appears to be related to the Cu-content. Tanaka et al. [44] found increasing grain size with increasing Cu/(Zn+Sn) ratio. This is related to the results that were found for CIGS where the beneficial influence of Cu on grain size is well known (see for example [45]).
- Copper sulfides that appear as secondary phases for films with Cu-excess could be removed by KCN etching. However, this process can instead lead to undesirable voids ([35], [34]).
- Loss of elements: Both loss of Zn and Sn (by evaporation, elemental or as secondary phases) could be observed as a consequence of the sulphurization process ([42], [46]).
- The presence of sulphur already in the precursor showed beneficial effects on the CZTS films. An increase in grain size, better adhesion to the substrate and smoother films could be shown [42].
- Films with Zn excess and Cu deficiency (Cu/(Zn+Sn) $\approx$ 0,85, Zn/Sn $\approx$ 1,1–1,2) gave so far the best results (see for example [37]).

  It is worth to note that efficiencies up to almost 10% could be reached for CZTS where a certain amount of selenium was added [47]. However, as this approach is not part of this study it will not be discussed here any further.

2.3.6 Aim of this study

The results of previous studies were of course considered in this work. We used the process that showed so far the most promising results, namely co-sputtering[1], and used sulphurization temperatures of 520°C. No precursors from the Cu-rich region of the phase diagram were used to make films for solar cells.

This diploma work was supposed to explore the potential of CZTS as a new absorber material for thin film solar cells and to establish CZTS in this group that so far concentrated on CIGS devices. This included both the determination of sputter conditions that allow a control of the precursor composition, as well as to find and arrange a way to sulphurize these precursors. For the further processing of the solar cell the standard process for CIGS solar cells was applied.

With regards to the content the main intentions of this work were to analyse the following two aspects:

- Influence of sulphur in the precursor: one series with precursors that only contained metals (referred to as *metal-* or *metallic precursors*) and one series with precursors that had an additional content of sulphur (referred to as *ZnS precursors*) were performed and compared.
- Influence of the composition: we studied films from 6 of the 7 regions of the phase diagram (including stoichiometric). This shall give deeper insights which composition is best and complement previous studies that mostly concentrated on the influence of only one element (e.g. Cu-poor vs. Cu-rich films, [29]).

For analysis of the films scanning electron microscopy (used for: analysis of morphology), energy dispersive X-ray spectroscopy (determination of composition), X-ray diffraction (identification of crystalline phases) and X-ray photoelectron spectroscopy (compositional gradients) were used. Further analysis of the solar cells included IV (current + voltage) and quantum efficiency measurements (determination of possible losses).

1 The slightly better result of 6,8% for co-evaporation was published after these experiments started.

3 Experimental

3.1 Fabrication techniques

Fabrication of CZTS thin films in this study was performed by a two-stage process, sputtering a metal precursor or a metal-sulphur precursor, respectively, followed by a sulphurization process.

3.1.1 Precursor deposition by sputtering

3.1.1.1 Sputter process

To deposit the precursors on the substrate, the magnetron sputtering technique is applied. It is based on momentum transfer from bombarding ions of working gas to the target atoms. By this, the atoms are knocked out from the target and are transported to the surfaces. When they get in contact with a surface, the atoms adhere, for example on the substrate. As a result, the substrates get coated by a thin film of the target material.

DC and AC sputtering

A sputter system is set up as follows. The target, i.e. the source of the used material, acts as the cathode and is connected to the several kilovolts high direct current (DC) voltage [48]. The anode is the substrate holder, or even the whole chamber like in the system used here, and typically connected to ground. In the evacuated chamber, a so called working gas is introduced. Often – and thus also in our case – Argon is used for this, as it is a noble gas (i.e. not reacting with the sputtered atoms) with low ionization energy. Furthermore it is low-cost and has a suitable mass for the momentum transfer to the target. Then a glow discharge is initiated and maintained in the chamber when a critical voltage is reached. The argon atoms get ionized by the high voltage and the electrons move to the anode (and ionize on their way further argon atoms), while the positively charged ions are accelerated towards the target and there knock out atoms. The aggregate state where electrons and atoms exist separated from each other is called plasma.

Sputtering in this way – with DC voltage – works only for conducting materials. In the case of insulating materials, the surface charges up because of the charge brought by argon ions. To avoid this problem, alternating current (AC) voltage is used. In our case, ZnS and ZnO required this approach.

Magnetron sputtering

In magnetron sputtering, a magnetic field is applied in order to confine the electrons in the target vicinity. The electrons then suffer more collisions with argon atoms thus increasing plasma density. That makes possible to reduce the working gas pressure, which, in turn, lets more energetic particles reach the substrate and also results in higher deposition rates [48]. Another positive effect of trapping the electrons near the target is reduced heating of the substrate.

Co-sputtering

It is even possible to sputter several targets at the same time. This could be desirable to dope a material by co-sputtering an appropriate small amount of the doping material, or to achieve a homogenous mixture of several compounds. If a sufficient energy supply is given – for example by heating the substrate –, even crystal growth already during sputtering can be enhanced.

We used co-sputtering in order to reduce diffusion of the sputtered metals during sulphurization.

3.1.1.2 Process used in this thesis

The metals copper, tin and zink were sputtered as precursor material. For this, a *von Ardenne CS 6005* was used. As this system has only room for two targets, a Cu/Sn alloy (99,99% purity) was used for the one target, the other one was a Zn-target (99,994-99,995% purity) or a ZnS-target (99,99% purity), respectively. The targets were produced by *Kurt J. Lesker Inc.*.

The sputtering was performed under a base pressure of between $3{,}8 \cdot 10^{-6}$ and $1{,}5 \cdot 10^{-7}$ mTorr. The working pressure was 2,7-6,7 mTorr with an Argon flow of 20 sccm (standard cubic centimeters per minute) in the first series, and fixed to 3,3 mTorr in the second series (Ar flow: 40 sccm).

5 samples were deposited on a heated substrate (300°C); all other depositions took place at room temperature.

The sputtering was performed as co-sputtering, i.e. all metals were sputtered at the same time, except of some films where multi-layers were deposited. The thicknesses of the films were varied between 100 nm and 1 µm. The deposition rate was changed between 20 and 80 nm/min. First, films only from one target (Cu/Sn or Zn, respectively) were sputtered to find out the rate for different settings. It turned out that the film thickness is proportional to sputter time and power. After this, co-sputtering was performed, and it emerged that the film thickness was approximate to the sum that one would expect from the individual thicknesses of each target at the certain power.

Concerning the composition, we aimed for stoichiometry, but also wanted to have variations in some samples to investigate the influence of non-stoichiometry such as Cu-depletion. Anyway, it was not possible to set an exact composition, all samples ended up with less Sn in the film than in the target.

In this diploma thesis, two sputter series were performed. The first one contained 47 different films and was done with a Cu/Sn-target (ratio: 60/40) and a Zn-target. These samples are referred to as *metallic precursors*. The second series included 44 films. The same Cu/Sn-target and a *ZnS* target were used. Those samples from the second sputter series are referred to as *ZnS precursors*. In this second series, also the substrate heating was tested for 5 samples.

The thickness of the precursors was measured using a *Dektak V 200-Si* profilometer.

Storage

In the first series, the sputtered samples just lay in plastic boxes with no further precaution, that means they were exposed to air, (sun-)light etc..

In the second series, two pieces of each sample (i.e. 2 pieces of SLG, Mo-SLG and Si) already cut in the right size for the sulphurization process (ca. 0,5x1,25 cm), were stored in a vacuum storage at ($5x10^{-8}$ mbar). The remaining parts of the samples were stored in plastic boxes in a nitrogen-flooded cabinet in the clean room, but not in vacuum.

3.1.2 Sulphurization

Quartz tubes

Due to the absence of an adequate oven that could be flown with H_2S or sulphur vapor, a quite special method had to be accomplished. Small pieces were cut off from the samples and sealed with sulphur powder into small quartz tubes, which then were heated in a normal oven.

As the glass had to be sealed by hand, only small quartz tubes could be used, otherwise they became too warm to hold them with hand. For this reason, only very tiny pieces of the samples could be sulphurized, i.e. a size of roughly 0,5-0,7 times 1-1,5 cm.

The original quartz tubes had a length of 1 m (outer diameter: 1 cm, inner diameter: 0,8 cm). They were first cut in the middle. The remaining 0,5 m pieces were warmed in the middle with a Bunsen burner and then carefully extended by pulling on both sides. By this, the quartz tube was melt thoroughly and two quartz tubes with melted end were made.

The quartz tubes with one closed end were then cleaned by immersing into a tank with heated water (60°C) and detergent. After it they were shower rinsed with de-ionized water.

Preparations

The sulphur used for this sulphurization process was available in form of powder (*Scharlau*, synthesis grade, 99% purity). Ca. 2–4 mg were weighted and put into the quartz tube. The amount of sulphur ending up at the bottom of the quartz tube was unknown and quite various, as on the one hand the weighting machine had an uncertainness of 0,1 mg (2,5–10%), and on the other hand always some powder adhered at the inner surface of the funnel used to pour the sulphur into the quartz tube (which was the considerably bigger source of error compared to the measurement inaccuracy). In the end, 1–4 mg of sulphur

could be assumed to be in the quartz tube. Then, the tiny sample piece was put into the quartz tube. Samples on SLG and on Mo-SLG came into the same quartz tube, back to back, the ones on silicon into one quartz tube by itself.

To provide a high vapor pressure and to have as little oxygen, carbon etc. in the quartz tube under the reactive time in the oven as possible, a vacuum in the quartz tube was requested. To preserve the vacuum in the quartz tube, it should be melt thoroughly in the middle while it is still connected to the vacuum pump. So, the open end of a quartz tube was connected with the flexible tube of a vacuum pump (*varian SD-91*) and evacuated for around 20 minutes down to a pressure in the order of some mbar. Then – still connected to the pump – the quartz tube was melted thoroughly in the middle.

Sulphurization process

The prepared quartz tubes could then be put into the furnace. There was room for maximum 6 quartz tubes. The furnace was a simple upright cement cylinder with a hole inside (*Eurotherm 904*). It was possible to run programs on this oven, i.e. ramping (raising the temperature in a wished velocity, here typically 4,2–8,4 °C/min) and dwell time at a certain temperature (or even on several stages) could be programmed. Setting used here were 1h ramping and dwell for 2h at 520°C. All samples cooled naturally, this means that the oven was switched off and the samples were taken out at room temperature.

To test if the vacuum is still present, a spark tester (*TMF Spark Tester MK.3, Buckleys (Uvral) Ltd.*) was used. It induces plasma in the closed quartz tube if there is a vacuum (see Fig. 3.1). Finally, the quartz tube was scored with a circular saw, to make it easier to break it up later.

3.1.3 Processing of the solar cell

The processing of the CZTS films to solar cells included substrate preparation, sputtering of the molybdenum back contact, deposition of CdS by CBD and sputtering of a ZnO/ZnO:Al TCO layer. This process was performed according to the "baseline" process of the Ångström solar center [49].

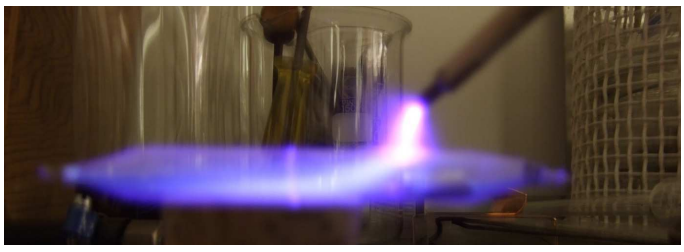

Figure 3.1: Spark tester induces plasma in the evacuated quartz tube.

3.2 Analysis techniques

3.2.1 Scanning Electron Microscopy (SEM)

SEM measurements are an important tool for the analysis of the morphology of films. The possibility to immediately see structures gives a direct and intuitive approach, which makes it to a popular analyzing method.

The functionality of an electron microscope is similar to an optical microscope, but instead of light, electrons are used. The advantage is the much smaller wavelength and the associated higher resolution. Typical electron energies are 10–30 keV, which refers to significantly smaller wavelengths than for light. For example, electrons with 20 keV like used in these experiments corresponds to a wavelength of 0,009 nm (light: ≈400–700 nm), according to *de Broglies formula* $\lambda = \frac{h}{mv} = \frac{h}{\sqrt{2qmV}}$, where h is the *Planck constant* ($6{,}626 \cdot 10^{-34}$ Js), m the mass of the electron ($9{,}1 \cdot 10^{-31}$ kg), q the elemental charge ($1{,}602 \cdot 10^{-19}$ C), v the velocity and V the acceleration voltage of the electron [50].

In a SEM, electrons are emitted from a filament and accelerated to an anode. Like in an optical microscope the beam is focused, but here with magnetic or electrostatic lenses instead of glass. The electron beam is than scanned over the sample. Secondary and/or backscattered electrons that are produced in this process are collected by a detector and a picture is created [50].

In this study a *LEO 440* SEM was used for EDS measurements (see next chapter) and a *LEO 1550* to make pictures of cross sections of the samples.

3.2.2 Energy Dispersive X-ray Spectroscopy (EDS/EDX)

EDS is a method to analyze the composition of a sample. It bases on the principle that electrons hit the sample where they excite bound electrons to leave the atomic shells. This process creates vacancies in the atomic shell, which are then filled up by electrons from higher shells. Hence, X-ray photons with characteristic element-specific energies are produced and can be detected to determine the content.

The characteristic photons are labeled with a Latin and a Greece letter. The Latin letter corresponds to the shell where the electron has been knocked out (from the K-, L-, M-shell etc.), the Greece letter indicates from which shell it has been substituted (α for the next higher shell, β for the next but one shell etc.). For example, if an electron from the K-shell is substituted by an electron from the L-shell, Kα X-rays are emitted.

When electrons impinge on a solid, they can interact in several ways: They can inelastically interact with the matter, i.e. get reflected or deflected (which widens the electron beam); they can interact with the atomic nucleus which produces bremsstrahlung (continuous radiation); and the electrons can ionize the atoms which causes characteristic radiation. The interaction volume of the electron beam with the material is a bulb as shown in Fig. 3.2. As can be seen the penetration depth is in around one micrometer. That means that the result of the EDS measurement might be dependent on the thickness of the

film, especially if there are depth gradients. For example, a secondary phase segregating as a sublayer below a film thicker than 1 µm would not or only partly contribute to the result. This should be kept in mind.

To determine the composition of the analyzed sample is not that easy. The first problem is that not only and not the whole characteristic radiation from the elements reaches the detector. On the one hand, the bremsstrahlung caused by the deceleration of the electrons in the material adds to the background of the spectrum. The software of the EDS program has to filter out arithmetically this noise. On the other hand, the deeper the electrons penetrate into the material, the more photons produced deep in the sample do not get out of it. This attenuation is not the same for all elements but depends of course on the energy of the photons, i.e. suppressed more for light elements. Consequently, higher electron beam energies are not necessarily better, as they increase the excitation but also the depth of penetration, which again increases the absorption.

Another fact that hinders the analysis is the overlap of lines of different elements due to noise in the detector and other electronic components, and as the channels that count certain energies have a certain width. For this reason, for each element different spectral lines are taken into account and compared, as they have a certain ratio. To remove the other named effects (background, absorption), complicated calculations have to be carried out by the software, or reliable reference samples with known composition are needed.

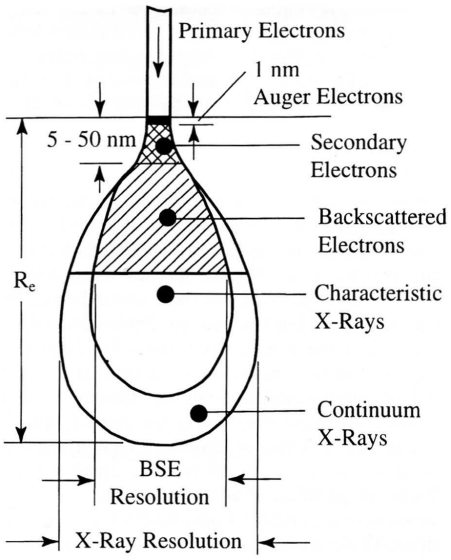

Figure 3.2: Interaction of electrons with matter. The form of interaction is different for different depths of penetration. For EDS, characteristic X-rays are used. R_e depends on the density of the examined material and on the electron energy [50]. In our case R_e can be calculated to be between 1 and 2 µm. From [50].

Anyway, the detection limit is typically not higher than 0,1% [48].

In the software used in this diploma thesis, elements or their peaks, respectively, are identified automatically and the atomic and mass percentage is immediately computed. Elements that are known to be not part of the sample or that are irrelevant for the considerations (like in our case the silicon from the substrate) can be removed manually, and the composition is then calculated for the remaining elements.

It should be noted that the height of the peaks is not linearly connected to the concentration, and not even the elements in one measurement can be estimated relatively to each other just by the peak height. The excitation is different for varying incoming electron energies, and different for the particular element. Furthermore the named effects background (which is not the same for all energies) and absorption play an important role.

Often – and also in our case – the incoming and exciting electron beam comes from an SEM where the EDS is attached to. The photons are detected by a silicon detector doped with lithium. The incoming photons produce electron-hole-pairs, and the number is linear to the photon energy. The pulses are in the following amplified and then sorted into channels according to their energy. The resulting spectrum is then among other things dependent on the intensity of the incoming electron beam, the atomic concentration, the ionization cross section, the X-ray absorption coefficient in the material and the detector efficiency, which leads to a complicated formula to analyze the data. [48]

The equipment used for the EDS measurements was a *LEO 440*.

3.2.2.1 EDS reliability measurements

EDS was one of the most important analyzing methods in this work. For an estimation of the error range of the EDS results diverse measurements were performed.

- Same sample - same area: Deviation for exactly the same conditions.
- Same sample - different area: Exploration of lateral gradients.
- Same sample - different resolution: Also influence of different areas.
- Same sample - different date: Stability of the EDS measurement.
- Different substrates: Si, SLG and Mo.

The first case, where exactly the same area was measured, gave as one would expect the lowest deviations: in average the results for the elements differed by 2% (standard deviation divided by the mean value; average over all samples and elements).

For different regions on the same sample, where lateral gradients within the film could come into play, the average deviation accounted for 4%. This slightly increased variation compared to measurements on the same area might be explained by small lateral gradients as well as non-uniform segregation of secondary phases within the film.

For the same reason, i.e. to see if it plays a role which area of the substrate is measured, compositions for different resolutions on the same sample were measured. This was done for 100x, 250x and 1000x magnification (250x was the default value used in our experiments). No significant deviations could be observed, in average 2% difference was seen.

The most critical cases are when samples are measured on different days (i.e. it cannot be guaranteed that exactly the same conditions prevail). In average, the mean values of the different days differ up to ca. 10%. Even taking into account that most probably different areas were measured (as mentioned this would mean ca. 4% variation) this is quite a lot. This might be due to variations in the sensitivity of the detector and the exact properties of the electron beam.

In Table 3.1 the results for the measurements on different substrates (Si, SLG, Mo-SLG) are given. The last row shows the variation that was measured for the same sample but on different days.

The compositional results between the (assumed) same films on Si and Mo as well as Si and SLG were compared to each other and the average deviation between the values was calculated. The difference is mostly below 6%, in one case up to ca. 11% deviation between same films on different substrates.

This result means that the composition of equally processed films on different substrates can be assumed to be equal, as the EDS results do not show more deviation between same films on different substrates compared to the same film on the same substrate. Nevertheless it is not impossible that some variation also results from different forming of CZTS on the different substrates, which might affect both the loss of certain elements and the structure or density of the film, respectively. The latter influences also the thickness, which can itself affect the result if there is a depth gradient.

	Cu/Zn	Cu/Sn	Cu/(Zn+Sn)
Si ↔ Mo	1,7%	11,2%	5,9%
Si ↔ SLG	5,7%	4,2%	5,9%
Si ↔ Si	8,2%	9,5%	10,3%

Table 3.1: Deviations in the EDS measurements concerning different substrates. The data for SLG and Mo-SLG are referred to measurements on Si on different dates (last row). Compared to this, the error range for glass and glass coated with molybdenum is comparable (even smaller). Hence, the same composition on the different substrates can be assumed.

In default of an appropriate calibration sample, the EDS measurements had to be verified in a different way.[1] This was done by comparison of the Cu/Zn ratio with XRF[2] measurements. The average deviation was about 9%, which is near the variation of EDS itself for different days.

The conclusion is that EDS is possible to be used for composition measurements. However, it should be kept in mind that variations up to 10% can occur.

3.2.3 X-ray Photoelectron Spectroscopy (XPS)

XPS is a method closely related to EDS and XRF. Incoming X-rays knock out electrons from the atomic shells of the sample, which is referred to as photoelectric effect. These electrons are detected by a spectrometer and allow conclusions about the composition of the irradiated substance. Furthermore, also information about the bonds of the elements can be obtained as the electron levels are influenced by bindings. This allows to draw interesting conclusions for example if oxides or sulfides are formed [50].

As electrons are already absorbed by very thin layers of material, XPS is very surface sensitive (much more than for example EDS or XRF). In this work this method was mainly used to get information about the depth profile of the composition of the samples. For this the sample had to be sputtered, that means the material was gradually removed while measuring the composition.

For this thesis, a *Quantum 2000 Scanning ESCA Microprobe* from *Physical Electronics* with monochromatic Al Kα X-ray radiation (1486,7 eV) was used. All XPS sputterings considered here were performed at 0,5 keV.

3.2.4 X-Ray Diffraction (XRD)

The technique *XRD* was used in this study to identify secondary phases in our films. It bases on the diffraction of waves by a lattice. The wavelength of the incoming light has to be in the order of the lattice constant for this effect to take place. As crystals have lattice constants in the order of nanometers or Ångströms, X-rays with a similar wavelength are used.

Considering a crystal, the incoming light waves are reflected by the crystal planes. For a certain angle θ that depends on wavelength λ and distance of the crystal planes d, the reflected waves interfere constructively and give a measurable intensity. This is described by *Braggs law*: $\Theta = \sin^{-1}(\frac{\lambda}{2d})$ [50].

1 There was actually one more confirmation that cannot be called a "calibration" but was used before XRF measurements to see how reasonable EDS is. The Cu/Sn = 60/40 sputter target was measured with EDS and the result was $\approx$ 59/40 (1% other elements).

2 *XRF* (X-Ray Fluorescence) analysis is related to EDS. Electrons are by incoming radiation (X-rays) removed from the atoms and substituted by electrons from higher shells. During this process they emit fluorescent X-rays that are characteristic for the element. The difference to EDS is the excitation by polychromatic X-rays instead of electrons [51]. In these experiments the *Spectro X-lab 2000* was used.

That makes it possible to determine for known angle and wavelength the lattice spacing. The other way round, unknown phases can be identified by the characteristic reflection pattern that depends on the lattice parameters. This is used here.

The advantage of this technique is that it is nondestructive and needs no elaborate sample preparations [48]. For thin films, however, it is a problem that the volume of material that contributes to the signal is very small. This would require very long counting times. A way to avoid this is the technique of grazing incidence. A very small angle is applied which increases the effective volume by some factor in the order of 10 [48].

In our experiments, a *Siemens D 5000* was used. The wavelength of the X-rays was 1,54 Å (gained from a Cu-target), the angle of gracing incidence was 1°.

The XRD peaks are often of different intensity, and in principle the measured signal has only to be compared with the pattern of the related phase in a data base. One problem is, though, that peaks often overlap. For example, since the peaks of Cu_2ZnSnS_4 (CZTS), Cu_2SnS_3 (CTS) and ZnS – which all have the sphalerite structure (see chapter 2.3.3) – overlap, it is complicated to identify CZTS clearly. Indeed, the first two compounds have some small extra peaks which ZnS does not show, but ZnS on the other hand has no unique peak. That means that ZnS can never be proven or excluded, as long as there is crystalline CZTS (and/or CTS). In literature this signal is referred to as Σ-signal.

Another common problem is that often only a part of the peaks of the phase one would assume is present. That means that if only a few expected peaks appear, this phase cannot be proven but neither be excluded. This was a major problem in our XRD analysis and can be due to preferred orientation of the crystals. Typically, the reference spectra are for powder diffraction and in case of preferred orientation, some peaks may not be present. Furthermore, the absence of an XRD signal does not have to mean absence of the secondary phase, since it could be present in amorphous phase.

3.2.5 Quantum efficiency (QE) measurements

One technique for analysis of solar cells is quantum efficiency (QE) measurements. It allows conclusions about the losses in the cell, effectiveness of charge separation and the absorption, or charge generation. Quantum efficiency means how many of the incoming light quanta are converted into electron-hole-pairs and collected in the outer circuit. Here, always the external quantum efficiency will be meant, that means the incident and not only the absorbed photons are counted. The incoming light is monochromatic and varied stepwise (for our cells from 360 to 900 nm in 10 nm steps). If all incoming photons excite each one electron-hole-pair that is collected, this would mean a quantum efficiency of 100% or 1, respectively. Theoretically a QE higher than 1 is possible if photons with an energy higher than the double band gap produce two electrons. Practically this effect is irrelevant, though.

In our experiments the signal of the monochromatic light is split by a chopper. That

allows to refer the measurement signal to the incoming monochromatic light.[1] The light can be superposed by biaslight to analyse the influence of light intensity on the cell. The result is calibrated with a reference sample of known quantum efficiency.

The QE curve allows drawing conclusions about the absorption and recombination losses in the solar cell. Furthermore the band gap can be estimated. For this the x-scale is converted from wavelength to energy ($E = h \cdot f = h \cdot \frac{c}{\lambda} = 1240 \frac{eV \cdot nm}{\lambda}$) and the QE-values are squared. Reason for this is the relation $QE\left(E\left(\lambda\right)\right) \approx \sqrt{E - E_g}$. That means that the squared QE curve in theory intercepts the energy axis at E_g. Practically one has to take into account that the material contains secondary phases with a lower band gap than the considered semiconductor. Those as well as defects could lead to some absorption of the photons even below the band gap. Therefore not the energy at $QE^2 = 0$ is taken, but the slope is extrapolated to 0, like shown in Fig. 3.3. The described procedure is a common way in literature to determine QE (see for example [52]). However, this includes of course some freedom where exactly to draw the extrapolation line. For this reason we consider this more as an estimation for the band gap than an exact definition.

Next to the information that can be extracted from the shape of the QE curve, by integrating quantum efficiency with photon flux the short circuit current can be calculated.

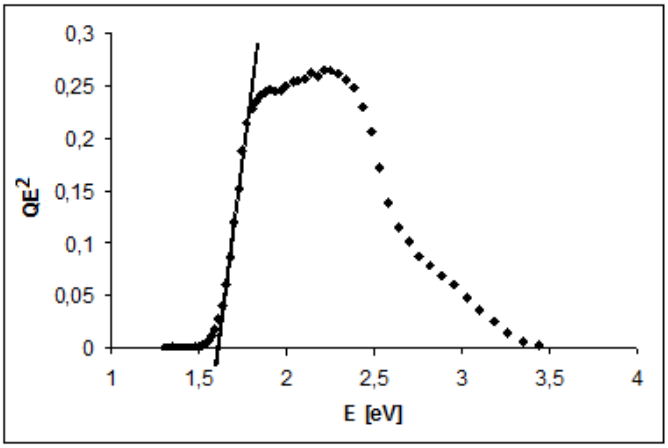

Figure 3.3: Squared QE curve to extract the band gap. The slope of the curve on the low energy side is extrapolated lineary. The interception with the energy axis gives the energy of the band gap. Here the band gap is roughly between 1,6 and 1,7 eV.

1 As the measurement is not performed in complete darkness, otherwise the ambient light would contribute to the counting.

3.2.6 Current–voltage (IV) measurements

The functionality of a diode concerning (short circuit) current and (open circuit) voltage are described in detail in the theory part of this thesis (chapter 2.1.7). To measure the diode characteristic the solar cell is contacted at the surface and the back contact. Then the solar cell is illuminated and the current is measured while at the same time varying the voltage that is applied, which gives the IV-curve.

Additionally, the measurement can be performed in darkness as well. This can give further insights about the cell. For example, an increasing current for negative voltages could be due to a shunt through the space charge region or due to voltage dependent carrier collection (for more details see chapter 2.1.6). As the latter effect occurs only under radiation, i.e. when electrons are produced and can be collected by the SCR, it can be excluded if the dark curve does no show an increasing current for increasing (negative) voltage.

In this work the light source is a halogen lamp, calibrated to provide an intensity giving the same short circuit current as that obtained from QE measurements on CZTS devices. The temperature is maintained at 25°C by a water-cooled peltier element.

4 Results and discussion

4.1 Sputtering of precursors

This chapter will cover the composition of the precursors, structural insights, as well as considerations on deviations from the standard sputtering process.

4.1.1 Composition

4.1.1.1 Growth of films at different powers and for different periods

In our experiments, altogether 91 different depositions were performed, except of some test runs all of them on silicon, glass and glass coated with molybdenum in each run. The depositions were split into two series: 47 depositions with a Cu/Sn and a Zn target, and 44 depositions with a Cu/Sn and a ZnS target in order to get S-containing precursors.

The first aim was to find out the deposition rate in order to determine the needed deposition time for desired thicknesses. For this, depositions from single target of only Cu/Sn and Zn (ZnS), respectively, were done, and the film thicknesses were measured.

For the Cu/Sn-target the sputter process was very stable. Two series at 200 W and 400 W were performed, each with several different sputter times. The results showed a linear increase in thickness with deposition time, so that a deposition rate for each power could be calculated. These were 29,6 nm/min for 200 W, and 58,5 nm/min for 400 W. Thus, the sputtering process for the Cu/Sn target also showed a linear dependence in sputtering power, which made it possible to vary the sputter power arbitrarily and interpolate the expected thickness.

For the Zn target, the results were not that well-defined. Three series (at 50, 70 and 100 W) were made, that also showed linearity in deposition time. Plotted for different powers, though, the growth per minute is not linear, especially not if the linear slope should intercept 0 (see Fig. 4.1). Therefore no interpolation was done and for this target and only the deposition rates 50, 70 and 100 W were used.

On basis of the gained results, it could be calculated which thickness one would obtain for certain power settings. It turned out that in average the calculated and measured total film thickness were differing by 6%. This is a very good value, considering that there is also an error of measurement from the profilometer, which was found to be $\approx 3\%$. For this reason we can expect that the sputter rates for the single (Cu/Sn and Zn) films are preserved in co-sputtering.

In the second series, the Zn target was replaced by a ZnS target. This target was always

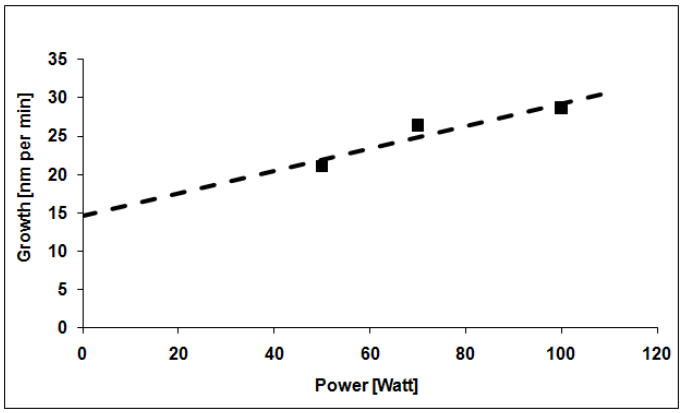

Figure 4.1: Zn deposition rate for different powers. The slope cannot be proven to be linear. For this reason no extrapolated but only measured values of Zn growth are used for composition calculations.

sputtered at 400 W. At this power, the target showed a constant and stable behaviour with a deposition rate of 24,4 nm/min.

In spite of the linear behaviors of the Cu/Sn and the ZnS target, the expected and the measured thicknesses of co-sputtered films were on average differing by 13%. As all films were thicker than expected, this allows the conclusion that either the co-sputtered film is more porose or less dense, respectively, or that anomaly in the co-sputtering causes that more material is sputtered compared to the single material layers. As the ZnS target was operated in RF sputtering mode, it might have been influenced by the presence of the DC sputtering of the Cu/Sn target during co-sputtering.

4.1.1.2 XPS studies on precursors

On some of the precursors, XPS measurements were performed to get information about composition (details including the graphs can be found in Appendix A.2). XPS is very surface sensitive. That offers the possibility to determine gradients in the film, if the material is uniformly removed by sputtering, which was the case here.

We compared 4 precursors with XPS. Each one sample pair was sulphurized in the same run, but on different substrates: Si and Mo, respectively. One sample pair was pure metal precursors, the other one ZnS precursors. In both cases the composition was very uniform within the film. Furthermore, no difference between Si and Mo substrate could be observed, both showed homogenous element distribution within the film. The only gradients that could be observed for all 4 films were related to the surface, which was found to be Cu-poor and Sn- and Zn-rich.

That means that no difference in composition and gradients could be found for the different substrates Mo/Si and for ZnS/metallic precursors from XPS.

4.1.2 Structure

To get insights about our precursors beyond composition, XRD analysis was done to reveal information about structure and existing phases.

Firstly, we take a look at the metallic precursors as well as single Zn and Cu/Sn films. In Fig. 4.2, the black pattern belongs to a pure Zn film, sputtered from the Zn target. The red line shows the data of a Cu/Sn film as sputtered from our Cu/Sn 60/40 target. Last, the green line is a typical precursor, composition according to EDS of Cu/Zn/Sn = 46/25/30.

The vertical lines in the diagram – black, blue, green and red – denote XRD peaks for different crystal structures, in which the length is related to the intensity of the peak from randomly oriented powder samples. The reference data is taken from the *JCPDS* (*Joint Committee on Powder Diffraction Standards*) data base.

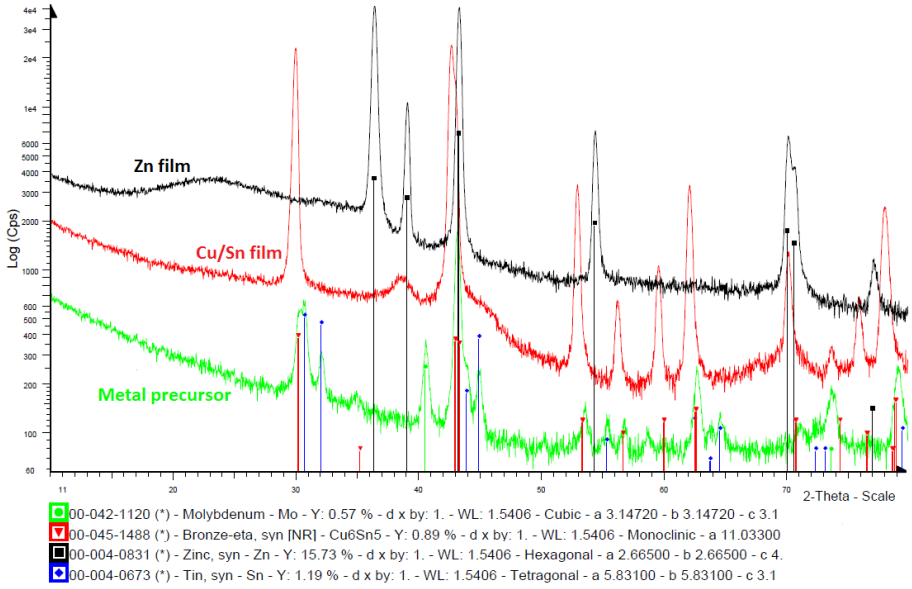

Figure 4.2: XRD pattern of a Zn (black line), Cu/Sn (red) and Cu/Sn/Zn (precursor) film (green). The vertical lines indicate where peaks for zinc (black), tin (blue), molybdenum (green) and bronze (red) would be expected. The Zn film shows hexagonal zinc structure, the pattern for bronze is slightly shifted as compared to our curve. The metal precursor contains crystalline tin (tetragonal structure) and probably bronze according to XRD.

The Zn line (black) matches clearly with the expected signals for hexagonal zinc structure (black as well). Obviously, sputtered pure Zn forms this structure for pure films.

The red pattern, belonging to the Cu/Sn film, is a bit more difficult to clarify. Peaks referring to Cu_6Sn_5 (bronze) would match perfectly (red), anyway, they are all shifted compared to the Cu/Sn peaks for around 0,5°. The reason for this could be that the stoichiometry is slightly different, for example Cu_7Sn_5 or similar instead of Cu_6Sn_5. This

could lead to a slightly different signal for the same structure, if the lattice is stretched.

Additionally to Cu_6Sn_5 or related, more Cu-rich compounds would be expected, as a Cu/Sn ratio of around 1,7 was measured by EDS. Indeed, pure Cu cannot be excluded by this pattern, as it's main peak is at around 43°, a peak that exists here. Further weaker peaks, like for 50,5°, cannot clearly be identified here, though. The existence of amorphous Cu or Cu-compounds is another possibility, but that cannot be detected with this method.

The precursor pattern (green line) shows – in contrast to the Cu/Sn film – a clear match to elemental Sn (tetragonal structure). All blue vertical lines showing the expected Sn peaks find a related peak in the precursor pattern. Further peaks can be explained by bronze (red lines), which means that the existence of this phase is very likely here.

Several more peaks, in contrast, are not so easily to assign to a certain phase, while at the same time several phases cannot be excluded to occur. Cu (43° and weaker at 50,5°) and CuZn (43°) are quite possible and likely. Cu_5Zn_8 (major peak at 43°) is often reported for metal precursors ([38], [26]), but no clear evidence for this can be found here.

In Fig. 4.3, ZnS precursors are shown. Here we concentrate on the black line, the others will be discussed in the next chapter as they were sputtered under special conditions.

It can be seen that the XRD pattern shows a much more amorphous structure. Except of three distinct peaks that can be related to the substrate (Mo, red vertical lines), the peaks are very broad, indicating an amorphous or nanocrystalline structure. For this reason, a clear assignment to certain phases is not possible. Both broad 'peaks' could belong to bronze (pink lines) and Sn. The broad peak between 40° and 46° could include elemental Zn and Cu as well as CuZn (all have the major peak at 43°).

4.1.3 Special settings

During the second sputter series with the ZnS target, some settings that vary from the otherwise adjusted settings were carried out. To the best of our knowledge, none of these special settings caused any major change in the precursor, as we will support in this chapter, so that we treat them in the following as ordinary samples, if they were used to make solar cells.

4.1.3.1 Slowly sputtered

5 precursors were sputtered with only half of the usual power. These precursors are referred to as 'slowly sputtered'. Compared to the average composition of 'normal sputtered' precursors, no abnormal variations could be observed. Looking at the XRD data (Fig. 4.3, red line), the pattern looks very similar to the normal sputtered reference (black line). From this the conclusion is, that slowly sputtered samples can be treated without as normal samples.

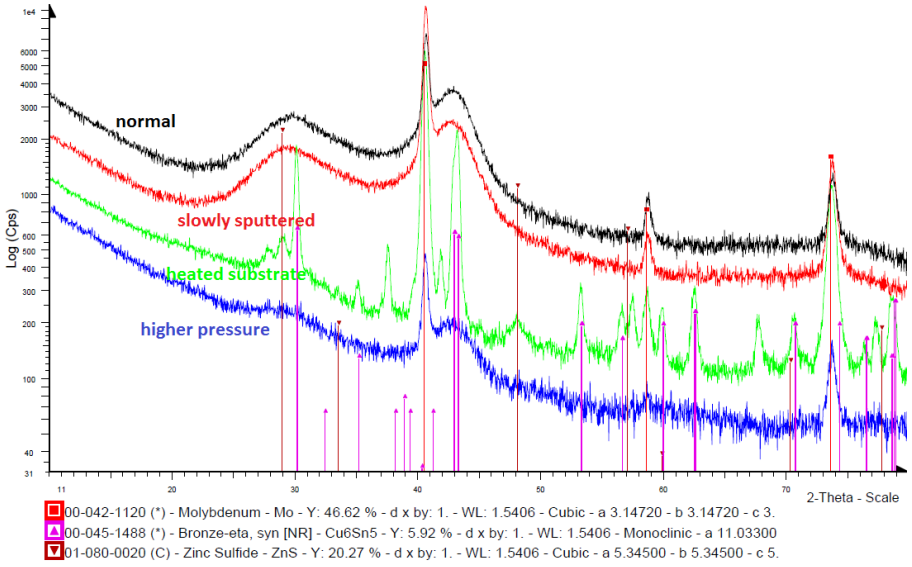

Figure 4.3: XRD pattern of ZnS precursors, sputtered under normal conditions (black line), slowly sputtered (red), with higher gas pressure (blue) and with heated substrate (green). Except for the sample with heated substrate, all films have an amorphous structure and are very similar. The crystalline XRD pattern for the heated substrate sample matches to bronze (pink vertical lines); ZnS (or CTS/CZTS) is very probable (brown). Several peaks cannot be clearly assigned.

4.1.3.2 Higher gas pressure

For 13 out of 44 samples in the second series, the pressure in the sputter chamber was different from the default settings. That was not a wished effect. However, no unusual variations in composition were found, and like for the 'slowly sputtered' case, no difference for the XRD pattern (blue line in Fig. 4.3) compared to the reference sample can be found. The weaker XRD signal results from an exchange of the X-ray tube in the used XRD machine for samples with the stronger signals (red and black lines).

4.1.3.3 Heated substrates

As for the previous special cases, the composition of samples with heated substrates (4 precursors) had no unusual deviations from the average compositions for the used power settings. The XRD data, however, shows a significant different pattern than the three other precursors presented in Fig. 4.3. In contrast to those samples, the pattern for the heated substrate precursor shows clear crystallinity. *Bronze* (Cu_6Sn_5) is clear identified (pink vertical lines). *ZnS* (brown) looks very probable, but at the same time *CZTS/CTS* cannot be excluded as both patterns coincide very much in XRD (see chapters 2.3.3, 3.2.4).

Several peaks can again not or not clearly be assigned to a certain phase, as well as several elements or compounds cannot be unambiguously identified. Those are in this case Cu, Cu_5Zn_8 and Zn (Peak at 43°), as well as Cu-Sn compounds and copper sulfides.

4.1.3.4 Summary

As precursors sputtered slowly or with higher pressure do not change in structure and composition, they will simply be treated as 'normal' samples. For heated substrates, the situation is a bit more complicated, as the structure appears to be much more crystalline than for other ZnS-precursors. But as only one single cell was made of heated substrate precursors, and no conclusions are drawn only from this specific cell, while it on the other hand does no show any major abnormality in composition, morphology or efficiency, we won't consider this special setting any further.

4.1.4 Conclusions

Sputter experiments showed that the Cu/Sn target behaved very stable while for the Zn target non-linear growth of the films was observed. This could be due to some interaction of DC (Cu/Sn target) and RF (ZnS target) sputtering that could have occurred during co-sputtering.

XPS studies on some samples indicated that precursors on Mo and Si can be treated as equal, as they showed same composition and behaviour regarding gradients. For metallic precursors no gradients within the film but a Cu-poor and Zn-rich surface were observed; ZnS precursors had a slight Cu gradient within the film and a very Sn-rich surface.

Further analysis on the precursors was done with XRD. A general problem here was that not all peaks could be assigned to a certain phase, which means that only few phases could be proven to be present.

Pure Zn films matched clearly to the signal of crystalline Zn. Pure Cu/Sn films showed the peaks for Bronze (Cu_6Sn_5) but shifted about 0,5°. This might be due to a different composition. Further Cu-containing phases could neither be proven nor be excluded.

For the metallic precursors (Cu+Zn+Sn) crystalline Sn was found, Cu and CuZn are very possible.

ZnS precursors (Cu+Zn+Sn+S) turned out to be amorphous, except for one that had a heated substrate. A lot of phases (Cu, Zn, Sn, CuZn, Cu_6Sn_5 and more) might contribute to the broad peaks that were seen here. The sample with heated substrate indicated the existence of Cu_6Sn_5 and ZnS (or CZTS, CTS); Cu, Cu_5Zn_8,Zn as well as Cu-Sn compounds and copper sulfides are possible.

Another conclusion from XRD combined with compositional considerations was that precursors with different sputtering processes (slow sputtering, different pressure, heated substrate) can be treated as equal.

4.2 Properties of sulphurized films

This chapter shows the results of the analysis done on CZTS films obtained by sulphurisation of precursors. The measurements included SEM, EDS, XPS and XRD, and were used to identify compositional evolution (e.g. element losses under sulphurization), structure, appearance (e.g. grain size) and existence of secondary phases. The main goal was to analyze the quality of the synthesized material.

4.2.1 Data set

Table 4.1 shows the most important data for all sulphurized samples that were part of this study. They are grouped by the region of the phase diagram where the final CZTS films belong to (column 'category'). The first column contains the sample number that will be referred to in this thesis. The second column gives type of the precursor which either contained sulphur or was a metallic one (for the labeling metallic and ZnS see chapter 3.1.1.2). Next, the composition of the CZTS film is shown. It should be noted that only the three metals and their fraction relative to the total metal amount is given; the amount of sulphur was always 50% within the measurement accuracy. The next two columns show thickness of the precursor and CZTS, in which the CZTS thickness shows the range of thicknesses that could be estimated from SEM cross section images. For samples 24 and 25 (last two rows) no SEM images were made, and as the CZTS thickness was extracted from these no information about the CZTS thickness is available here. The further columns show the solar cell parameters of the solar cell with highest efficiency of each sample.

These 25 samples were used to make solar cells and are discussed in this thesis, and the table shall provide all available information.

4.2.2 Composition

4.2.2.1 Compositional changes during sulphurization and CZTS formation

CZTS from ZnS precursors

An appropriate tool to get a quick overview of composition related properties is the phase diagram. Fig. 4.4 a) illustrates the compositional changes during sulphurization of ZnS precursors. Inset as visual help are the directions of Sn- and Zn-loss. Arrows point in the direction from precursor to the sulphurized sample composition.

A clear trend is the movement of most samples roughly in a direction corresponding to Sn-loss, even if they often show minor components of other directions like Zn-loss.

Some samples, however, point in completely different directions; they are marked in grey. Those directions make, seen from a physical point of view, no sense, as they would indicate compositional changes like Cu-loss (no physical mechanism for this shown for CZTS) or Zn-enrichment. Those changes in composition are probably caused by measurement errors, most likely by the accuracy of EDS.

#	Type	Cu [%]	Zn [%]	Sn [%]	Prec [μm]	CZTS [μm]	η [%]	V_{oc} [V]	I_{sc} [$\frac{mA}{cm^2}$]	FF [%]	TPD
11	ZnS	47,2	27,4	25,3	0,40	0,6-0,8	2,7	0,61	10,3	42,6	Zn-rich
21	Metal	46,2	30,3	23,5	0,49	1,5-2,2	2,6	0,66	12,6	35,1	Zn-rich
22	Metal	46,5	29,9	23,6	0,49	1-1,3	2,3	0,64	10,5	35,0	Zn-rich
23	Metal	45,7	30,8	23,5	0,49	1,0-2,0	2,7	0,69	9,0	43,2	Zn-rich
15	Metal	48,2	27,6	24,2	0,60	1-1,6	0,5	0,53	3,6	28,2	Zn-rich
16	Metal	46,6	25,9	27,6	0,31	0,7-1,3	0,5	0,22	7,7	26,8	Cu-poor
7	ZnS	46,5	25,5	28,0	0,49	1-1,3	1,8	0,57	10,4	29,7	Cu-poor
8	ZnS	47,1	25,6	27,3	0,49	0,9-1	1,9	0,71	9,6	28,6	Cu-poor
6	ZnS	45,8	26,3	27,9	0,40	0,7	1,9	0,49	8	47,9	Cu-poor
17	Metal	47,2	26,5	26,3	0,46	1,1-1,4	2,1	0,55	8,2	47,3	Cu-poor
9	ZnS	47,7	25,2	27,1	0,49	1-1,1	2,5	0,62	9,3	43,6	Cu-poor
10	ZnS	47,8	25,3	26,9	0,49	1,2	3,2	0,72	10,9	38,9	Sn-rich
20	Metal	49,1	24,6	26,3	0,46	1-1,5	0,8	0,34	7,5	31,3	Sn-rich
3	ZnS	51,4	21,2	27,4	0,80	0,85-1,15	0,0	0,08	2,5	25,5	Zn-poor
2	ZnS	49,2	22,8	28,0	0,39	0,7-1,2	0,0	0,06	1	26,5	Zn-poor
1	ZnS	48,9	21,7	29,4	0,47	2-2,5	0,0	0,01	0,8	25,0	Zn-poor
4	ZnS	50,7	22,0	27,3	0,47	1,7-2,1	0,0	0,08	1,1	26,5	Zn-poor
5	ZnS	50,2	23,5	26,3	0,39	0,8-1	0,1	0,09	1,8	30,7	Zn-poor
14	ZnS	49,1	24,9	26,0	0,47	1	0,0	0,04	1,1	24,9	stoic
19	Metal	48,8	25,4	25,8	0,46	1,3-1,6	0,1	0,06	3,3	24,9	stoic
18	Metal	48,3	26,1	25,5	0,31	0,55-1	0,2	0,11	6	27,1	stoic
13	ZnS	49,5	24,9	25,5	0,47	0,5-1	0,4	0,28	3,6	38,1	stoic
12	ZnS	48,3	27,0	24,6	$\approx 0,20$	0,4	1,1	0,44	6,1	39,1	stoic
24	ZnS	52,8	34,7	12,4	0,49	-	0,0	0,02	0,6	23,2	Sn-poor
25	ZnS	53,7	34,6	11,7	0,49	-	0,0	0,02	0,5	25,8	Sn-poor

Table 4.1: Data set of all samples that were fabricated to solar cells. The data set contains sample number, precursor type, composition regarding the metals, thickness of precursor and final CZTS film, the solar cell parameters efficiency, open circuit voltages, short circuit current and fill factor, as well as the region of the phase diagram where the sample is assigned to.

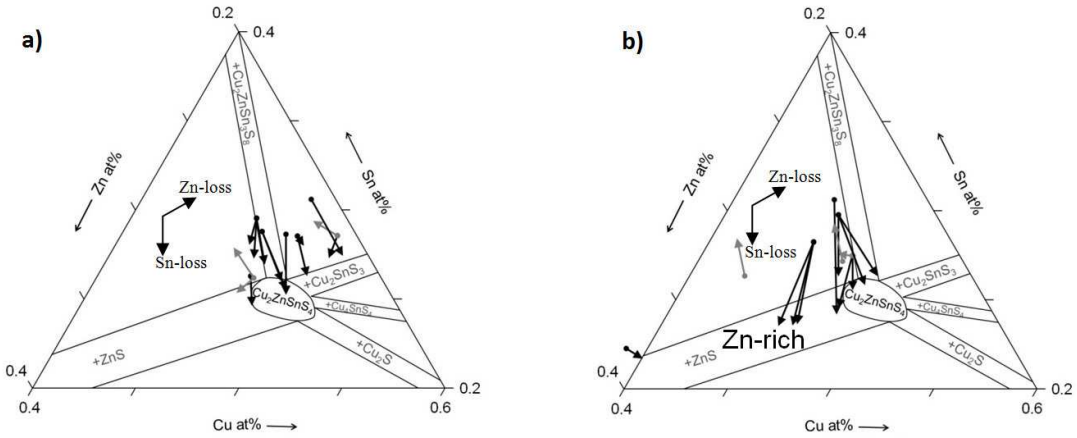

Figure 4.4: Ternary phase diagram showing the compositional changes for a) ZnS and b) metallic films. Arrows point in the direction from the precursor to the sulphurized sample.

CZTS from metallic precursors

For metallic precursors, the general impression is the same as for the ZnS samples (Fig. 4.4 b)). Most samples show Sn-loss, but some other directions exist as well. However, here the trend appears to be much more pronounced, i.e. a stronger Sn-loss occurs.

It is also worth noting that no remarkable Zn-losses can be observed which was reported in many publications (e.g. [46]), even for those samples that end up in the Zn-rich region and could have reached stoichiometry by Zn-loss.

Mechanism of Sn–loss and possible explanation for differences between metal and ZnS

It is very likely that the Sn-loss occurs by evaporation of SnS_2 that is formed early in the sulphurization process at 180°C for Cu-poor films like used here [29]. The material in this way looses the excess tin. That means that almost all samples achieved a Cu/Sn ratio closer to stoichiometric (which would be 2). At the same time, the Sn loss for our samples was never so large that films would end up in the Sn-poor region of the phase diagram. The tin loss observed here seems to be a beneficial process for the CZTS formation in cases like ours, where the initial Cu/Sn ratio is below 2. This observation is contrary to frequently reported tin loss beyond a beneficial dimension (e.g. [28]). We contribute this to the sealed quartz ampoules used in this process, where an atmosphere of tin sulfide is established which prevents further tin loss.

As mentioned before, the trend is much more pronounced for metallic precursors. The examined precursors changed from Cu/Sn = 1,58 to 1,89 (near stoichiometric) for metallic, and from 1,68 to 1,79 for ZnS precursors. The question is what the cause for this difference is. It seems very likely that the reason could be related to the fact that ZnS precursors contain S already before sulphurization.

For metallic precursors, the following reaction path[1] has been proposed[2] ([29], [28], [26]).

In the beginning, the S has to diffuse into the film of the precursor to get in contact with the elements to react. The first sulfides that are formed are the binary sulfides, i.e. copper sulfides ($Cu_{(2-x)}S$, $2 \leq x \geq 1$), zinc sulfides (ZnS) and tin sulfides (SnS_2). This happens below temperatures of 300–350°C ([28], [26]).

In the next stage, these sulfides react with sulphur to more complex structures like Cu_2SnS_3 (that itself reacts with ZnS to CZTS) and Cu_2ZnSnS_4. This step starts at around 350°C ([28][3]) to 400°C ([26]).

The reactions are summarized below.

$Cu+Zn+Sn+S$	$\rightarrow$	$Cu_{(2-x)}S+ZnS+SnS_2$	(<300–350°C)
$Cu_{(2-x)}S+SnS_2$	$\rightarrow$	Cu_2SnS_3	(>350–400°C)
$Cu_{(2-x)}S+ZnS+SnS_2$	$\rightarrow$	Cu_2ZnSnS_4	(>350–400°C)
Cu_2SnS_3+ZnS	$\rightarrow$	Cu_2ZnSnS_4	(>350–400°C)

For the process in our samples, it seems very likely that very early formed SnS_2 evaporates partly. Possibly existing further excess of Sn (most likely in form of SnS_2 as there is excess sulphur) that is formed deeper in the film and does not reach the surface but is enclosed by the CZTS (and other, secondary phases) will then remain as conglomerates or maybe as a SnS_2 layer.

The described reactions refer to metallic precursors. For S containing precursors the reaction path could be different. Sulphur is now – even though not in sufficient amount – available throughout the whole film already from the beginning. Binary sulfides can be formed everywhere much earlier, or may even exist from the beginning. XRD analysis of the precursors (chapter 4.1.2) did not show any crystalline phases for ZnS precursors. However, the results for the heated substrates could give an indication. XRD measurements of precursors heated up to around 300°C suggest that ZnS (or even CTS or CZTS) exists in those samples. That means that either ZnS could be present in all ZnS precursors (in an amorphous, or crystalline but disordered form), or at least should be formed at

1 For further details see chapter 2.3.4

2 Schurr et al. [29] and Weber [28] performed XRD analysis during the annealing process, Scragg [26] interrupted the sulphurization process at certain temperatures and cooled rapidly, assuming that the existing phases at the interruption temperature "freeze".

3 As mentioned before, it is not possible to distinguish between CTS, CZTS and ZnS from XRD. Anyway, Weber was able to find strong evidences for the present phases by additional XRF measurements. His precursors were layered: Mo/SnS/CuS/ZnS. The XRF signal of Cu and Sn is attenuated by the upper layers, i.e. occurance of a mixture of layers can be found by an increasing signal of Cu or Sn, respectively. An increase of the XR**D** Σ–signal, without any change of the XR**F** signal of Zn indicates that Zn did not diffuse and Cu_2SnS_3 is formed. The amount of ZnS cannot be increased as all Zn is already present in the form of ZnS from the beginning. This reaction takes place between 250 and 300°C. At 350°C, the XRF Cu signal increases, while the Zn signal decreases. This indicates interdiffusion of both elements. CZTS formation then likely starts from Cu_2SnS_3 and ZnS.

temperatures below 300°C. The copper and tin sulfides should be formed very early in the sulphurization process as well. So the question is, could these sulfides in the ZnS precursors form CTS and CZTS much earlier than in the metallic precursors, or is the formation limited not by sulphur but requires achieving a certain temperature? According to Weber [28], copper and tin sulfides form Cu_2SnS_3 already at 250°C. This means that temperature can obviously not have been the limiting factor in experiments with metallic precursors, but rather the fact that first binary sulfides had to be formed before the sulphurization could proceed.

Therefore, following mechanism for our ZnS samples may be proposed: copper, tin and zinc sulfides are formed very early or are even present already throughout the whole ZnS precursor. That makes it possible to form Cu_2SnS_3 and Cu_2ZnSnS_4 at a very early stage of the sulphurization process, so that the Sn is bound and cannot evaporate from the film. Only SnS_2 compounds near the surface would have the possibility to evaporate and lead to a slight Sn-loss. The latter assumption is supported by Weber [28], who found out that the Sn-S loss rate increases for the different phases in the order

$$Cu_2ZnSnS_4 \rightarrow Cu_4SnS_4 \rightarrow Cu_2SnS_3 \rightarrow SnS.$$

This means that excess tin cannot evaporate from the film in the same way as in the case of metallic precursors, but would either be bound in non volatile structures or encapsulated by the early formed CTS and CZTS phases. We therefore suggest that the excess tin would evaporate as SnS or SnS_2 for metallic precursors, while it would rather be enclosed as conglomerates or SnS_2 layer for ZnS precursors.

It is difficult to find a definite proof for this mechanism that we conclude from the different Sn-losses for metallic and ZnS precursors, but it is at least supported by the fact that all CZTS films showing clear SnS_2 signals in XRD (3 samples) were made of ZnS precursors.

4.2.2.2 Reproducibility

It is interesting to see how reproducible our sulphurizations are in order to evaluate to which extent we can control the sulphurization process. This is also important to verify whether we can draw conclusions from the observed compositional changes. During our experimental series, three precursors were sulphurized twice under exactly the same conditions to answer this question. We took pieces of the same precursor and subjected them to the same sulphurization on different days. The results for metal composition and efficiency are listed in Table 4.2.

It can be seen that our experiments are very reproducible concerning composition and also in efficiency. For this reason we assume that samples from the same precursors are comparable, which we will use for example in chapter 4.3.2 for the QE measurements.

Sample #	Cu	Zn	Sn	Efficiency
21 (metallic)	0,46	0,30	0,23	2,6%
23 (metallic)	0,46	0,31	0,24	2,7%
9 (ZnS)	0,48	0,25	0,27	2,5%
10 (ZnS)	0,48	0,25	0,27	3,2%
7 (ZnS)	0,47	0,25	0,28	1,8%
8 (ZnS)	0,47	0,26	0,27	1,9%

Table 4.2: The sample pairs #21 and #23, #9 and #10 as well as #7 and #8 were in each case made of the same precursor. The results for composition and efficiency show the reproducibility of our experiments.

4.2.2.3 Role of the substrate

All precursors were deposited on three substrates: silicon, glass, and glass coated with molybdenum. The precursors on the three substrates are assumed to be identical as they were sputtered in the same deposition process. The substrates lay on a rotating substrate holder, so that there should be no differences between the several substrates. Reason for this is the advantage of different substrates for different analyzing methods. For example suits the conducting silicon very well for EDS, while molybdenum-coated glass (Mo-SLG) is needed for making a solar cell.

In order to test possible differences of films deposited on Mo, Si and SLG, some EDS comparison measurements were done (chapter 3.2.2.1). Measured compositions of the (assumed) same films on Si and Mo as well as Si and SLG were compared to each other and the average deviation between the values was calculated. The difference is mostly below 6%, but in one case up to ca. 11% between same films on different substrates. This is within the error range we found for EDS (3.2.2.1). That means, that the composition of equally processed films on different substrates can be assumed to be equal, as the EDS results do not show more deviation between same films on different substrates compared the same film on the same substrate.

This is in good agreement with the results from chapter 4.1.1.2, where we could conclude that there was no difference in composition or compositional gradients between precursors on Mo and Si.

4.2.2.4 Summary

For our set of samples we observed Sn-loss during sulphurization. The Sn-loss is more pronounced for the metallic precursors. A possible explanation including a theory how CZTS is formed in our films was presented. As a result, it is assumed that a different formation pathway of CZTS in ZnS films (compared to metallic films) leads to enclosure of SnS_2 or other tin-rich secondary phases. For metallic precursors it is assumed that excess tin evaporates during sulphurization.

Furthermore we analysed the role of the substrate comparing the composition of films on glass, glass coated with molybdenum and on silicon. The conclusion was that the variation between composition on the several substrates lies within the error range of EDS.

One experiment was performed to find how reproducible our experiments are. This was done by sulphurizing pieces of the same precursors in different runs. The result showed a very high reproducibility regarding the composition and quite good concerning efficiency. For this reason we believe that the sulphurization process is stable with regard to composition, i.e. compositional changes like the observed Sn-loss should not depend on the day of sulphurization but have more fundamental reasons.

4.2.3 Morphology

In addition to the composition, the morphology of the sulphurized films is another important aspect that can help to understand the processes occurring during sulphurization as well as to reveal information about the film quality.

In this chapter we attempted to identify secondary phases by XRD and SEM combined with EDS, to examine the 'quality' of the CZTS films (grain size, voids, compactness), and to evaluate the influence of ZnS in the precursor. Measurements of the thickness of the CZTS layers and of a presumed molybdenum sulfide layer from SEM cross sections were also performed.

As a further aspect, the influence of the substrate for the morphology of the CZTS was studied.

4.2.3.1 Surface features

A SEM top view makes possible to identify secondary phases that precipitate at the surface. As mentioned before, analysis of final CZTS films on Mo was difficult as the samples were in most cases further processed directly after sulphurization to minimize oxidation. Films with CdS and ZnO as top layers, however, cannot be easily analyzed, as the top layers hide or at least attenuate the desired details.

For the surface features, we could distinguish between two appearances: round, more spherical features (Fig. 4.5 a)), and features that looked like small plates or flakes (Fig. 4.5 b)). Those two were the most common structures seen on the surface, and both were in the range of micrometers.

The round features were extremely Cu-rich. Compared to the average Cu content in the whole film, the amount of copper increased roughly 25 times (e.g. Cu/(Zn+Sn): 0,51→13,52). The other metals appear only in small amounts.

Unfortunately it is very difficult to distinguish sulphur and molybdenum with EDS as the peaks partly overlap. This is one of the reasons why EDS measurements were usually performed on silicon. Therefore we could not accurately determine the contribution from sulphur from molybdenum. However, it is very likely that this surface feature is $Cu_{(2)}S$. First, EDS indicates an increase of the sulphur and a decrease of the molybdenum

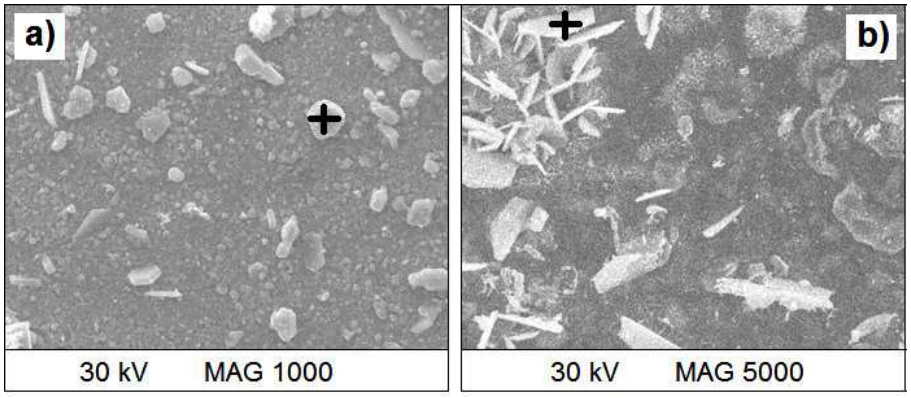

Figure 4.5: Surface features on CZTS films (substrate: Mo). EDS measurements were performed in the areas marked with a cross. a) shows round features that were very Cu-rich . Hence, it is assumed that these surface features are copper sulfides. In b) the flakes can be seen. As EDS measurements showed Sn-richness, these features are possibly tin sulfides.

signal, which would be expected when looking at a sulphur rich surface feature (i.e. the molybdenum signal should be more attenuated). Second, the combined Mo/S signal is still very strong compared to the average value of the surface, while Zn and Sn signal almost disappear. In the end, Cu_2S is frequently reported (e.g. [35]) to precipitate at the surface (see chapter 2.3.4), especially if the precursors is Cu-rich like in this case (Cu/(Zn+Sn) = 1,12 where 1 would be stoichiometric). For this reason we assume that we had formation of copper sulfides as secondary phases.

The flakes like structures shown in Fig. 4.5 b) are Sn-rich. The point marked in the image showed ca. 50% more Sn than the surrounding area, while the other metals were reduced by ca. 50%. The combined S/Mo signal increased (less Mo, more S). What we assume from this result is that we have $SnS_{(2)}$ flakes. The signal from Cu, Zn and Mo could result from the film below, considering that the flakes seem to be much thinner than the penetration depth of the electron beam. As the sample was slightly Sn-rich (Cu/Sn = 1,87 where 2 would be stoichiometric), this result seems to be plausible, and tin sulfides are apparently another possible secondary phase for our CZTS films.

4.2.3.2 Cross sections

Cross section studies of sulphurized films are an important and useful tool which provides an indication about material quality. They can give information about grain size, voids, compactness, homogeneity and uniformity of the film, which can potentially allow drawing conclusions about the material formation process, secondary phases and possibly disadvantageous structures or features.

Cross sections of all solar cells were made. However, it is often not easy to draw unambiguous conclusions. 25 solar cells are part of this study, and more than 200 SEM images were taken and analysed. Still, often only 3–4 images for each sample remained where the interesting aspect (such as grain size or surface features) could be seen clearly and accurately. Furthermore, the solar cells were cut only once, that means the images show only the structure along a single line. Therefore, it can of course not be excluded that in some other part of the cell different structures occur. The images should at least give an impression about the general appearance of the film, even if we have to exercise caution in drawing conclusions.

Grain size

It is often very difficult to determine the grain size from SEM images. Main problem is that the cross section does not show an even fracture plane, but a very square-edged side. It is often impossible to determine where grains begin and where they end, or whether several grains "overlap" in the image but appear as one; a general topographical problem when a three-dimensional structure is pictured in a two-dimensional image. Another problem is that it sometimes was not possible to get a sufficient contrast for the images (see for example Fig. 4.8 e)) due to charging effects, which made it nearly impossible to estimate grain size.

However, for most samples an impression could be received if the grains appear 'larger', by which we mean here clearly bigger than 0,5 µm, or smaller (less than 0,5 µm). In these categories, no clear trend for grain sizes related to composition could be found. As can be seen in Fig. 4.6, there exist large-grained samples in the Zn-rich, Cu-poor, stoichiometric and Sn-rich region of the phase diagram, i.e. in four of five regions of the phase diagram where we have made solar cells[1]. Only Zn-poor cells with reasonable grain sizes could not be found.

Comparison of samples with similar composition could give more specific insights in addition to the general conclusions. That could support – or disprove – the assumption that composition is not the driving force for grain size.

In Fig. 4.7 a) one can see a sample with Cu/Sn ratio of 1,69 and Cu/(Zn+Sn) ratio of 0,87, that is Cu-poor. It shows huge grains in the micrometer range. Next to it, in Fig. 4.7 b), a sample with almost the same composition from the same region (Cu/Sn = 1,66, Cu/(Zn+Sn) = 0,87) can be seen, and the grains are significantly smaller.

Another example with samples of similar composition but different in grain size can be seen in Fig. 4.27 b) and c) on page 87.

From this we conclude that composition is not a parameter that controls grain size in our experiments.

1 Actually, two solar cells from a fifth region of the TPD exists (Sn-poor), but no SEM-images were made for these samples.

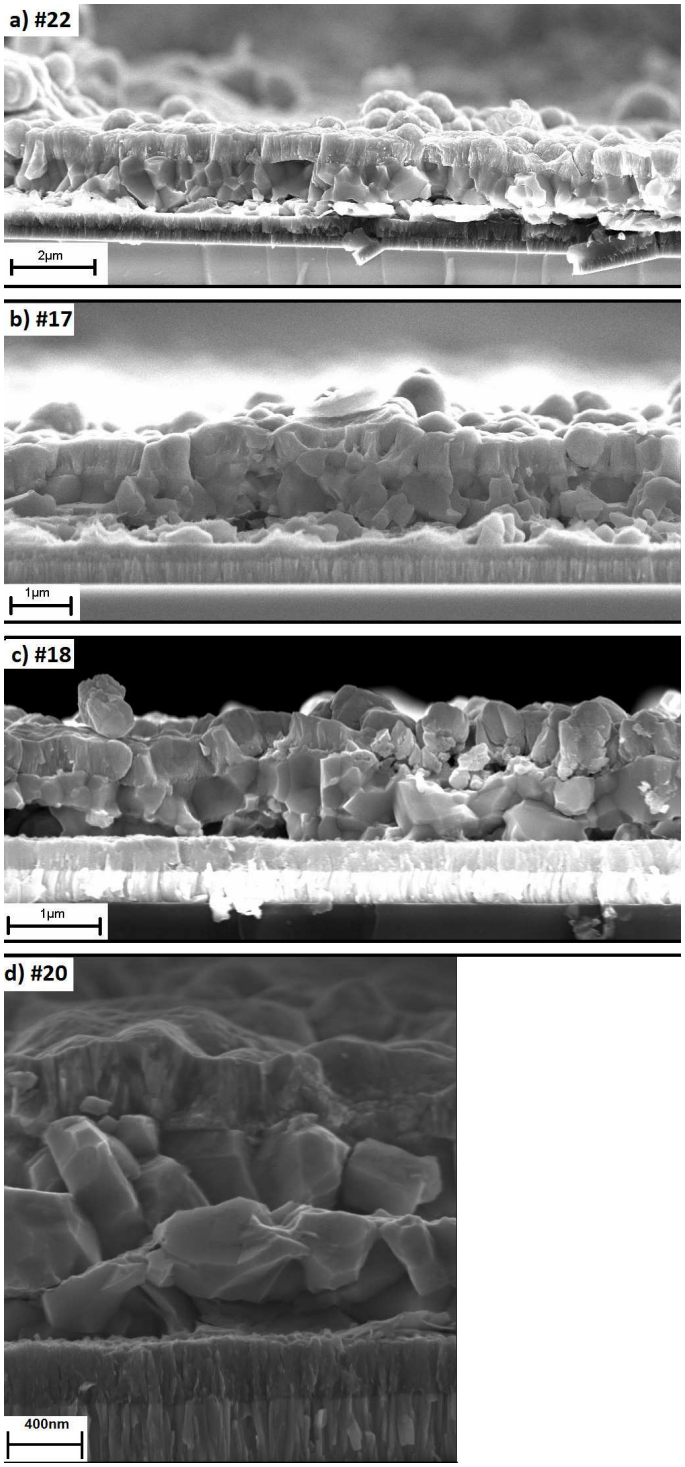

Figure 4.6: Solar cell cross sections from the a) Zn-rich, b) Cu-poor, c) stoichiometric and d) Sn-rich region of the TPD. It can be seen that grain sizes larger than 0,5 µm can be found in each of these regions. Inset are the sample numbers.

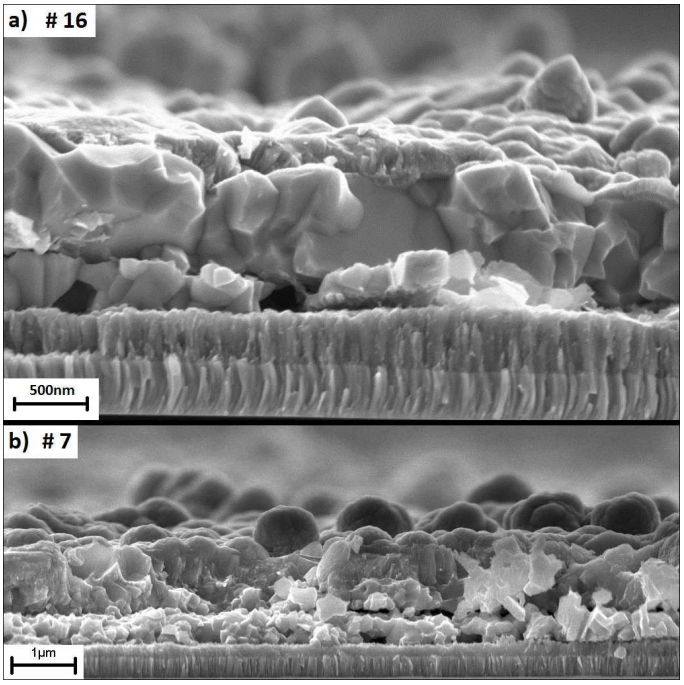

Figure 4.7: Grain size comparison for two Cu-poor samples near in composition. Even though the two samples lie in the same region of the TPD, the grain size is very different. Inset are the sample numbers.

Voids and compactness

Considerably easier to determine is if a film appears compact or shows a lot of voids. As for grain size, the composition seems to have no impact on the formation of voids or density of films. The Figures 4.8 a)–h) give an impression: a) and b) are Zn-rich samples, c) and d) Cu-poor, e) and f) stoichiometric, and g) and h) Zn-poor (for Sn-rich it was difficult to see a clear trend). The left image always shows a dense, compact film, almost without voids, while the right image from the same region of the phase diagram is more porous and shows (often huge) voids. Note that we consider three-dimensional holes; cracks between different layers like in c) are examined in the next chapter and do not count as voids.

Voids at the back contact are frequently seen for CZTS films (for example in [7]). As described in chapter 2.3.4 it is very likely that this effect results from Cu diffusion to the front, leaving voids within the film.

a) and b) as well as e) and f) are at the same time examples of samples that are very close in composition and still very different concerning compactness, as can be seen from Table 4.3.

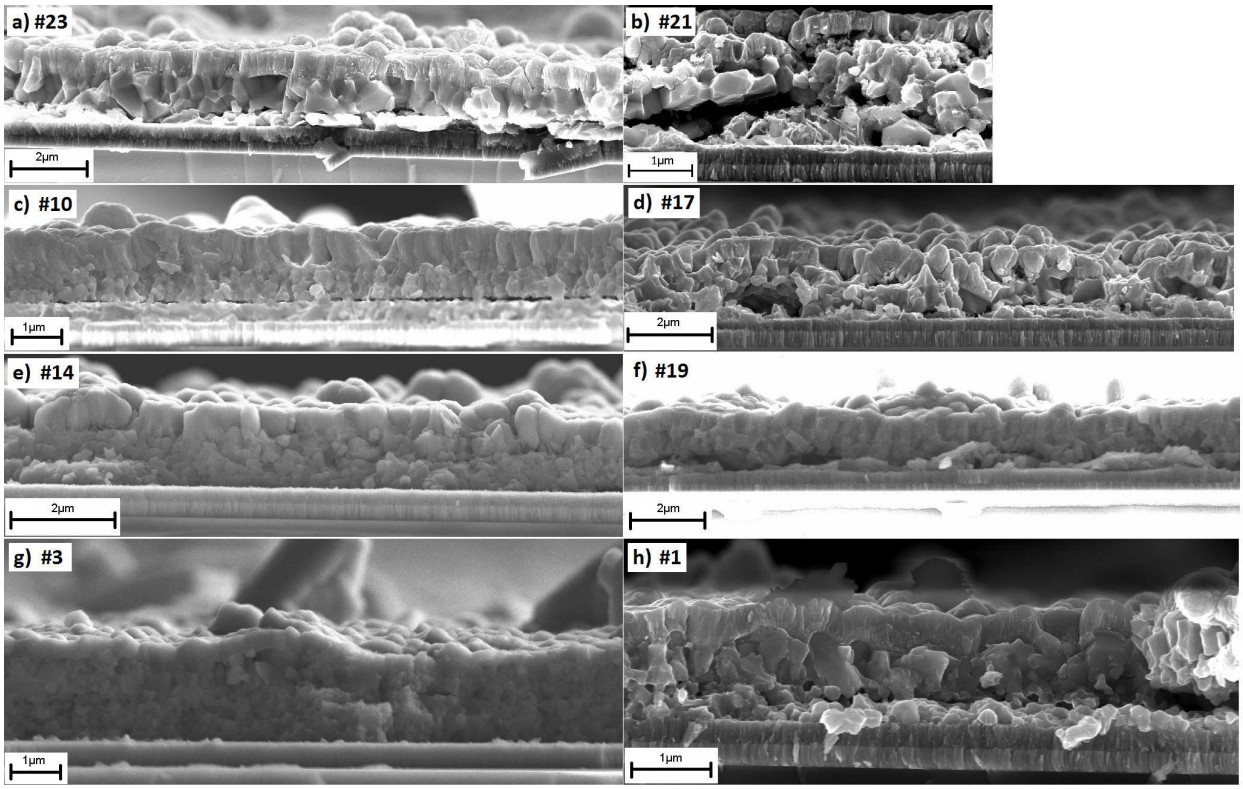

Figure 4.8: Void comparison for different regions of the TPD. a) and b) are Zn-rich samples, c) and d) Cu-poor, e) and f) stoichiometric, and g) and h) Zn-poor. Each left image shows dense films with no or only few voids, the right image films with large and/or several voids. Inset are the sample numbers.

	Cu/Sn	Cu/(Zn+Sn)
a (#23)	1,94	0,84
b (#21)	1,97	0,86
e (#14)	1,89	0,96
f (#19)	1,89	0,95

Table 4.3: Sample set with similar composition (concerns Fig. 4.8, for more information see the text). Samples #23 and #21 are Zn-rich, #14 and #19 stoichiometric.

Layering

In several cases we observed that the CZTS film was clearly divided into two or even three sublayers. This phenomenon we refer to as *layering*, as examplified can be seen in Fig. 4.10 (page 62).

Like for grain size and voids, we were interested in if the occurrence of layers in some way is connected to composition. For this we investigated all samples with respect to layering. In doing so we encountered the problem that many samples were not clearly defined, as layering was not very pronounced. Fig. 4.8h) for example might show layering or just a random accumulation of voids near each other. Another problem was when only some images of the same sample showed layering while others did not exhibit any such features. This class of samples was categorized as *ill-defined*.

Definite layering could be observed in all regions of the phase diagram that were covered in our experiments. Anyway, we had a closer look at samples where we could definitely *exclude* the existence of layering, and plotted samples without layering as one group (black in Fig. 4.9), and samples with or with unclear layering as another group (marked in blue). There is a trend that 'no layering' mainly occurs in or near the stoichiometric region (there is only one sample far off in the Zn-poor region). That means to avoid layering it could be helpful to end up not too far away from the stoichiometric region of the phase diagram, even if this cannot guarantee layer-free structures.

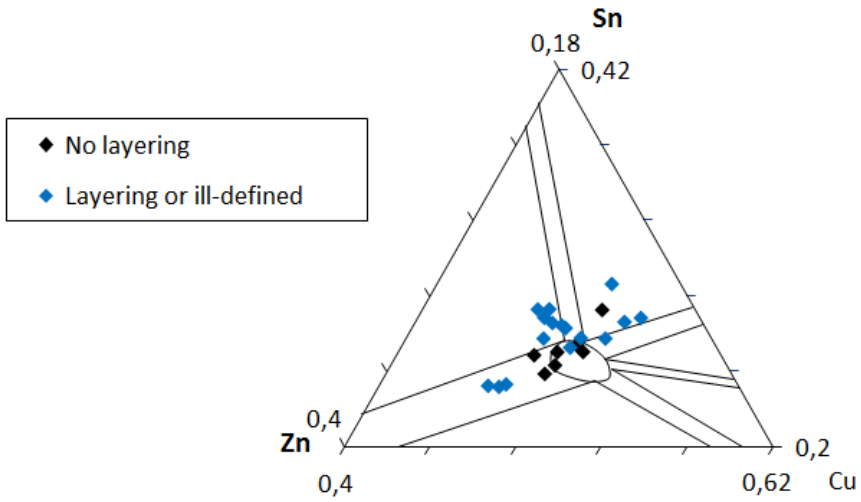

Figure 4.9: Composition (plotted in the TPD) of samples with no (black) and with clear/ill-defined layering (blue). Samples that definitely showed no layering are grouped in and near the stoichiometric region.

Of course it is of interest why layering occurs and especially if it just means a crack within the CZTS layer, or if the borderline actually separates two different phases. For this reason we examined one sample more closely.

Fig. 4.10 shows sample #10. The image illustrates what we refer to as layering: a crack divides along the whole image a top from a sublayer. Obviously the adhesion between these two layers is poor, as the top layer flaked off near the breaking edge (that is why the top layer is – contrary to the bottom layers Mo and glass – out of contrast). This adhesion problem was observed in several images and Fig. 4.11 shows it even more clearly: to the left is the bare substrate, next to it only the bottom layer is covering the substrate. The top layer including CdS and ZnO flaked off and starts in some distance away from the fracture edge.

Zooming in (Fig. 4.12) one can see that the sublayer seen from the top has a needle shaped structure in plane of the sublayer, which is different from the CZTS structure. That indicates that this layer is not CZTS but another, secondary, phase. EDS measurements reveal that while the top layer exhibits the expected Cu/Sn ratio of 1,9, the bottom layer is extremely Sn-rich: Cu/Sn = 0,28. Measurements of the whole film including the bottom layer gave 1,78; 67% of the metals in the bottom layer are tin. A determination of sulphur content was not possible due to overlap between sulphur and molybdenum. Although we cannot prove it, we strongly suggest that this layer contains large amounts of tin sulfide. There is no Cu-Zn-Sn-S phase next to CZTS known, especially not with those metal ratios, and no Cu-Zn-Sn phase either. On the other hand, the presence of pure Sn after 2 hours of sulphurization is very unlikely. Therefore it is likely that this layer consists mainly of SnS_2. This assumption is supported by the fact that XRD analysis for this sample shows the existence of a crystalline SnS_2 phase (see chapter 4.2.3.6, Fig. 4.17), and that precursor as well as final sulphurized layer are Sn-rich (Cu/Sn = 1,56 and 1,78, respectively, while 2 would be stoichiometric).

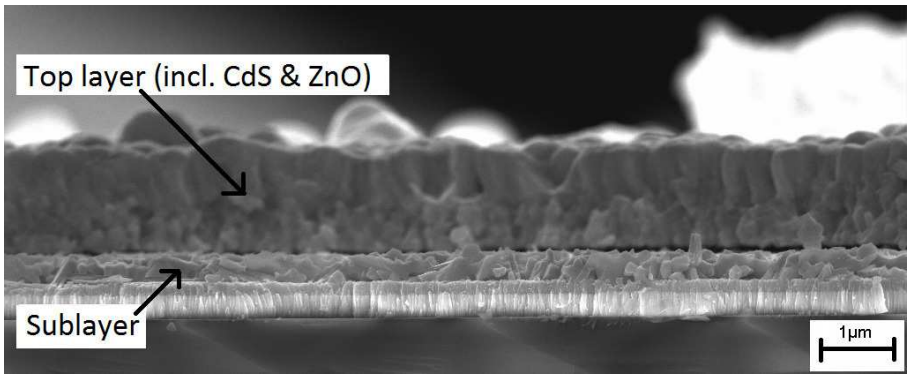

Figure 4.10: Cross section of sample #10. The film is clearly divided into two layers. The upper layer contain the (presumed) CZTS film as well as the CdS and ZnO layer.

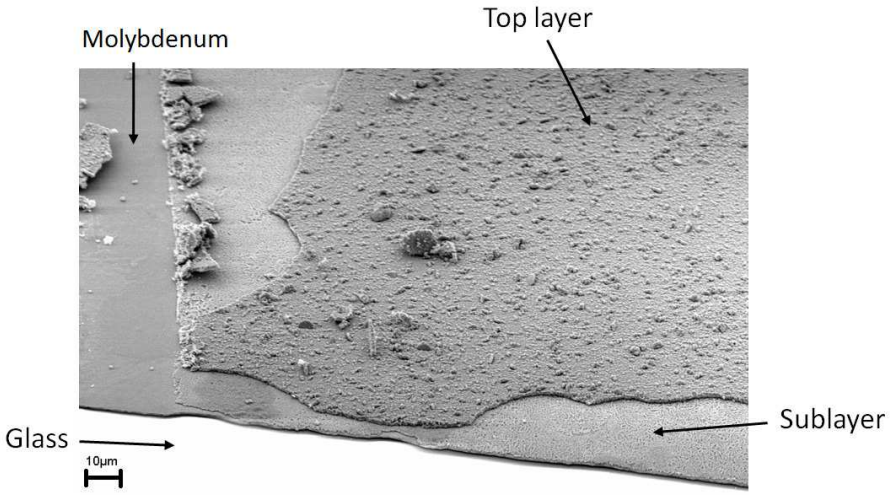

Figure 4.11: Top view on sample #10. The different layers can be seen as they partly separated from each other during the sample breaking. This shows also the bad adhesion between the sub and the top layer: near the breaking edge the top layer has flaked off, which caused the contrast problems that can be observed in Fig. 4.10.

This observation supports our considerations in chapter 4.2.2.1, where we suggested that ZnS precursors tend to keep their excess tin in form of tin sulfide as conglomerates or layers, while metallic precursors loose tin sulfide by evaporation early in the sulphurization process before it can be enclosed by CZTS.

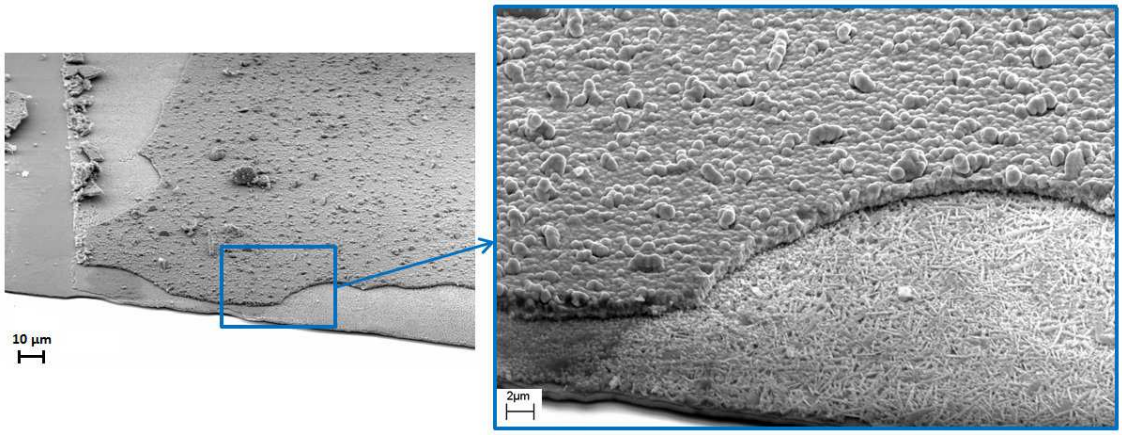

Figure 4.12: Zooming into the breaking edge. The sublayer has a needle shaped structure. EDS in combination with XRD measurements leads to the assumption that this layer is SnS_2.

Two more ZnS samples (#8&9) show layering in the way shown in Fig. 4.10 with bad adhesion between the two layers (#9 is shown in Fig. 4.13 a, bad adhesion arises from the flaked off top layer near the breaking edge), and for both samples SnS_2 was found by XRD as well. There is also a sample made of a metal precursor where the cross section could suggest two layers with bad adhesion, but XRD could not prove the existence of SnS_2.

Note that the considerations about this kind of layer concern only those mentioned three ZnS samples. There are other layer structures (see Fig. 4.13b)) that look different and where we cannot clarify if the layers consist of different phases. We assume that these different layers consist of CZTS divided by cracks, as the structures of the layers are very similar to each other. This kind of layering has also been observed in publications [7].

Summary

As grain size, voids and layering are assumed to influence the performance of a device we would like to be able to control these properties. However, a correlation with composition – the main parameter we changed in our experimental series – could not be observed. This was shown likewise for a general overview as for a comparison between each two samples very near in composition. Only Zn-poor samples were all small grained.

Layering, in contrast, might be avoidable by choosing (near-) stoichiometric samples. It is not always clear if the two to three layers are CZTS or consist of different phases, but combined EDS and XRD measurements indicate that at least for a part of the ZnS precursors the bottom layer is mainly tin sulfide.

The question in which way efficiency is influenced by those morphological parameters is discussed in chapter 4.3.1.2.

Formation of molybdenum sulfide

In all of our cross sections we observed that the molybdenum film is discoloured at the top after sulphurization. We assume that this discolouring results from a sulphurization of the molybdenum, i.e. we suppose that molybdenum sulfide (more precisely: MoS_2) is formed. This assumption is supported by XPS analysis (see Appendix, Fig. A.5), where an

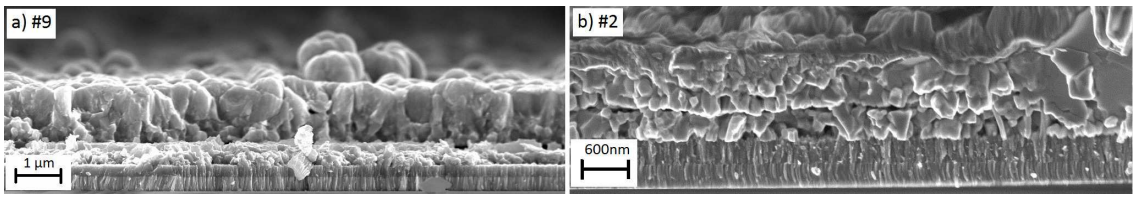

Figure 4.13: Different layer structures observed in this study. a) shows layering where the sublayer has a different structure and where the adhesion between sub- and top layer is poor. b) shows layering that supposes same material, and the top layer is not flaked off which suggests better adehesion than in a).

increase of the Mo signal can be seen, while the S signal is still unchanged and decreases significantly deeper in the film and slower than the metals Cu, Zn and Sn. That means that Mo and S coexist in a certain area and supports our assumption.

4.2.3.3 The influence of sulphur in the precursor

The substantial difference between our two experimental series was that we used a ZnS target instead of the Zn target in the second series. The aim was to incorporate sulphur already into the precursor, expecting that the film is subjected to less diffusion of the elements and so to less dramatical changes within the film (see chapter 2.3.4).

In our case the fraction of S in the precursors varied between 14 and 20%. The sulphurization process remained the same to assure that the results are comparable to the experiments with the metallic precursors.

General impression

It is not straightforward to get an objective overview about the possible difference between metallic and ZnS CZTS-films. However, the fact that it is difficult to see a general difference between these two types of films means that the use of ZnS actually did not make any major improvement in our experiments. Especially considering grain size it seems more that the impact could even be the opposite, i.e. that grain size for ZnS films rather decreased. Most ZnS samples show grains not bigger than half a micrometer, bigger grains are nearly exclusively observed for metallic films. Concerning voids and compactness, there actually seems be a slight trend. With only one exception, all metallic films show voids, often even very large ones, while ZnS films tend to produce less and smaller voids. The latter is probably related to less diffusion of Cu to the surface (see chapter 2.3.4). Furthermore, the ZnS samples are smoother, i.e. show less variation in thickness (see chapter 4.2.3.4). Fig. 4.14 gives an impression of the described effect. a) shows a metallic film, b) a film made of a ZnS precursor.

Hence, the general conclusion is: ZnS precursor show a trend to more compact films with smaller grains as well as less and smaller voids.

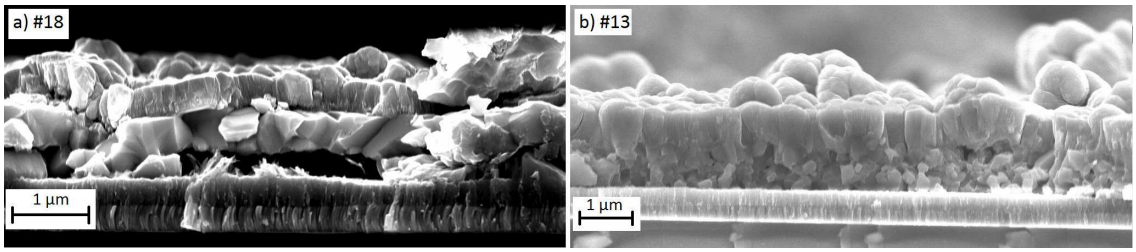

Figure 4.14: Illustration of the general impression that metallic precursors a) tend to have larger voids than ZnS precursors b).

Comparison of similar compositions: Experimental matrix

When comparing all samples for a general discussion one should keep in mind that composition is the main parameter and that it is not possible to distinguish between the impact of the S in the precursor and the composition of the films. To support the results from the previous chapter it would therefore be illustrative to compare samples with as similar precursor compositions as possible. For this reason we made an experimental matrix with metallic and ZnS precursors from the same region of the phase diagram. Same composition means in this case the ratios between the metals; as only one kind of precursors contains sulphur, the overall composition is of course not the same. More information about the chosen samples is provided in Table 4.4. Two pieces of the same ZnS precursor were sulphurized two times under the same conditions, which is why we have two samples to compare with here. As can be seen, all samples keep similar composition after sulphurization, which makes the comparison sensible.

Fig. 4.15 shows the cross sections of the three sulphurized films, a) made of a metallic precursor, b) and c) the ZnS ones. An increase in grain size cannot be stated, rather the opposite: while the grains in sample #17 are noticeable larger than 0,5 µm (often up to ≈0,9x0,7 µm), the grains for the ZnS samples #9 and #10 are difficult to estimate but already limited by the obvious layering to sizes less than 0,5 µm. The impression is that the grains are even smaller than that. On the other hand, comparing #17 and #10 could support the general impression of the previous chapter that ZnS films are more compact and contain less and also smaller voids. The result is not very clear for sample #9, the crack within the film seems to be the origin of voids that reach into the CZTS film. Sample #9 illustrates also very well both the difficulty to distinguish clearly between for example voids and cracks, and also that the use of ZnS could not prevent voids in every case.

Next to this example from the Cu-poor region, ZnS and metallic samples with similar composition from the Zn-rich and stoichiometric region were compared. They are not discussed here[1] but showed the same impression as described for the samples above: no increase in grain size, but films that are more compact and show fewer large voids.

	Precursor		Sulphurized	
Precursor # and type	Cu/Sn	Cu/(Zn+Sn)	Cu/Sn (sulph)	Cu/(Zn+Sn)
#17 (metallic)	1,53	0,83	1,79	0,89
#9* (ZnS)	1,56	0,86	1,76	0,91
#10* (ZnS)	1,56	0,86	1,78	0,92

Table 4.4: Sample set with similar composition that is examined to analyse the impact of sulphur in the precursor on film morphology. They were chosen to minimize the influence of the composition. Samples marked with an asterisk (*) were made of the same (ZnS-) precursor, sample #17 is made of a metal precursor.

1 Fig. 4.8 e) (ZnS) and f) (metallic) show a cross section, though

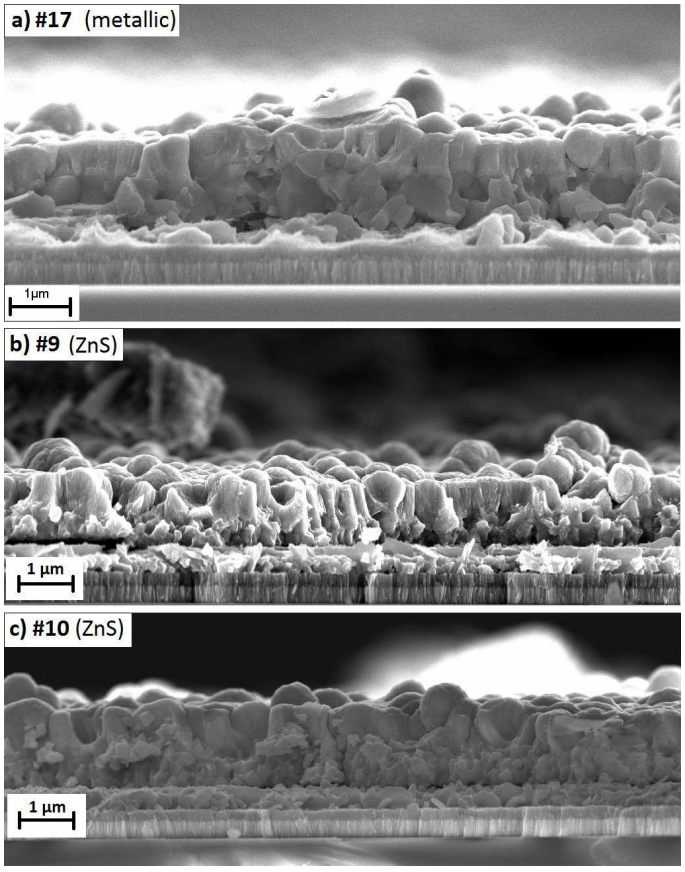

Figure 4.15: Metallic (#17) and two ZnS (#9 and #10) CZTS films. No increase in grain size for the samples that contained S in the precursor can be observed. Instead, a trend to smaller grains and more compact films is visible, especially comparing #17 and #10.

Summary

Both the general overview and the experimental matrix with similar-composition samples indicate that replacing Zn with ZnS in the precursor does not increase grain size but rather leads to even smaller grains. However, the use of S in the precursor appears to lead to more dense films with less or smaller grains, even if that is a weak trend. Further work could enlighten this question by an extended series with metallic and ZnS samples that are very close to each other in composition to exclude compositional effects.

4.2.3.4 Thickness development

Both the metallic and the ZnS precursors contained less sulphur than needed for CZTS. For this reason, the film is subjected to strong expansion: CZTS has a lower density than

the metals, and up to 50% of the final number of atoms has to diffuse into the film and build structures under sulphurization (see chapter 2.3.4).

To get an idea how strong the changes within a film are when CZTS is formed under sulphurization, it can be helpful to evaluate the expansion from the precursor to the final CZTS film and look at surface features as well as roughness of the film.

The thickness data for all samples can be found in Table 4.1. The expansion for *metallic* precursors varies from just less than 2 up to even 4 times. At the same time, the CZTS films are in most cases very uneven so that expansion factor could vary a lot between different areas of the same sample. In the most extreme cases, the expansion was between 2 and 4 times, depending on the considered area. On average, the maximum and the minimum thickness measured for one sample varied around 50%. On the other hand only two of the nine samples showed remarkable surface features on the viewed images.

The impression for the *ZnS* precursors is, in contrast, that the expansion of the films was less dramatic than for the metallic ones. First, the increase in thickness was except of one case in maximum 2,5 or less. In most cases the expansion was around two, which was the lower limit for the metallic precursors. This is not surprising as the ZnS precursors already contained up to 20% sulphur, so less incorporation of additional material was needed. Second, the ZnS films were in general smoother, that means they had less hills and valleys and also showed less thickness variation between different images. In average, the thickness for a sample varied around 25%, i.e. only half of the value found for the metallic films. However, it should be noted that almost all ZnS samples showed enormous surface features at some parts and piling up of material. This structure resembles the surface features seen in Fig. 4.5 b), and therefore it might be tin sulfide. However, deeper analysis would be necessary and could be part of future work.

In conclusion, the use of ZnS in the precursor obviously leads to smoother films and at the same time decreased expansion of our films. Considering that expansion always can cause stresses and cracks within the film and that a film that is more even and shows less distortion probably is desirable, this is a beneficial effect of S incorporation in the precursor. At this point, the origin of the obviously increased surface features for ZnS films is unclear. Further experiments could focus on finding out their nature and the possibility to remove them, for example by etching. This might increase the performance of the solar cells. Moreover, stresses within the films could be measured to reveal if ZnS films show less of it, which might be assumed as the expansion is lower.

4.2.3.5 Role of the substrate

In chapter 3.2.2.1 we showed that – within the error range – the composition of the films deposited on silicon, glass and glass coated with molybdenum are the same. That is expected as for each sample all the three substrates were sputtered in the same run.

However, even if the samples were then sulphurized in the same run, the morphology does not have to be the same. We would rather expect that the substrate plays an important role for the growth. First, the orientation of the substrate crystals might influence the

grain growth; second, elements from the substrate could diffuse into the CZTS, which can potentially have major influence on the film quality. For example it is known for CIGS that sodium has a beneficial effect on the material such that films grown on sodium free glass or other substrates need supplementary Na to achieve same efficiency [53].

Therefore, it was not surprising that the cross sections for the different substrates revealed completely different images. Typical images for the three substrates coming from the same precursor deposition are shown in Fig. 4.16.

Fig. 4.16 a) shows a CZTS film on molybdenum substrate. Note that it shows a final solar cell, i.e. there is a top layer of ZnO (CdS is too thin to be seen), even though it varies in thickness. The film shows relatively large grains that are clearly defined. The surface is quite even and no larger surface features can be seen. There are few voids and the films seem to adhere to each other.

b) shows the corresponding film on silicon. No further layers like ZnO were deposited here. The adhesion to the substrate appears to be very poor. Some voids can be seen; some other pictures show a more porous structure. The grain size is very small, in most cases only one to two hundred nanometers, but it is very difficult to estimate it as the grains are not as well defined as for the Mo-substrate. Some surface features could be observed.

c) shows CZTS grown on glass substrate. In this image, the substrate cannot be seen as the film peeled off from it. Other pictures showed better adhesion, but never as good as for the Mo. The grain size seems to be a mixture of what was seen on Mo and Si: Some larger, well-defined grains, next to extremely small grained without contours. Most conspicuous are, however, the gigantic surface features and distortions that dominate the image. Other images support the existence of unidentified surface features in the micrometer range and show huge voids where the film still adhered to the glass.

Summary

It should be noted that these conclusions were not drawn only on the basis of the three presented pictures. They served only to illustrate a general trend that was observed on several samples.

Film growth and quality appear to be completely different for each of our substrates. Fortunately, the by far best results are achieved for molybdenum coated glass, which is quite satisfying as these are the substrates we used for solar cells. Films grown on silicon showed much smaller grain size and were partly lifted up from the substrate as a result of poor adhesion. As these films only were used to measure composition with EDS, this is not a basic problem, as composition was shown not to vary significantly between the substrates. The glass substrates, however, which were used for XRD measurements (see next chapter), showed a clear difference in appearance. We cannot exclude occurrence of different secondary phases as compared to Mo. Especially for the surface features we could not identify if they consist of secondary phases that on Mo substrates where enclosed into the film, or if growth on glass enhanced the appearance of further secondary phases. It is

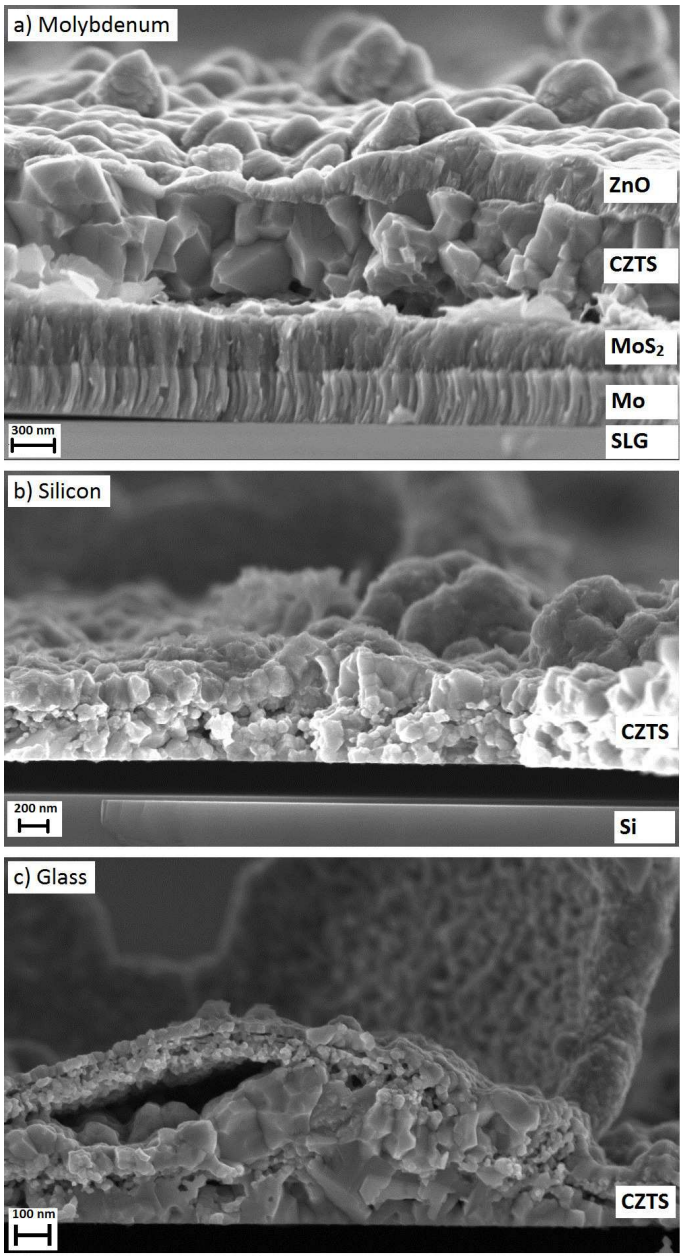

Figure 4.16: Comparison of CZTS films on different substrates. a) On Mo: The film looks quite even and has only few voids. The adhesion between the different layers is good. b) On Si: The adhesion between CZTS and substrate is very poor. The grains are considerably smaller than on the Mo substrate. c) On SLG: The films is completely lifted off. The film is very uneven, large surface features can be observed. Grain size is a mixture of very small and some larger grains.

possible that these structures are related to the surface features seen in Fig. 4.5 b), which would mean that they are probably tin sulfides. However, further work would be required to identify these secondary phases; for this we have examined too few samples.

4.2.3.6 XRD analysis

The analysis of samples by XRD can provide important insights in the structure of films. Especially the identification of crystalline secondary phases is a powerful tool that is not possible with other analyzing methods used. However, the drawback of this technique is that XRD results are difficult to interpret in cases of peak overlap and multiple-phase systems. As discussed in more detail in chapter 3.2.4 crystalline phases show several peaks in X-ray diffraction. Different phases can show overlapping peaks, as in this thesis CZTS, CTS and ZnS. They cannot be distuingished in our XRD analyses.

Not related to XRD, but an issue in our case, is that all measurements were performed on glass, only few samples got an additional measurement on Mo or Si. Even though they did not show any fundamental difference to those on glass, no hypothesis shall be educed only from XRD measurements.

The first result is that all of our sulphurized samples showed the Σ–signal. As mentioned, this is not a definite proof of CZTS, but as the composition is always close to CZTS stoichiometry and we could in most cases produce working cells with a band gap of roughly 1,6–1,7 eV (see chapter 4.3.2.2), i.e. the presence of CZTS is very likely. Cu_2SnS_3 as single phase would give a different band gap ($\approx 0{,}9$ eV) and has a completely different composition. For this reason we assume to have mainly CZTS. CTS and ZnS might occur as secondary phases (from the phase diagram in Fig. 2.16 we would expect ZnS for Cu-poor and Zn-rich samples and CTS for the Zn-poor ones) and increase recombination or reduce the active area, respectively.

The second observation is that all samples show additional peaks next to the Σ–signal. The spectrum reaches from one additional peak to more than ten. We conclude this means that we never obtained phase pure CZTS, not even in the cases where the samples lay in the stoichiometric region of the phase diagram and the absence of secondary phases might be assumed.

Concerning identification of the secondary phases, our third conclusion from XRD measurements is that it appears that most peaks cannot clearly be assigned to a certain phase. There are only four cases where we believe that we can claim to have found a certain phase.

Three samples show signals that can clearly be assigned to SnS_2 (hexagonal structure) as a secondary phase (Fig. 4.17). All samples lie in the Sn-rich (or Cu-poor, respectively, which is still on the opposite side of Sn-rich) region of the phase diagram, i.e. compositional measurements support this result. Deeper analysis shown in chapter 4.2.3.2 could at least for one of these three samples show that the secondary phase SnS_2 is present as a layer under the CZTS. For the other two samples there is a strong evidence from images of the cross section.

In the XRD pattern of one sample, CuS (hexagonal structure) could be found (Fig. 4.18). This sample was in the Sn-poor region of the phase diagram where copper sulfides would according to the TPD (Fig. 2.16) would be assumed.

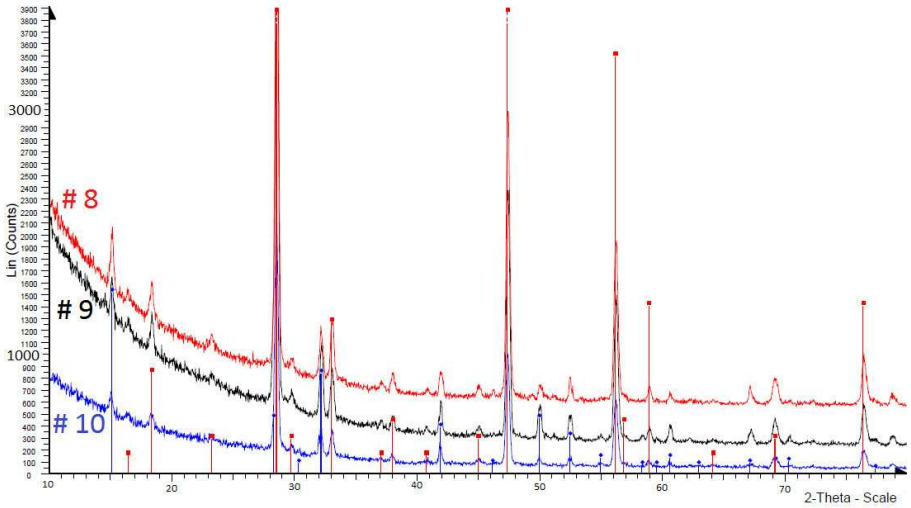

Figure 4.17: Samples #8 (red line), #9 (black) and #10 (blue). The red vertical lines indicate the kesterite structure. These samples matched to the SnS_2 signal (Berndtite-2T SnS_2, hexagonal structure) which is inset with blue vertical lines.

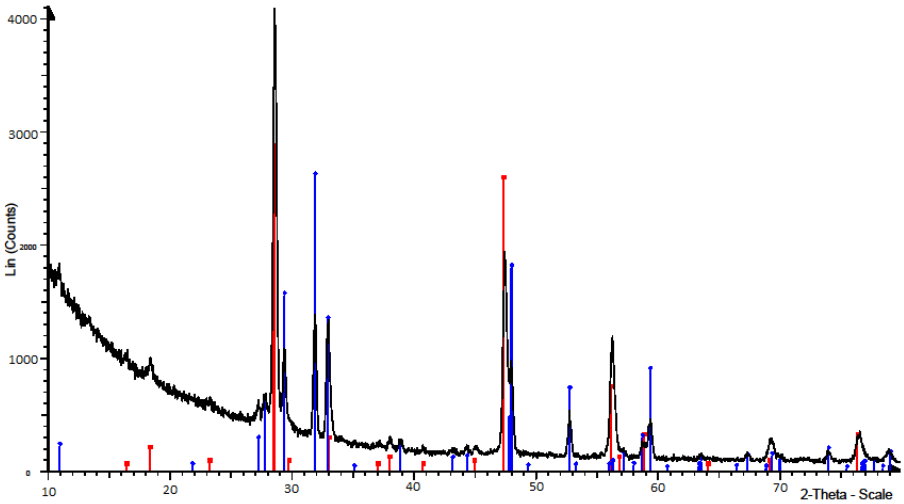

Figure 4.18: Sample #24. The red vertical line indicate the kesterite structure. This sample matched to the CuS signal (hexagonal structure) which is inset with blue vertical lines.

Summary
XRD analysis show – in combination with other analyzing methods like EDS – that CZTS is most likely the main phase in our films. All samples show also additional signals that cannot be assigned to the Σ–signal, though. In most cases we could not clearly identify secondary phases. In three cases, however, SnS_2 could be found; one sample shows copper sulfide. All these secondary phases are supported by what can be expected from the samples' position in the ternary phase diagram.

4.2.4 Conclusions

All sulphurized films were subjected to SEM and XRD analysis. The main focus was on the examination of the cross section pictures from which we drew conclusions concerning morphology (grain size, voids etc.), especially relating to composition and the use of ZnS in the precursor.

Taking all samples into account, composition had no influence on grain size, voids and compactness of our samples, with the only exception that Zn-poor material showed no films with big grains at all. The only impact of composition on morphology could be seen for layering, where (near-)stoichiometric films tended to show less layering.

Concerning secondary phases we can state from XRD that no sample could be proven to be phase pure CZTS, because additional peaks were always seen, even if they could not clearly be assigned to a certain phase. It has to be noted that XRD was done on glass, though, and SEM pictures showed a different film structure for glass samples. Therefore, this conclusion does not have to be valid for the solar cells. On the other hand, even the absence of additional peaks in the XRD pattern does not prove the absence of secondary phases as they can be amorphous.

For the layering, however, XRD results match to the observation that several ZnS samples show a sublayer of SnS_2. There were three samples that lay in the Sn-rich region, showing a sublayer that looked different from the (supposed CZTS) top layer and at the same time had been proven to contain SnS_2 by XRD. For one sample the existence of SnS_2 in the sublayer could even be confirmed by EDS. These results support the assumption from chapter 4.2.2.1 that ZnS samples rather enclose excess tin as secondary phase while metallic samples loose excess tin mainly by evaporation of tin sulfide.

One sample far away from the Cu-poor region showed copper sulfide as secondary phase in XRD. This and the results for SnS_2 indicate that XRD obviously needed larger amounts of secondary phases to reveal their existence.

Further secondary phases could be found on the surface of films. Compositional measurements with EDS suggest here that these surface features are copper- and tin-sulfides as well.

One important aspect in our experimental series was to examine the influence of sulphur in the precursor by using a ZnS instead of a Zn target for sputtering. The conclusions we could draw were that those ZnS samples did not produce larger but rather smaller grains. Instead, more compact films with less voids have been observed, although this

is more a trend and not valid for each sample. Another consequence was that the films were subjected to less expansion during the sulphurization process due to less integration of further sulphur. This led to smoother films with less thickness variation as well (but possibly more surface features). As discussed in more detail in chapter 2.3.4, those beneficial effects of incorporated sulphur in the precursor are due to less Cu diffusion to the surface, which would leave voids within the film.

MoS_2 could be found as an additional layer on the Mo.

In conclusion we can say that it was possible to control film quality only to a very limited extend. The use of ZnS in the precursor could reduce voids and increase compactness; the choice of films that lie in the stoichiometric region of the phase diagram might reduce layering and the formation of secondary phases. As secondary phases copper- and tin-sulfides could be identified for our samples.

However, these results concern only the appearance of the material. The next chapter will enlighten the impact of these parameters on efficiency, which is after all the most important parameter for a cell.

4.3 Solar cells

The final analyses that was done concerns the solar cell performance. The most important aspect for us to evaluate the quality of the cell is the efficiency, determined from IV measurements. Next to it, also QE measurements were performed.

4.3.1 Efficiency

To get an overview about the efficiencies of our fabricated solar cells, the phase diagram is a very helpful tool. Especially trends in terms of composition can much easier be discovered than from the raw data.

Fig. 4.19 shows the phase diagram with all our samples that were part of this study. They are classified in different efficiency groups and for it marked with colours. The black points symbolize cells where no efficiency could be measured, for example because they were completely shunted. All cells with better efficiency up to $< 1{,}2\%$ are marked in brown, with 1,2% and more up to $< 2\%$ in dark green, and the best cells with more than 2% efficiency are shown in blue.

It is conspicuous that Zn-poor samples obviously gave really bad results, there was only one cell that was working at all (0,1% efficiency). A bit more surprising is that cells within the stoichiometric region of the phase diagram are not really good either. Except of one sample they have all efficiencies of 0,5% and less. The exception has 1,1% and is the sample nearest to the Zn-rich region. This observation goes with the fact that the best solar cell efficiencies can be found in the Zn-rich region, in average slightly better than those from the Cu-poor region. For this reason we conclude that we have a clear trend that – to a certain extend – more Zn in the film increases the efficiency.

To illustrate this we plot the measured efficiencies against the Zn content, more precisely against the Zn/(Cu+Sn) ratio. Included are Zn-poor, stoichiometric and Zn-rich samples. The plot can be seen in Fig. 4.20 and supports the first impression from the phase diagram: An increase of the Zn-content leads to an increase in efficiency.

However, it has to be noted that this observation refers to samples that have (almost) the same Cu/Sn ratio. Spoken in terms of the phase diagram one would say they lie on a *pseudo binary tie line*[1], which is plotted red in Fig. 4.21. Looking for example parallel to that line above the stoichiometric samples, there are samples in the Sn-rich and Cu-poor region that have efficiencies comparable to those from the Zn-rich region, even though they have a lower Zn/(Cu+Sn) ratio.

1 The pseudo binary tie line is a line that assumes the presence of only two components (here: Zn and a Cu-Sn phase), where the amount x of the one component and the amount 1–x of the other component are existent. That is for example that $x = 1$ would mean presence of only one of the two components. The Cu-Sn phase or the Cu/Sn ratio, respectively, has in this case to be constant; otherwise one would end up above or below the pseudo binary tie line.

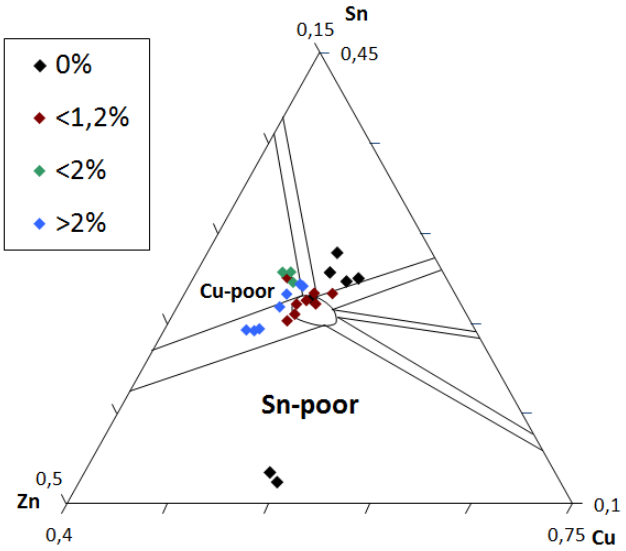

Figure 4.19: TPD with all samples of this study ordered by efficiency. While samples from the Zn- and Sn-poor as well as from the stoichiometric region are almost without exception poor in efficiency, the best cells come from the Zn- and Sn-rich as well as from the Cu-poor region.

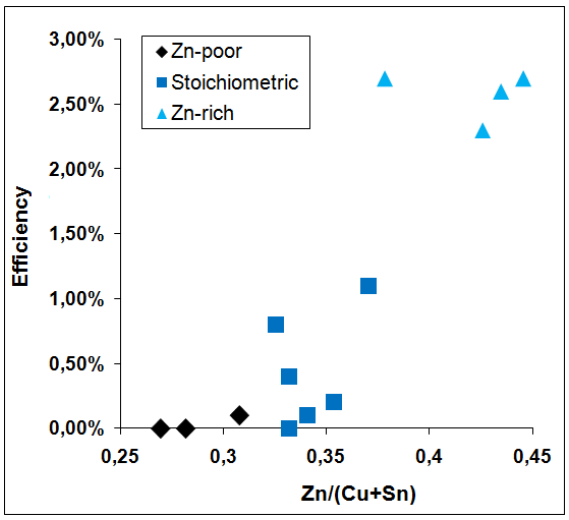

Figure 4.20: Influence of Zn content on efficiency. A clear increase of efficiency with increasing Zn content is observed.

Unfortunately we don't have enough samples to make a plot like in Fig. 4.20 for a parallel pseudo binary tie line like the light blue dashed one in Fig. 4.21. More data points for example in the region that is marked with an 'X' would be needed for this. Future work could examine this very interesting aspect that has so far not been shown in literature.

Considering physical reasons for the observed trend it is not that surprising anymore. A deficiency of Zn means – provided a sufficient amount of sulphur like assumed in our experiments – that Cu-, Sn- and Cu-Sn- sulfides are formed. Especially compounds containing Cu, like CuS or Cu_2SnS_3 turn out to be metallic ([31], [33]), which is detrimental for a solar cell. Conglomerates of those Cu-compounds that extend over the space charge region would let the electrons flow back directly and they would recombine with the holes before they could do work at a load. This is referred to as *shunting*.

Looking at the Zn-rich region of the phase diagram, ZnS is supposed to appear as secondary phase. ZnS is a less harmful secondary phase (see chapter 2.3.3) as it is a semiconductor with a band gap of 3,54 eV. That means that in most cases it would just act isolating, and by this 'only' reduce the active area, but at least would not shunt the sample.

This consideration shows: As we assume that we in all of our films have secondary phases (see chapter 4.2.3), it would be preferable to end up with the least harmful ones. ZnS might be such a secondary phase. For this reason samples should preferably not come from the Zn-poor region, to be on the safe side perhaps even from the Zn-rich side. This approach is strongly supported by our results.

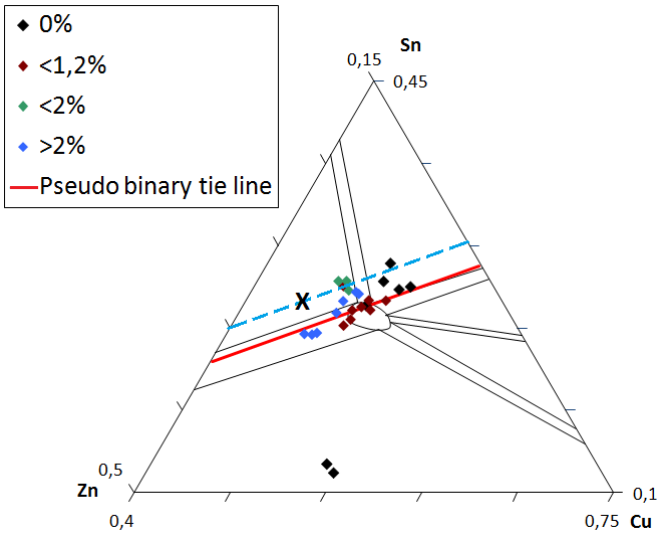

Figure 4.21: Pseudo binary tie line (PBTL, line of constant Cu/Sn ratio, red). Increasing Zn content (left direction) increases efficency of the cells. The blue dotted line is a PBTL for a different Cu/Sn ratio. A region where samples would have been needed for an extended analysis of the influence of the Zn content on efficiency is marked with an 'X' .

For samples that are not on the red pseudo binary tie line in Fig. 4.21, one can at least see that samples that lie in regions of the phase diagram where no Cu- or Cu-Sn-sulfides would be expected show much better efficiencies than those in the Zn-poor region. For a real trend more data points with a higher Zn/(Cu+Sn) ratio would be needed, though.

Note: Of course we suspect that this trend will be beneficial only to a certain Zn/(Cu+Sn) ratio and then make the efficiency drop again.

The two samples lying in the Sn-poor region of the phase diagram are negligible as they are so far away from stoichiometry which results in 0% solar cells. Most probably copper sulfides shunt the cell; this secondary phase is both expected from the TPD (Fig. 2.16) and has been found by XRD (4.2.3.6).

More interesting is that – next to the Zn-rich region – also in the Sn-rich and the Cu-poor region near the Sn-rich region very good solar cells were produced. The secondary phase found here with XRD (4.2.3.6, 4.2.3.2) was SnS_2, which is a semiconductor with a band gap of 2,2 eV (2.3.3). This secondary phase is less detrimental for the solar cell than metallic phases like copper sulfides.

4.3.1.1 Influence of sulphur in the precursor

Like for the morphological considerations, the influence of sulphur already in the precursor shall be examined in respect of efficiency as well. As we concluded from the studies of the cross sections (4.2.3.3) sulphur in the precursor leads in our case assumedly to smaller grains, but more compact films with less voids. However, next to the question if one would assume rather compact films or films with large grains to be better for a good solar cell, at this stage we want to consider the correlation ZnS precursor $\leftrightarrow$ efficiency from a general point of view, not taking into account morphological parameters. This is done in a further chapter (4.3.1.2).

General impression

As we have seen from the last chapter (4.3.1) the composition has a major influence on the efficiency. Zn-poor and stoichiometric samples give rather poor cells, while Zn- rich and Cu-poor cells show in general relatively high efficiencies[1]. Therefore it is reasonable to take this into account comparing metallic and ZnS precursors.

In Table 4.5 the average efficiencies for metallic and ZnS precursors ordered by phase diagram region is listed. No solar cells made of metallic precursors lay in the Zn-poor region, so here is no comparison possible. For the other regions the average efficiency for ZnS samples is (slightly) better than for the metallic ones, but the number of samples (mostly 2–5 samples per each precursor and compositional region) requires being careful in drawing major conclusions from this. The comparison of samples very close in composition

1 There are two samples that would actually be referred to as "Sn-rich". As only two samples would not allow to see a trend here and as they lie on the border to the Cu-poor or stoichiometric region, respectively, they are just added to these categories in this case.

might support or disprove this trend. This will be done in the next subchapter. For the general overview, however, we state that in average a slightly higher efficiency in favour of the ZnS cells could be observed.

Comparison of similar compositions: Experimental matrix

The same samples that were used to find morphological differences between metallic and ZnS samples very near in composition in the chapter 4.2.3.3 will now serve to consider correlations between efficiency and sulphur in the precursor. Table 4.6 shows the examined solar cells. #17 is made of a metallic precursor, #9 and #10 were made of the same ZnS precursors, but in different runs (same sulphurization conditions, though). The composition can be considered as very close.

The ZnS samples show better efficiencies. However, one has to take into account that the two ZnS samples #9 and #10 differ more from each other than metal sample #17 and ZnS sample #9. This makes it again very difficult to draw an unambiguous conclusion, but it at least does not contradict the weak trend from the general consideration that ZnS samples are slightly better, but rather supports it.

Summary

The influence of sulphur in the precursors was analysed regarding efficiency. The general overview, where the solar cells were grouped by compositional regions of the phase diagram, as well as a comparison of samples near in composition lets us assume that there is a slight improvement by using ZnS precursors. However, experiments with a larger set of samples than it was possible to do in this work would be needed to prove or disprove this trend.

	Cu-poor	Zn-poor	Stoichiometric	Zn-rich
Metal	1,3% (2,1%*)	–	0,4%	2,0%
ZnS	2,3%	0,02%	0,5%	2,7%

Table 4.5: Average efficiency of metallic and ZnS precursors from the different regions of the phase diagram. One can see a slight trend that ZnS samples produce better efficiencies. No Zn-poor metallic films were sulphurized.
*All Cu-poor samples have an efficiency between 1,8% and 3,2%, with only one exception. As one of the 2 metal samples has only 0,5%, this lowers the metal average efficiency from 2,1% to 1,3%. It is likely that this sample is only an outlier.

	Cu/Sn (sulph)	Cu/(Zn+Sn) (sulph)	efficiency	category (TPD)
#17 (metal)	1,79	0,89	2,1%	Cu-poor
#9* (ZnS)	1,76	0,91	2,5%	Cu-poor
#10* (ZnS)	1,78	0,92	3,2%	Cu-poor

Table 4.6: Sample set with similar composition that is examined to analyse the influence of sulphur in the precursor on efficiency. ZnS samples show better efficiencies.

4.3.1.2 Correlation between morphology and efficiency

It is of interest to study if a correlation between the appearance of a film and its performance can be seen. From this one could deduce which parameters – like grain size or compactness of the film – should be subjected to more effort to enhance them in future experiments.

However, we cannot see any correlation between material quality and efficiency. First we consider grain size. One would suspect that larger grains and the hence resulting fewer grain boundaries lead to a larger mean free path of the electrons and reduce recombination. Less recombination should result in higher current and higher efficiency. Looking at Fig. 4.22 one can see two samples with comparable, large grain sizes. The larger grains are roughly between 0,7 to 1 µm. However, the efficiency is significantly different: the sample in Fig. 4.22 a) has 0,5%, while the sample in b) shows 2,3% efficiency.

For small grains the result is the same, even if we do not show such an explicit comparison here. Fig. 4.24 can serve as an example since those samples have both small grains but very different efficiencies.

We conclude that grain size in our experiments has obviously no influence on the efficiency.

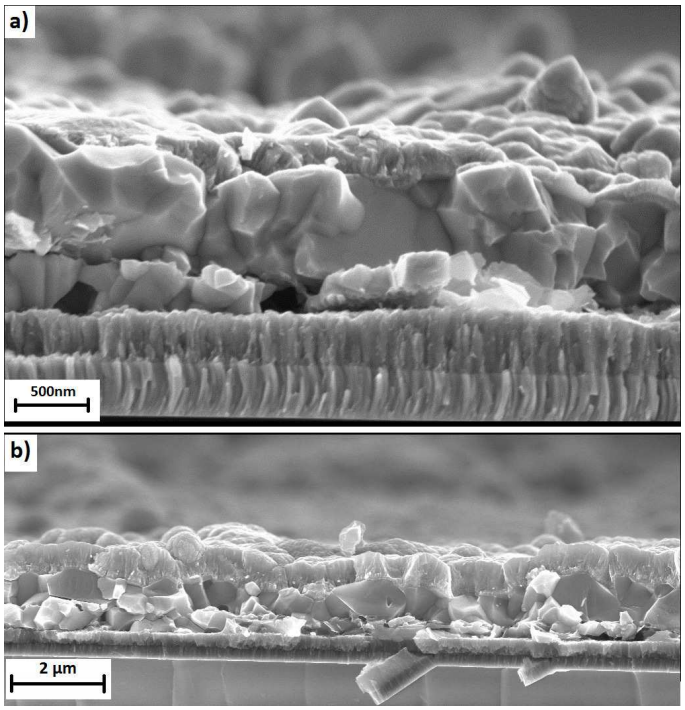

Figure 4.22: Illustration of the correlation between morphology and efficiency. Both samples have large grains, but while the sample in a) (#16) has 0,5% efficiency the cell in b) shows 2,3% (cell #22).

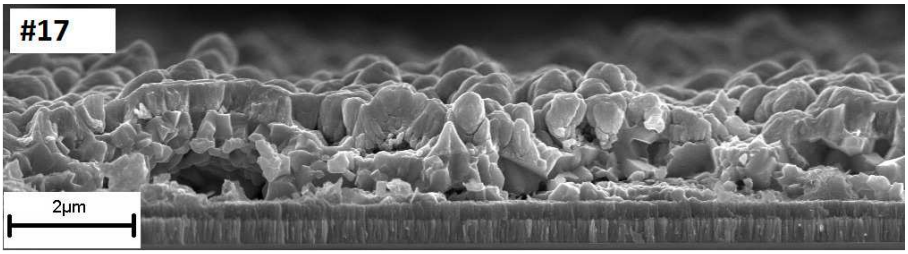

Figure 4.23: Cross section of sample #17. Huge holes can be seen, nevertheless 2,1% could be reached with this cell.

Next, we consider voids and compactness. Fig. 4.23 shows a sample with considerable voids and a very uneven film with 2,1% efficiency. This sample might be compared to Fig. 4.22 b), where a film can be seen with less voids and a smoother surface, but roughly the same efficiency (2,3%).

For small grained films the picture is the same: Compactness or number of voids seem to have no impact on the efficiency. Fig. 4.24 shows two samples, both small grained and very compact. The upper one has an efficiency of 0%, while the lower one shows in spite of the sublayer 3,2%.

Considering the sublayer it was found (chapter 4.2.3.2) that this is most probably a segregated SnS_2 phase. As mentioned in the theory part (chapter 2.3.3) this phase is an n-type semiconductor which would be detrimental for the p-type solar cell. However, the solar cell with the best efficiency of 3,2% was a cell with a SnS_2 sublayer.

We conclude that voids, compactness and even clear layering did not have an influence on the performance of our solar cells either.

Summarizing one can say that morphology and efficiency were independent from each other in our experiments. It was not possible to judge from the visual appearance if a solar cell might show good or bad performance.

The reason for this is quite unclear. One would suggest that films with large grains or compact CZTS would lead to better conditions for the electrons (diffusion length) and in doing so increase the efficiency. That we do not see this correlation might relate to several aspects. First, the level of our efficiencies and other data gained from QE and IV measurements (I_{sc}, V_{oc}, FF) is rather low (see the following chapters 4.3.2, 4.3.3). That means that a lot of parameters probably influence and decrease the performance of our cells. Shunting or isolating phases might be present, the CZTS might be lifted from the substrate at some places, or the top layers (CdS + ZnO) might not be perfect everywhere (pictures with few or not ZnO at all could be seen). Second, we can not be sure that all these parameters that have influence on the efficiency (secondary phases, ZnO, voids, layering, bad adhesion etc.) could be seen on the images for every sample. We divided every sample in different cells and measured efficiency separately. Not always did the several cells on one sample show the same result, but often the efficiencies varied a lot.

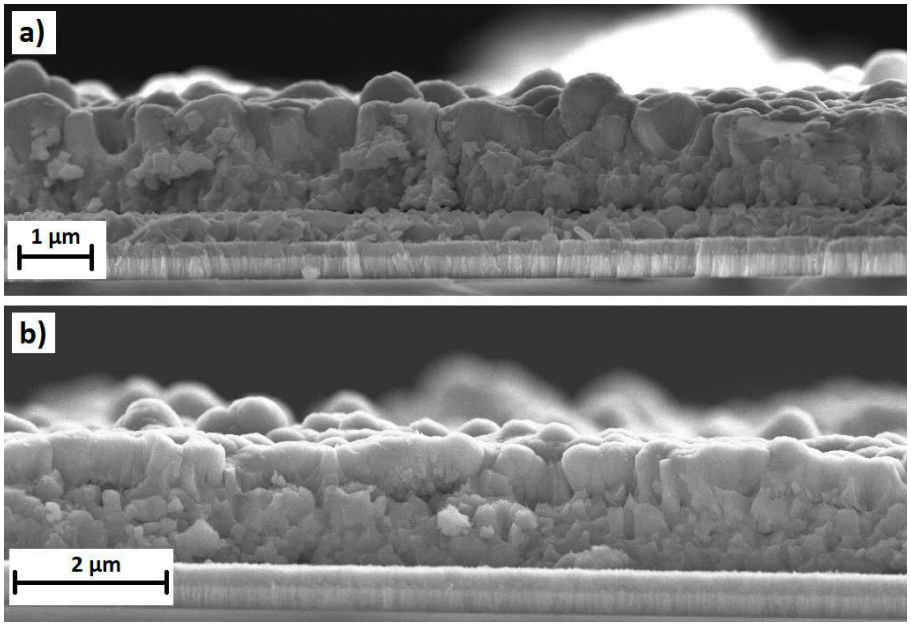

Figure 4.24: Two samples with comparable compactness. a) #14, efficiency 0%. b) #10 with 3,2% efficiency.

On the other hand we looked at only one cross section, and in doing so perhaps saw only bad film quality while the efficiency measurement was performed at another, better region of the sample. Unfortunately it was technically not possible to measure efficiency and cross section at exactly the same place. For this reason we have to trust that we got an overview about the general morphology of each sample, even if we made only one cross section. It is very possible that influences that cannot be seen with an electron microscope (like secondary phases) decrease the performance of a cell a lot, even if the appearance shows nice grains or compact films.

4.3.1.3 Result from the efficiency measurement

We examined the influence of morphology, sulphur in the precursor and the composition of the sulphurized film in terms of efficiency. It could be shown that only composition has a clear impact on the performance of a cell. Here we found that the efficiency increased going from the Zn-poor to the Zn-rich region on a pseudo binary tie line with almost constant Cu/Sn ratio. The best cell efficiencies were gained for the Zn-rich and Cu-poor region. For a general beneficial effect of sulphur in the precursors only a weak trend was noticeable. For parameters like grain size, voids and layering no correlation to the efficiency could be found at all.

4.3.2 QE measurements

Quantum efficiency measurements are a useful tool to get informations about the losses in a cell. For more details about QE measurements see chapter 3.2.5.

Fig. 4.25 shows the QE data for all samples with reasonable results, i.e. where the typical pattern is observable. 'Typical pattern' means for example the kink in the graph starting below $\approx 520\,\text{nm}$. This is the "CdS-kink", resulting from the CdS band gap at 2,42 eV [53] where the CdS layer starts absorbing photons and is not completely transparent any longer. Electrons produced in the CdS are assumed to be lost. The ZnO absorbs most at $> 900\,\text{nm}$ (not relevant here), where free carrier absorption comes into play, and below 400 nm at the band gap for ZnO [53]. For longer wavelengths the band gap of CZTS is limiting. As shown in chapter 4.3.2.2 this starts around 750–800 nm for our cells. Furthermore, recombination at the back contact concerns mainly electrons produced by long wavelengths. Next to these losses, reflection of the layers (CZTS/CdS/ZnO) lowers the whole level.

The latter loss should only reduce quantum efficiency by some percentage, the other losses are supposed to influence the QE only above or below certain wavelengths (those named before). However, what we see is that the overall level of our quantum efficiency is very low and reaches in the best case a bit more than 60%. In most cases half of the incoming energy or even more is not converted into usable current. That means that fundamental losses reduce the whole level. These losses could be

1. *Shunting*: Metallic secondary phases or pinholes bypass the space charge region and the separated electron-hole-pairs recombine directly.
2. *Reduced active area*: The actual area that contributes to the current might be reduced by several influences:
   - Isolating secondary phases reduce the area as they do not produce electron-hole-pairs and hinder the electrons to come to the front contact.
   - The same is valid for voids.
   - Parts of the film can due to bad adhesion flake off. Even if not the hole film falls off, if it happens after deposition of CdS and ZnO those layers fall off as well (seen in some pictures) and the current cannot be transported away.
3. *Layering*: Parts of our samples showed that the absorber was divided into layers. Besides the fact that the sublayer turned out to be a secondary phase (SnS_2) at least in some cases, a crack within the absorber will definitely impair electron migration.
4. *Interface recombination*: Recombination at the interfaces, i.e. between CZTS and CdS, CdS and ZnO as well as surface recombination, concern all electrons and therefore lower the whole current level.
5. *Recombination at defects*: Secondary phases, holes, unwanted impurities etc..
6. *Voids*: Voids, like for example in Fig. 4.14, can reduce the active area of the cell.

The differences regarding the level between the different curves in Fig. 4.25 can in the main be explained by the different efficiencies. The red curves have an efficiency better than 2%, the blue ones between 1,2% and 2%, and the lowest of 0,4% (black). As shown in chapter 4.3.1 this has for our samples mainly to do with the composition, which probably effects secondary phases, even if we cannot point out here if certain phases are correlated to certain quantum efficiencies or losses of QE.

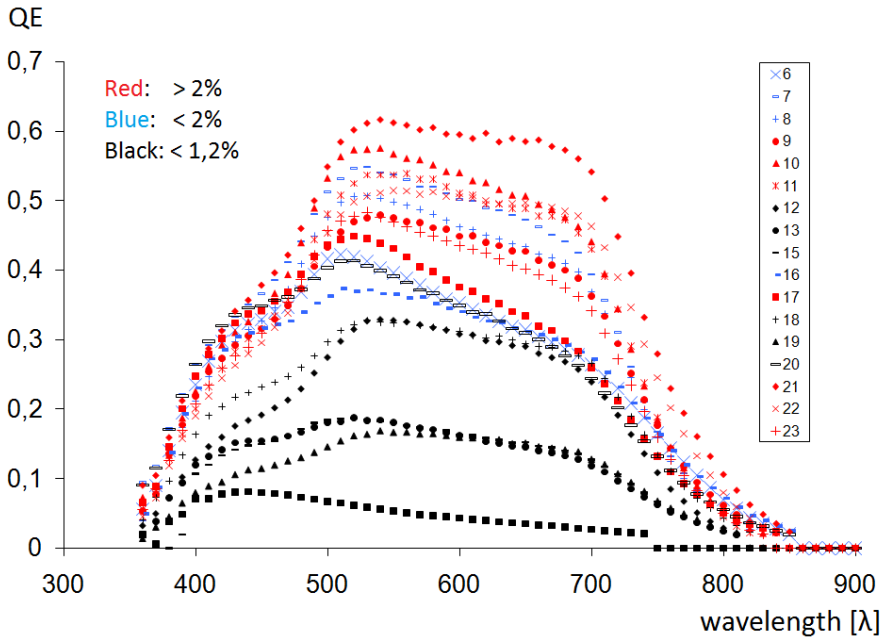

Figure 4.25: QE curves of all samples with reasonable curves, sorted by efficiency.

There is one distinctive difference between the curves, though, that does not concern the overall level but only the long wave lengths. Looking at sample #21 and #22 (Fig. 4.26) one can see that these curves show some kind of plateau, which means that they in contrast to the other curves do not slope after reaching the maximum value. Even if two samples are the minority one could assume that they represent the optimum case. The slope after the maximum QE value means an increasing loss for higher photon wavelengths. This effect was also observed in literature (see for example [54]). A first idea would be that the films are too thin and low energy photons just pass the solar cell without being absorbed. However, these two samples are not particularly thick compared to the other cells. Too thin films could thus only mean a general lowering of the QE level for higher wavelengths for all samples. Indeed there are some more reasons that could cause this effect which we want to discuss in the following.

4.3.2.1 Possible reasons for slopes in the QE curves

In order not to complicate the discussion we want to consider samples very near in composition as we already know that composition influences both efficiency and the presence of secondary phases strongly. Next to the two samples with a plateau, there is one more sample made of the same precursor, and the three samples are very near in composition after sulphurization as well (see Table 4.1). For the sake of clarity the three graphs are plotted again without all the others in Fig. 4.26, which makes the difference even clearer. The samples #21 and #22 show a plateau that #23 does not have. Three possible explanations will be discussed below.

1. A small space charge region

   As discussed in the theory part (chapter 2.1.7) is a large space charge region (SCR) beneficial for a solar cell as more electron-hole-pairs are excited within it and directly feel the electrical field. All other electrons have to reach the SCR by diffusion; therefore a smaller SCR results in fewer electrons reaching it. The recombination probability increases with increasing distance to the SRC, i.e. for electrons produced deeper in the absorber. Those electrons are generated by long wave length photons, which is the correlation of interest here.

   As described in the theory part of this work (chapter 2.1.4) the extension of the SCR depends on the doping: Less doping of the absorber leads to a larger SCR. For our material the doping is intrinsic, that means no material is added for doping but this happens by intrinsic defects. The doping is thus influenced by the composition, which for our three samples is very similar. Even for a look on all samples and their composition no trend to a correlation between composition and absorption of long wave photons can be seen. This means that we cannot proof this theory.

2. A bad back contact

   Like all interfaces the back contact is a region of increased recombination. Electrons produced deep in the absorber, i.e. nearer to the back contact, have of course a higher probability to reach this interface by diffusion. If we would find some observable difference for the back contacts (we have only the tool "cross section") this might be an explanation for the different QE pattern of the three cells.

   Considering the film, especially sample #21 and #23 are quite similar; both show some kind of layering near the back contact (Fig. 4.27). This makes obviously not the difference. However, looking at the other side of the back contact, the Mo or rather the MoS_2 (see chapter 4.2.3.2), a difference between the samples with plateau for the QE curve and the sample that has a slope can be seen. The MoS_2 is much thinner for the latter, which might indicate some influence of this layer on the back contact. For CIGS it is shown that a very thin $MoSe_2$ layer at the back contact is a so called back surface field. This can be seen as an electronic mirror where electrons are reflected (by a potential wall) and so the back contact recombination is

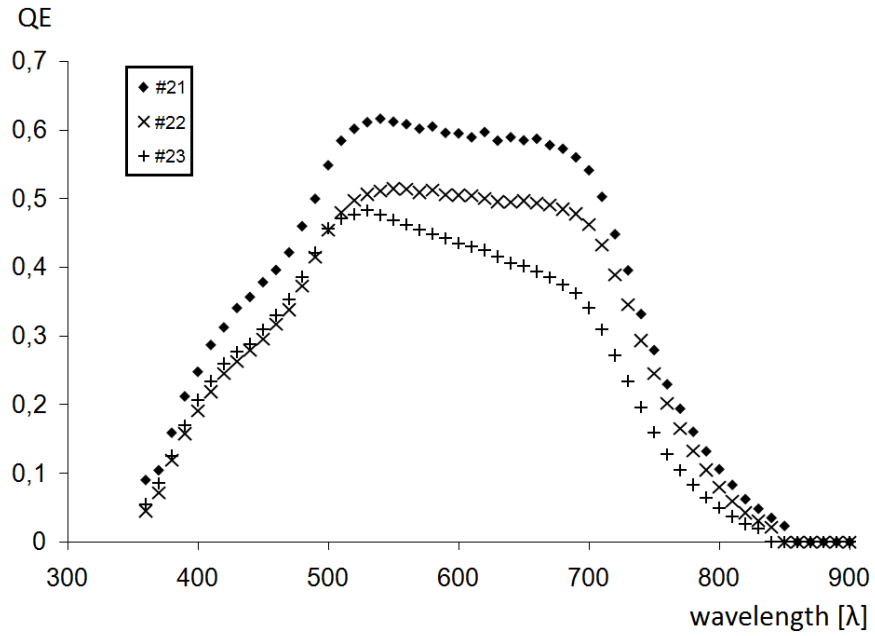

Figure 4.26: 3 samples with similar composition (made of the same precursor). The curves of sample #21 and #23 show a plateau, while the curve for #22 slopes after reaching the maximum QE value.

reduced [55]. In the same way the MoS_2 might have some beneficial influence for our back contacts. This is admittedly a very unconfident theory. No such an effect was reported for CZTS so far and the band structure for CZTS (here needed for the back contact) is not known either. Furthermore, samples #21 and #22 are the only ones with a plateau in QE but not the only ones with thick MoS_2. Therefore we conclude that an influence of MoS_2 on the back contact and the recombination at the same place is not impossible, but we cannot prove it.

3. A low diffusion length

   To contribute to a current, the electrons produced deep in the absorber need to reach the SCR by diffusion before they recombine. The diffusion length of the electrons depends on the material quality, i.e. grain size, compactness, as well as on voids and other crystal defects that enhance recombination of the electrons. To see if such aspects might be responsible for this QE results we take a look at Fig. 4.27. a) and b) show the samples that have a plateau in the QE curve (#21 and #22). Both samples have at the same time comparatively large grains in the µm range. Fig. 4.27 c) shows sample #23 which has similar composition but a slope in QE measurements for higher wavelengths, and the grains are significantly smaller (<0,5µm).

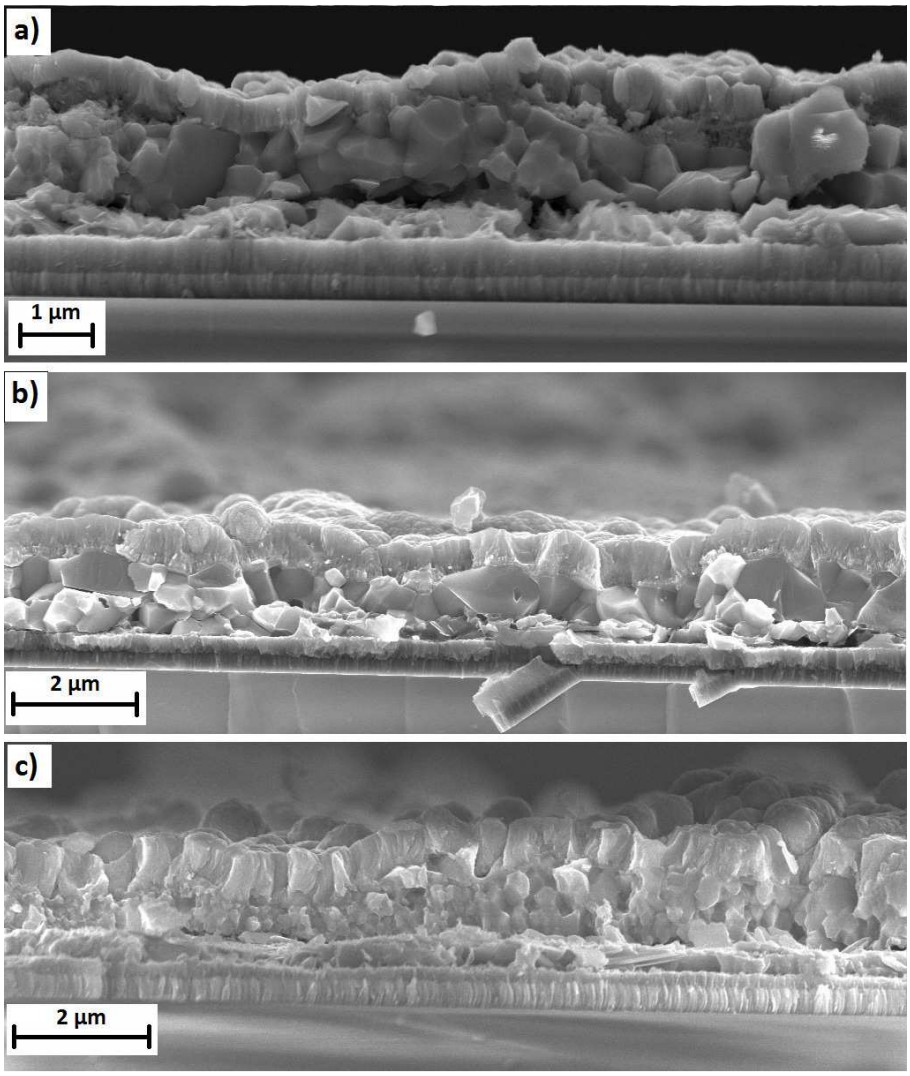

Figure 4.27: Cross sections of the three samples #21 a), #22 b) and #23 c) that were analysed regarding the QE curve. While the samples with the plateau in the QE curve have large grains (#21 and #22) sample #23 has considerably smaller grains, which might be the reason for the worse quantum efficiency for higher wavelengths.

This means that the grain size could be a possible explanation for the differences of the QE curves for these three samples. As grain boundaries are (like other crystal defects) a region of potentially increased recombination, this looks like a plausible explanation. However, samples with large grains and a slope in QE exist as well, even if they are due to their different composition not comparable with these three samples. Hence, we conclude that the presence of large grains could be a necessary but not sufficient condition for the collection of electrons produced by long wave photons.[1] It is noticeable that at the same time efficiency was not influenced by this aspect: The samples with plateau in QE and large grains have 2,6% and 2,3% efficiency, respectively, while the sample with the slope shows 2,7%.

4.3.2.2 The bandgap

A common way to estimate the band gap E_g is to extract it from the squared quantum efficiency, like described in chapter 3.2.5. For it the x-scale is converted from wavelength to energy and the QE-values are squared. The slope at the long wave length side (corresponds to the low energy side) of the curve is extrapolated to 0, like shown in Fig. 4.28. As this includes of course some freedom where exactly to draw the extrapolation line, we show the extrapolations of the examined QE^2-curve for sample #22. We consider this more as estimation for the band gap than an exact definition since the edge in general is not sharp.

Fig. 4.28 shows also three more curves, even if only the detail of the extrapolation. The samples are #21–23 which were examined in the last chapter (4.3.2.1) and additionally a sample with a much lower QE level (sample #15, dark blue in Fig. 4.28). The band gaps for our CZTS lie between 1,5 and 1,65 eV (corresponding to $\approx$ 750–800 nm). This is slightly higher than what is reported in publications (1,45–1,5 eV, [20], [56]).

4.3.2.3 Summary

The QE measurements revealed that fundamental losses reduce the quantum efficiencies of our cells. Possible reasons are conducting and isolating secondary phases, voids, bad adhesion between the layers as well as layering. We assume that all these aspects contribute in varying proportions to the low QE level, as they all have been proven by our analyses. For the fact that most curves slope after reaching the maximum QE value we suggest after comparing near-compositional samples that grain size could be one responsible parameter. Larger grains might increase the probability for the collection of more electrons that were produced by long wavelength photons. An influence of space charge region and back contact could not be proven.

1 Morphological aspects that could be responsible for a lower diffusion length (like voids, layering, compactness etc.) but did not turn out to be different for the "plateau-samples" and the "slope-sample" on the cross sections are not discussed here. Grain size was the only clear difference.

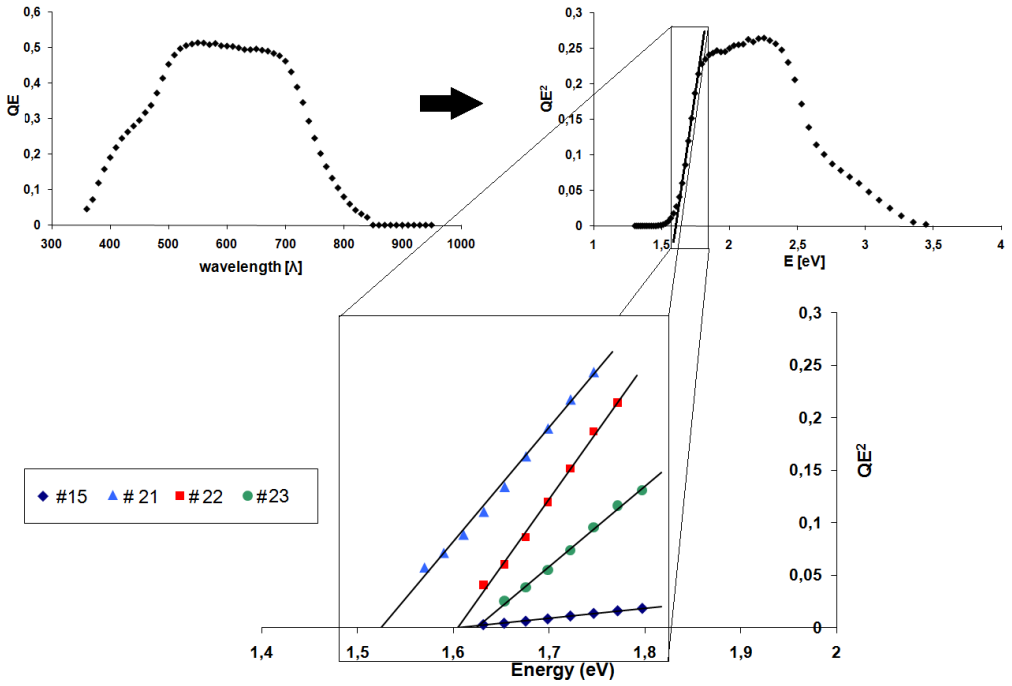

Figure 4.28: Possibility to extract the band gap from the QE curve. The band gap is the interception of the interpolated slope of the squared QE-curve.

From squared QE-curves we extracted a rough estimation for the band gap. It is for our samples between 1,5 and 1,65 eV.

4.3.3 IV measurements

For further analysis we performed *IV measurements*. During IV measurements the cell is illuminated and the current is measured while at the same time the voltage is varied. The result is (for good cells) a diode curve like discussed in chapter 2.1.7.

For this discussion we want to concentrate on the clearest cases to point out possible influences on the IV behaviour of the cells. The other cells lie somewhere in between and are thus subjects to several influences.

Fig. 4.29 a) shows the three solar cells with the best parameters we got. Sample #10 had the highest efficiency (3,2%) and open current voltage (0,72 V), #21 showed the highest short circuit current density ($I_{sc} = 12{,}6\ \frac{mA}{cm^2}$), and sample #17 had the best fill factor of all our cells (FF = 47,9%).

The blue line in Fig. 4.29 a) represents sample #10. It has the highest η and V_{oc} of all our solar cells. Even the current is with $I_{sc} = 10{,}9\ \frac{mA}{cm^2}$ in the range of the best values we got. The voltage is not the maximum one would expect from theoretical foundations but

exceeds the so far best published results by ca. 10%.[1] The efficiency is clearly lower than the so far world record of 6,8% (IBM, [7]). The high slope at forward bias suggests that the cell has a high series resistance. First, the curve is not exponential for high voltages like for an ideal diode but a linear slope ($I = \frac{U}{R_S}$). Second, the curve is not almost "rectangular shaped" like an ideal diode curve, but the current is very voltage-dependent. That means, as soon as current is flowing, a part of the voltage drops due to the series resistance.

The same is valid even to a greater extend for sample #21 (red curve). It has the highest I_{sc} found for our cells. It drops even more even for quite low voltages. Furthermore, increasing the voltage in the reverse direction of the diode results in increased current. A possible reason for this shunting, which means we would also have a parallel resistance R_{SH}. A high parallel conductance could even be responsible for the lower V_{oc} compared to the maximum value we found (for more details see chapter 2.1.9). Furthermore, voltage dependent carrier collection (see chapter 2.1.6) can cause this phenomenon.

The maximum current for our solar cells is significantly lower than one could expect from theory (see chapter 2.1.7) and what other groups received (22–24 $\frac{mA}{cm^2}$ and 15–20 $\frac{mA}{cm^2}$, respectively; [37], [7]). This problem is related to what was said about the QE measurements (4.3.2): General losses caused by secondary phases, interface recombination and such effects mentioned before reduce the overall electron collection and in doing so reduce the current compared to what would be possible in a perfect cell.

The most significant loss we got was in the fill factor (FF). As defined in the theory part (equation 2.7) it is $FF = \frac{I_{mp} \cdot V_{mp}}{I_{sc} \cdot V_{oc}}$. That means even compared to our open circuit voltage V_{oc} and the comparably low I_{sc} we gain very low power. Best solar cells made of CZTS reached above 60% ([37], [7]), our maximum value was $\approx 48\%$. This is seen for sample #17 (green line in Fig. 4.29 a)). It shows the most "rectangular" shape of the curve; the linear behaviour of the curve for high voltages indicates again series resistances.

However, several samples were far away from reaching that; while the average fill factor for all of our cells is 33,3%, some samples have a FF of only 25%. This is the fill factor of a linear slope (conductor), and three examples of this kind can be seen in Fig. 4.29 b). The reason is most probably that the cells are completely shunted. A voltage dependent

1 The maximum voltage that is theoretically possible is difficult to estimate. Not the whole band gap can be gained as V_{oc} but only the band gap minus the distance of the doping levels from the conduction and valence band, respectively (see chapter 2.1.7). Futher reduction is due to radiative losses at room temperature. For example for CIGS, a material close related to CZTS, there is an empirical formula $V_{oc} = \frac{E_g}{q} - 500\,mV$ ([57]). This would suggest a value of around 1 V for a band gap of 1,5 eV. Publications on CZTS gave up to around 0,65 V in open current voltage (640 mV (IBM,[47]), 662 mV (Katagiri, [37])). V_{oc} is reduced by recombination throughout the cell and future improvements of CZTS devices are expected to give at least some improvements in V_{oc}. Wide band gap solar cells often show a larger loss in V_{oc} relative to their theoretical maxima than for smaller band gap materials. The reason for this is not completely clear. For CZTS it is assumed that very short life times and interface recombination might be responsible. For example is always CdS used a a buffer layer like for CIGS; however, it is unknown if other buffer layers might suit better to CZTS. So far it is unclear to what extent fundamental material properties of CZTS will limit V_{oc} in the future.

carrier collection can most likely be excluded as the dark curve of the samples looks the same, which should then not be the case (but look like a normal diode).

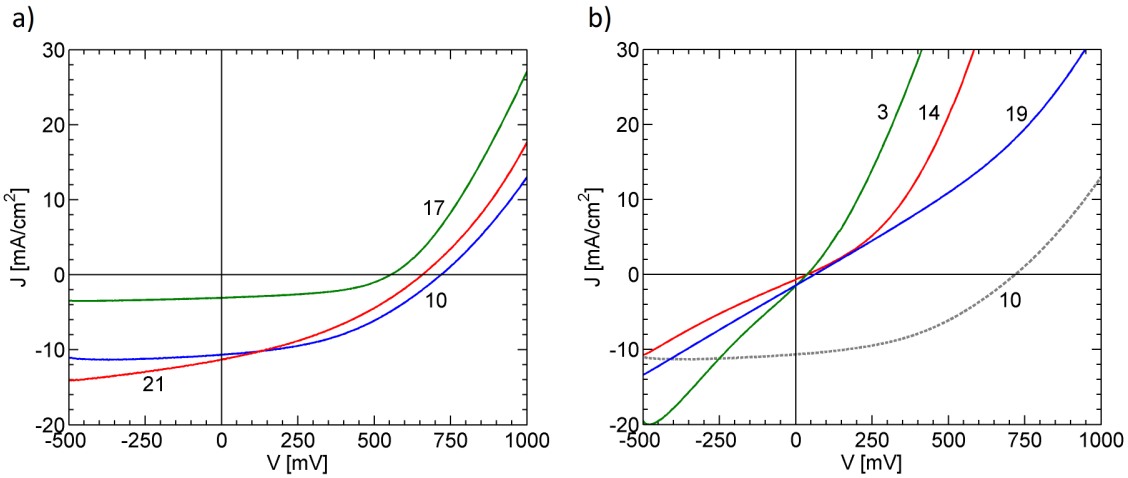

Figure 4.29: a) Samples with the best IV data measured in our experiments. #10 has the best efficiency and the best V_{oc}, #17 the best fill factor and #21 the best value for I_{sc}. b) Samples #3, #14 and #19 with bad fill factor and efficiency. They were most likely shunted. For comparison sample #10 that showed the best efficiency in our experiments is added in grey.

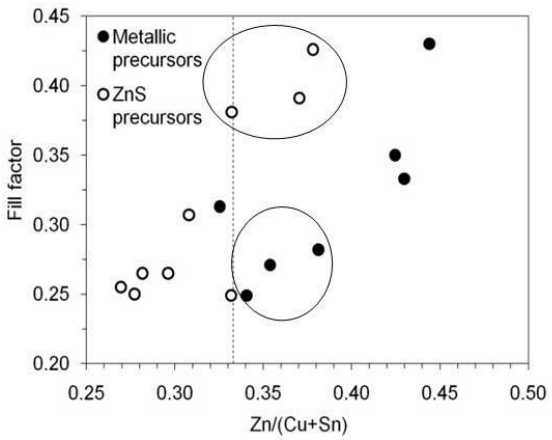

Figure 4.30: FF plotted against Zn content. For ZnS samples generally higher FFs are achieved than for metallic samples with the same Zn content. The circled samples are discussed in the text. They have excess Zn, as the vertical dotted line that shows stoichiometry indicates.

Two of the curves in Fig. 4.29 b) are by the way of stoichiometric samples which again indicates that we could have secondary phases for films with stoichiometric composition as well. However, shunting can also be caused by pinholes.

Considering the fill factor an interesting observation could be made concerning the difference between metallic and ZnS films. Looking at Fig. 4.30 where the fill factor is plotted against the Zn/(Cu+Sn) ratio (i.e. the Zn content, compare to Fig. 4.20), one sees not only the trend of improvement with increasing Zn content. Furthermore, for the fill factor obviously the ZnS had a major impact. There is a clear trend that samples for a certain Zn/(Cu+Sn) ratio became better for the films with sulphur in the precursor.

A closer look at the cross sections of the 3 metallic and ZnS samples, respectively, which are similar in Zn-content but very different in the FF (see marked samples in Fig. 4.30), reveals that the morphology is actually quite different. While the ZnS samples show only some voids within the CZTS, do the metallic ones have quite poor morphology. They have large voids or even cracks, in particular between CZTS and Mo. Pinholes or cracks through the whole CZTS film could shunt the cell and by this decrease FF. Furthermore the metallic films may have a different segregation of secondary phases, and isolating secondary phases like ZnS might increase the series resistance for the solar cells and in this way reduce FF. As the samples have Zn excess, ZnS would be expected from the TPD.

This observation suggests that the film growth for similar composition obviously is enhanced by the use of ZnS in the precursor instead of Zn (metallic precursor). Possibly due to less diffusion in the ZnS samples, fewer voids are formed by migrating elements. That supports the observation in chapter 4.3.1.1 that the integration of S in the precursor leads to smoother films with less voids.

However, such a general trend that ZnS samples are better could be seen neither for I_{sc} nor for V_{oc}.

Summary

The IV-measurements showed the maximum values $\eta = 3{,}2\%$, $FF = 48\%$, $I_{sc} = 12{,}6\ \frac{mA}{cm^2}$ and $V_{oc} = 0{,}72\,V$. While the open circuit voltage is higher than reported in other publications are efficiency, fill factor and short circuit current lower than for published record cells. The low current indicates general losses for electron collection; the fill factor is reduced by parallel and series resistances in our cells. The efficiency is affected by these losses (i.e. lower than it would be possible for this material). The results show that we probably have secondary phases that cause loss of active area (affects I_{sc}), increase the series resistance (FF) and can shunt the cell (FF). Pinholes, voids and other defects could be further reasons for the described effects. For this experimental series it was not possible to correlate the observed phenomena to certain defects, in can only be stated that – like for the efficiency part – the best IV results where found for Cu-poor and Zn-rich samples; stoichiometric and Zn-poor samples showed a bad IV performance. For the fill factor we observed a beneficial effect of sulphur in the precursor and assume that this is due to a smoother sulphurization process with less diffusion resulting in less voids and more compact films.

4.3.4 Conclusions

The best solar cell fabricated in our experimental series had 3,2% efficiency. Further maximum values for solar cell parameters are a fill factor of roughly 48%, and open circuit voltage of 0,72 V and a short circuit current of 12,6 $\frac{mA}{cm^2}$. For the band gap we estimate that our CZTS lies between 1,5 and 1,65 eV.

However, the potential for this material is much higher than what we could measure for our samples. QE and IV measurements revealed that we have significant losses. Low QE level and I_{sc} indicate general losses in charge carrier generation and collection. Secondary phases, voids, layering and bad adhesion can by increasing series resistance and recombination as well as by shunting be responsible for this and have been found to be present in our samples in a previous chapter. Clear correlations between certain losses and defects were difficult to find. However, the main influence on efficiency turned out to be the composition of the absorber (best results for Cu-poor and Zn-rich films), and large grains might be one factor that is beneficial for the collection of electrons produced by long wave photons. The former is related to the fact that samples from the Cu-poor or Zn-rich region would according to the phase diagram mainly have ZnS as secondary phase, which is the least bad secondary phase for CZTS solar cells, while samples in the Zn-poor region (where most of our bad films were) can show copper sulfides or CTS which are conductive and can shunt the sample. A trend that could be seen in our experiments (but should be examined for more samples in different regions of the phase diagram) is the beneficial effect of more Zn; on a pseudo binary tie line from the Zn-poor to the Zn-rich region increased efficiency with the Zn content.

Another observation is that ZnS obviously has a clear beneficial effect concerning the fill factor. While the FF increases with increasing Zn-content (just like the efficiency), almost all ZnS samples show a higher fill factor than metallic ones for the same Zn/(Cu+Sn) ratio. We refer this effect to a better film quality seen for these samples, that might result from a smoother sulphurization process, which could be enhanced by less diffusion as a consequence of S already in the precursor.

For a general beneficial influence of ZnS in the precursor next to the fill factor, however, only a weak trend could be observed.

5 Conclusions and suggestions for future work

The purpose of the presented work was to fabricate and analyse the thin film material Cu_2ZnSnS_4 (CZTS) and to produce solar cells based on this material. In the following the most important results are summarized.

We used a two-step process to produce CZTS. The first step comprised the co-sputtering of metals (metallic precursors) and metals + sulphur (ZnS precursors), respectively. Analysis of the precursors showed that they were all Cu-poor and Sn-rich compared to stoichiometry (Cu/Sn in average 1,7 where 2 would be stoichiometric). The composition was uniform within the precursors, only the surfaces showed some gradients. For metallic precursors, crystalline phases were found, even though it was not possible to assign all XRD peaks to certain phases. The ZnS precursors were amorphous as seen by XRD.

As all precursors were fabricated on different substrates (glass, glass coated with molybdenum and silicon) we studied the influence of the substrate as well. No difference in composition or compositional gradients could be found here.

The second process step was sulphurization of the precursors. Excess of sulphur was provided, however all samples showed almost exactly 50% of sulphur content, which is stoichiometric. That made it possible to examine the samples using the ternary phase diagram of Cu, Zn and Sn. The main observation here was that all samples showed some Sn-loss. This was more distinct for the metal precursors, and the conclusion was that metal films tend to loose Sn by evaporation of SnS_2, while this secondary phase is partly enclosed for ZnS films. An explanation for different forming of CZTS for the two different precursors types was suggested.

Good reproducibility of the sulphurization process considering composition and efficiency was shown.

Further analysis concerned the influence of the composition on the films. A correlation between composition and morphology was not found, except that the formation of several layers might be avoided by stoichiometric composition. Moreover, all films showed additional peaks next to the CZTS (Σ) pattern, indicating that all films contained secondary phases to some extent. Most could not be identified, but for some samples from the Sn-rich region a Sn-rich sublayer - most likely SnS_2 - was found. As those samples were made of ZnS precursors this supports the theory about the enclosure of tin sulfides in those films. EDS measurement showed copper- and tin-sulphide conglomerates on the surface.

Even if an influence of composition on morphology could not be proven, the influence on efficiency was strong. Here we found that more Zn is to a certain extent beneficial for the performance of the solar cell. The best results were found for Cu-poor and Sn- as well as Zn-rich films. We attribute this to the fact that Zn-poor samples (which showed the

worst performance) probably lead to formation of the most detrimental secondary phases. Cu- and Cu-Sn-sulfides are conducting and can cause shunting, while ZnS (expected for Zn-rich films) is insulating and thus mainly reduces the active area of the solar cell.

Another important point we studied was the influence of S in the precursor. A weak trend could be observed that those precursors developed to more compact films with smaller grains and slightly higher efficiencies. Concerning the fill factor this trend was a bit clearer.

The best solar cell parameters that were measured for our cells had 3,2% efficiency, a fill factor of roughly 48%, an open circuit voltage of 0,72 V and a short circuit current of 12,6 $\frac{mA}{cm^2}$. We estimate that the band gap of our CZTS lies between 1,5 and 1,65 eV. Those values are comparable to previously published data. Nevertheless, we assume that the potential of our CZTS is even higher, as QE and IV measurements suggest high losses for the generation and collection of the charge carriers. Increasing grain size and most of all reducing secondary phases, pinholes and voids might decrease series and parallel resistance as well as other losses and lead to higher efficiencies. However, it is not clear if that is possible with this simple sulphurization process.

The importance of composition on the performance of the solar cells shall be emphasized as the main conclusions from this work. This study systematically compared CZTS films from almost all different regions of the phase diagram (Zn-rich, Cu-poor, Sn-rich, Zn-poor, Sn-poor and stoichiometric). The result is that Zn-deficiency produces poor solar cells and the composition should rather be Zn-rich, Cu-poor or Sn-rich.

Recommendations for future work

The sulphurization process used in this work was very simple and for example concerning sulphur content and pressure not controllable. Due to the simple furnace used we could sulphurize only very tiny samples which complicated the analyses in several cases. Therefore we would recommend using a furnace that allows control of more parameters and the use of larger samples, which might directly solve some of our problems and would also allow studying variations in the sulphurization process, which is probably a very important parameter.

Besides this practical aspect, further experiments concerning results that were somewhat unclear in this study could be performed. The increase of efficiency with the Zn-content could only be shown for one fixedCu/Sn ratio and it would be interesting to extend this study for more compositions. Perhaps even the missing region of the phase diagram could be examined concerning the correlation between composition and efficiency, even if we strongly assume that Cu-rich samples will perform badly due to the secondary phase Cu_2S, which has to be expected according to the phase diagram.

Finally, the reported beneficial influence of sulphur in the precursor was weak in our experiments. Comparison of more metallic and ZnS precursors near or even equal in composition could enlighten this question.

Bibliography

[1] Solomon, S. ; Qin, D. ; Manning, M. ; Chen, Z. ; Marquis, M. ; Averyt, K.B. ; M.Tignor ; Miller, H.L.: *Zusammenfassung für politische Entscheidungsträger. In: Klimaänderung 2007: Wissenschaftliche Grundlagen.* http://www.ipcc.ch/pdf/reports-nonUN-translations/deutch/IPCC2007-WG1.pdf. Version: 2007

[2] Bundesanstalt für Geowissenschaften und Rohstoffe: *Reserven, Ressourcen und Verfügbarkeit von Energierohstoffen.* http://www.bgr.bund.de/cln_109/nn_322848/DE/Themen/Energie/Downloads/Energiestudie-Kurzf-2009,templateId=raw,property=publicationFile.pdf/Energiestudie-Kurzf-2009.pdf. Version: 2009

[3] IAEA: *The Long Term Storage of Radioactive Waste: Safety and Sustainability.* http://www-pub.iaea.org/MTCD/publications/PDF/LTS-RW_web.pdf. Version: 2003

[4] Bundesministerium für Umwelt, Naturschutz und Reaktorsicherheit: *Erneuerbare Energien.* http://www.dlr.de/tt/Portaldata/41/Resources/dokumente/institut/system/publications/broschuere_ee_innov_zukunft.pdf. Version: 2004

[5] Green, M. A. ; Emery, K. ; Hishikawa, Y. ; Warta, W.: Solar cell efficiency tables (version 35). In: *Progress in photovoltaics: Research and applications* 18 (2010), S. 144–150

[6] Umweltbundesamt: *Seltene Metalle.* http://www.umweltdaten.de/publikationen/fpdf-l/3182.pdf. Version: 2007

[7] Wang, K. ; Gunawan, O. ; Todorov, T. ; Shin, B. ; Chey, S. J. ; Bojarczuk, N.A. ; Mitzi, D. ; Guha, S.: Thermally evaporated Cu_2ZnSnS_4 solar cells. In: *Applied Physics Letters* 97 (2010)

[8] Neuberger, F.: *Module power evaluation report.* http://www.schottsolar.com/global/solar-yield/long-term-study/. Version: 2009

[9] ISI: *Rohstoffe für Zukunftstechnologien.* http://www.isi.fraunhofer.de/isi-de/n/projekte/rohstoffbedarf.php?WSESSIONID=edc588012d961c68488601f69504ffa0. Version: 2009

[10] Poortmans, J. (Hrsg.) ; Arkhipov, V. (Hrsg.): *Thin Film Solar Cells.* Wiley, 2006

[11] Würfel, P. ; Würfel, U.: *Physics of Solar Cells*. Bd. 2. Wiley-VCH, 2009

[12] http://rredc.nrel.gov/solar/spectra/

[13] Ibach, H. ; Lüth, H.: *Festkörperphysik*. Bd. 6. Springer, 2002

[14] Green, Martin A.: *Solar cells*. The University of New South Wales, 1998

[15] Hahn, G. ; Willeke, G.: *Halbleitertechnologie und Physik der Solarzelle*. Printout. http://www.uni-konstanz.de/pv/index_l.htm. Version: 2008-2009

[16] Schleußner, S.: *Cu(In,Ga)Se_2 Thin Film Solar Cells with ZrN as a Back Contact*, Universität Stuttgart, Diplomarbeit, 2003

[17] Zimmermann, U.: *Solar Cell technology*. lecture script PhD course, 2007

[18] Lewerenz, H.-J. ; Jungblut, H.: *Photovoltaik - Grundlagen und Anwendungen*. Springer-Verlag, 1995

[19] Bhattacharya, R. N. ; Ramanathan, K.: *Cu(In,Ga)Se_2* thin film solar cells with buffer layer alternative to CdS. In: *Solar Energy* 77 (2004), S. 679–683

[20] Ito, K. ; Nakazawa, T.: Electrical and Optical Properties of Stannite-Type Quaternary Semiconductor Thin Films. In: *Jpn. J. Appl. Phys.* 27 (1988), S. 2094–2097

[21] Maeda, T. ; Nakamura, S. ; Wada, T.: Electronic Structure and Phase Stability of In-free Photovoltaic Semiconductors, $Cu_2ZnSnSe_4$ and Cu_2ZnSnS_4 by First-principles Calculation. In: *Mater. Res. Soc. Symp. Proc.* 1165 (2009)

[22] Hall, S.R. ; Szymanski, J.T. ; Stewart, J.M.: Kesterite, $Cu_2(Zn,Fe)SnS_4$, and stannite, $Cu_2(Fe,Zn)SnS_4$, structurally similar but distinct minerals. In: *Canadian Mineralogist* 16 (1978), S. 131–137

[23] Lide, D. R. (Hrsg.): *Handbook of Chemistry and Physics*. 79th. CRC press, 1998-1999

[24] Bernardini, G. P. ; Borrini, D. ; Caneschi, A. ; Benedetto, F. D. ; Gatteschi, D. ; Ristori, S. ; Romanelli, M.: EPR and SQUID magnetometry study of Cu_2FeSnS_4 (stannite) and Cu_2ZnSnS_4 (kesterite). In: *Physics and Chemistry of Minerals* 27 (2000), S. 453–461

[25] Chen, S. ; Yang, J. ; Gong, X. G. ; Walsh, A. ; Wei, S.: Intrinsic point defects and complexes in the quaternary kesterite semiconductor Cu_2ZnSnS_4. In: *Phys. Rev. B* 81 (2010), Nr. 24, S. 245204

[26] Scragg, J. J.: *Studies of Cu_2ZnSnS_4 films prepared by sulphurisation of electrodeposited precursors*, University of Bath, Diss., 2010

[27] Olekseyuk, I.D. ; Dudchak, I.V. ; Piskach, L.V.: Phase equilibria in the Cu_2S-ZnS-SnS_2 system. In: *Journal of Alloys and Compounds* 368(1-2) (2004), S. 135–143

[28] Weber, A.: *Wachstum von Dünnschichten des Materialsystems Cu-Zn-Sn-S*, Friedrich-Alexander-Universität Erlangen-Nürnberg, Diss., 2009

[29] Schurr, R. ; Hölzing, A. ; Jost, S. ; Hock, R. ; Voß, T. ; Schulze, J. ; Kirbs, A. ; Ennaoui, A. ; Lux-Steiner, M. ; Weber, A. ; Kötschau, I. ; Schock, H.-W.: The crystallisation of Cu_2ZnSnS_4 thin film solar cell absorbers from co-electroplated Cu–Zn–Sn precursors. In: *Thin Solid Films* 517 (2009), S. 2465–2468

[30] Wagner, R. ; Wiemhöfer, H. D.: Hall effect and conductivity in thin films of low temperature chalcocite Cu_2S at 20°C as a function of stoichiometry. In: *Journal of Physics and Chemistry of Solids* 44 (1983), S. 801–805

[31] Nozaki, H. ; Shibata, K. ; Ohhashi, N.: Metallic hole conduction in CuS. In: *Journal of Solid State Chemistry* 91 (1991), S. 306–311

[32] Shibata, T. ; Muranushi, Y. ; Miura, T. ; Kishi, T.: Photoconductive properties of single-crystal 2H-SnS_2. In: *Journal of Physics and Chemistry of Solids* 51 (1990), S. 1297–1300

[33] Wu, C. ; Hu, Z. ; Wang, C. ; Sheng, H. ; Yang, J. ; Xie, Y.: Hexagonal Cu_2SnS_3 with metallic character: Another category of conducting sulfides. In: *Applied Physics Letters* 91 (2007), S. 143104

[34] Yoo, H. ; Kim, J.: Comparative study of Cu_2ZnSnS_4 film growth. In: *Solar Energy Materials and Solar Cells* 95 (2010), S. 239–244

[35] Fernandes, P. A. ; Salomé, P. M. P. ; Cunha, A. F.: Precursors' order effect on the properties of sulfurized Cu_2ZnSnS_4 thin films. In: *Semiconductor Science and Technology* 24 (2009), Nr. 10, S. 105013

[36] Katagiri, H. ; Ishigaki, N. ; Ishida, T.: Characterization of Cu_2ZnSnS_4 thin films prepared by vapor phase sulfurization. In: *2nd world conference on photovoltaic solar energy conversion* Bd. 1, 1998, S. 640–643

[37] Katagiri, H. ; Jimbo, K. ; Yamada, S. ; Kamimura, T. ; Maw, W. S. ; Fukano, T. ; Ito, T. ; Motohiro, T.: Enhanced Conversion Efficiencies of Cu_2ZnSnS_4-Based Thin Film Solar Cells by Using Preferential Etching Technique. In: *Applied Physics Express* 1 (2008), Nr. 4, 041201

[38] Araki, H. ; Mikaduki, A. ; Kubo, Y. ; Sato, T. ; Jimbo, K. ; Maw, W. S. ; Katagiri, H.i ; Yamazaki, M. ; Oishi, K. ; Takeuchi, A.: Preparation of Cu_2ZnSnS_4 thin films by sulfurization of stacked metallic layers. In: *Thin Solid Films* 517 (2008), Nr. 4, S. 1457–1460

[39] Ennaoui, A. ; Lux-Steiner, M. ; Weber, A. ; Abou-Ras, D. ; Kötschau, I. ; Schock, H.-W. ; Schurr, R. ; Hölzing, A. ; Jost, S. ; Hock, R. ; Voß, T. ; Schulze, J. ; Kirbs, A.: Cu_2ZnSnS_4 thin film solar cells from electroplated precursors: Novel low-cost perspective. In: *Thin Solid Films* 517 (2009), Nr. 7, S. 2511 – 2514. – Thin Film Chalogenide Photovoltaic Materials (EMRS, Symposium L). – ISSN 0040–6090

[40] Moritake, N. ; Fukui, Y. ; Oonuki, M. ; Tanaka, K. ; Uchiki, H.: Preparation of Cu_2ZnSnS_4 thin film solar cells under non-vacuum condition. In: *Phys. Status Solidi (c)* 6 (2009), Nr. 5, S. 1233–1236. – ISSN 1610–1642

[41] Katagiri, H. ; Jimbo, K. ; Moriya, K. ; Tsuchida, K.: Solar cell without environmental pollution by using CZTS thin film, 2003, S. 2874–2879

[42] Kobayashi, T. ; Jimbo, K. ; Tsuchida, K. ; Shinoda, S. ; Oyanagi, T. ; Katagiri, H.: Investigation of Cu_2ZnSnS_4-Based Thin Film Solar Cells Using Abundant Materials. In: *Japanese Journal of Applied Physics* 44 (2005), Nr. 1B, 783-787

[43] Scragg, J. J. ; Dale, P. J. ; Peter, L. M.: Towards sustainable materials for solar energy conversion: Preparation and photoelectrochemical characterization of Cu_2ZnSnS_4. In: *Electrochemistry Communications* 10 (2008), Nr. 4, S. 639–642

[44] Tanakaa, T. ; Yoshida, A. ; Saiki, D. ; Saito, K. ; Guo, Q. ; Nishio, M. ; Yamaguchi, T.: Influence of composition ratio on properties of Cu_2ZnSnS_4 thin films fabricated by co-evaporation. In: *Thin Solid Films* 518 (2010), Nr. 21, S. S29–S33

[45] Tuttle, J. ; Contreras, M. ; Albin, D. ; Noufi, R.: Physical, chemical and structural modifications to thin-film $CuInSe_2$-based photovoltaic devices. In: *22nd IEEE Photovoltaic Specialists Conference (PVSC)*, 1991, S. 1062–1067

[46] Fernandes, P.A. ; Salomé, P.M.P. ; ; Cunha, A.F. da: Growth and Raman scattering characterization of Cu_2ZnSnS_4 thin films. In: *Thin Solid Films* 517 (2009), Nr. 7, S. 2519–2523

[47] Todorov, T. K. ; Reuter, K. B. ; Mitzi, D. B.: High-Efficiency Solar Cell with Earth-Abundant Liquid-Processed Absorber. In: *Advanced Materials* 22 (2010), Nr. 20, S. E156–E159

[48] Ohring, M.: *The Materials Science of Thin Films*. Academic Press, 1992

[49] Kessler, J. ; Bodegård, M. ; Hedström, J. ; Stolt, L.: Baseline $Cu(In,Ga)Se_2$ device production: Control and statistical significance. In: *Solar Energy Materials and Solar Cells* 67 (2001), S. 61–76

[50] Schroeder, D. K.: *Semiconductor Material and Device Characterization*. 2nd edition. Wiley-Interscience, 1998

[51] Klenk, M. ; Schenker, O. ; Probst, U. ; Bucher, E.: X-ray fluorescence measurements of thin film chalcopyrite solar cells. In: *Solar Energy Materials and Solar Cells* 58 (1999), S. 299–319

[52] Lundberg, O. ; Bodegård, M. ; Malmström, J. ; Stolt, L.: Influence of the Cu(In,Ga)Se_2 thickness and Ga grading on solar cell performance. In: *Progress in photovoltaics: Research and applications* 11 (2003), S. 77–88

[53] Shafarman, W. N. ; Stolt, L.: Cu(InGa)Se_2 Solar Cells. In: Luque, A. (Hrsg.) ; Hegedus, S. (Hrsg.): *Handbook of Photovoltaic Science and Engineering*. Wiley, 2003, Kapitel 13, S. 567–616

[54] Schubert, B. ; Marsen, B. ; Cinque, S. ; Unold, T. ; Klenk, R. ; Schorr, S. ; Schock, H.-W.: Cu_2ZnSnS_4 thin film solar cells by fast coevaporation. In: *Prog. Photovolt: Res. Appl.* (2010). – ISSN 1099–159X

[55] Archer, M. D. (Hrsg.) ; Hill, R. (Hrsg.): *Clean electricity from photovoltaics*. Imperial College Press, 2001

[56] Katagiri, H.: Cu_2ZnSnS_4 thin film solar cells. In: *Thin Solid Films* 480-481 (2005), 426 - 432. – EMRS 2004. – ISSN 0040–6090

[57] Schock, H.-W.: High voltage solar cells by band gap and defect engineering in Cu(In,Ga)(S,Se)$_2$ chalcopyrite semiconductors. In: *Proceedings of the 16th European Photovoltaic Solar Energy Conference*, 2000, S. 304–308

List of Abbreviations

CBD	Chemical Bath Deposition
CIGS	$Cu(In,Ga)(S,Se)_2$
CIS	$CuInS_2$
CTS	Cu_2SnS_3
CZTS	Cu_2ZnSnS_4
EDS	Energy Dispersive x-ray Spectroscopy
KCN	Potassium Cyanide
Mo-SLG	Soda-Lime Glass coated with Molybdenum
QE	Quantum Efficiency
SEM	Scanning Electron Microscopy
SLG	Soda-Lime Glass
TPD	Ternary Phase Diagram
XPS	X-ray Photoelectron Spectroscopy
XRD	X-Ray Diffraction
XRF	X-Ray Fluorescence

List of Figures

1.1 Rise in prices for resources . . . 1

2.1 Available renewable energy . . . 3
2.2 Black body AM0 AM1,5 . . . 5
2.3 Silicon lattice . . . 6
2.4 Energy bands . . . 7
2.5 Band-bending . . . 8
2.6 Space charge region . . . 9
2.7 Band-bending applying voltage . . . 10
2.8 Diode characteristic . . . 11
2.9 Illuminated diode characteristic . . . 13
2.10 Equivalent circuit of a solar cell . . . 14
2.11 Impact of resistances on the diode characteristic . . . 16
2.12 Possible efficiencies for certain bandgaps . . . 18
2.13 CIGS and CZTS cell cross section . . . 19
2.14 Semiconductor compounds . . . 20
2.15 CZTS crystal structure . . . 21
2.16 Ternary phase diagram (secondary phases) . . . 23
2.17 Ternary phase diagram regions . . . 24
2.18 CZTS efficiency development . . . 27

3.1 Spark tester . . . 34
3.2 Electron-matter interaction . . . 36
3.3 QE squared . . . 41

4.1 Zn deposition rate for different powers . . . 44
4.2 XRD of Zn, Cu/Sn and Cu/Sn/Zn films . . . 45
4.3 XRD of ZnS precursors . . . 47
4.4 Sn loss . . . 51
4.5 Surface features . . . 56
4.6 Grain sizes for different TPD regions . . . 58
4.7 Grain sizes for two Cu-poor samples . . . 59
4.8 Comparison voids for different TPD regions . . . 60
4.9 Layering: TPD . . . 61
4.10 Layering: Cross section . . . 62

4.11 Layering: Top view 63
4.12 Layering: Zoom in 63
4.13 Layering: Comparison 64
4.14 Impact of ZnS: General 65
4.15 Impact of ZnS: Matrix (cross sections) 67
4.16 Substrate comparison 70
4.17 XRD SnS2-signal 72
4.18 XRD CuS-signal 72
4.19 TPD ordered by composition 76
4.20 Influence of Zn content on efficiency 76
4.21 Pseudo binary tie line 77
4.22 Correlation grain size and efficiency 80
4.23 Correlation voids and efficiency 81
4.24 Correlation compactness and efficiency 82
4.25 QE data of most samples 84
4.26 QE comparison 3 samples 86
4.27 QE comparison 3 samples: cross sections 87
4.28 Band gap determination 89
4.29 IV measurements: good and bad samples 91
4.30 FF plotted against Zn content 91

A.1 Energy consumption 111
A.2 Thin film solar cells fraction 111
A.3 XPS metal precursor on Si and Mo 113
A.4 XPS ZnS precursor on Si and Mo 114
A.5 XPS concerning MoS_2 115

List of Tables

2.1 Deposition methods 28

3.1 Substrate composition comparison 38

4.1 All sample data 50
4.2 Reproducibility 54
4.3 Voids table 60
4.4 Sample matrix 66
4.5 Average efficiency ZnS vs metal 79
4.6 Sample matrix efficiency 79

A.1 Sample matrix XPS 112

A Appendix

A.1 Trends in photovoltaics

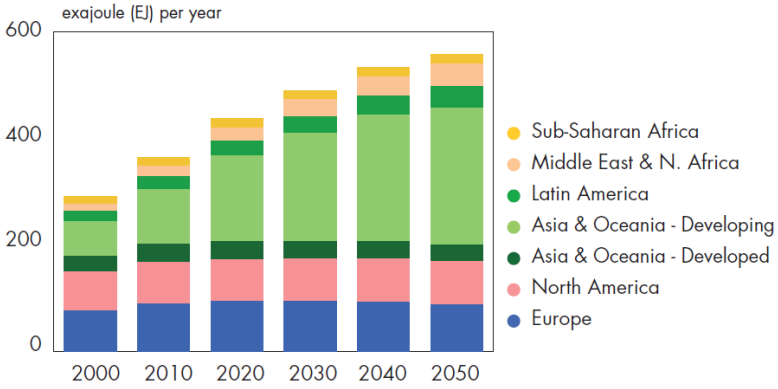

Figure A.1: Predicted increase of worldwide energy consumption. (Shell energy scenario to 2050, http://www-static.shell.com/static/aboutshell/downloads/)

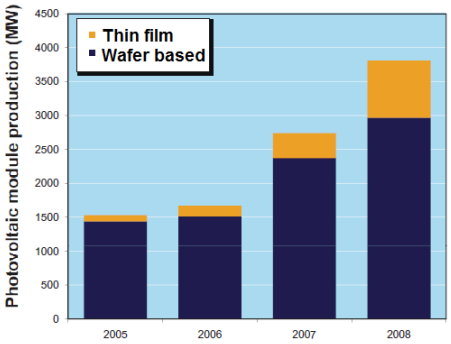

Figure A.2: Market share of thin film solar cells until 2008 (IEA study 2009 "Trends in Photovoltaic Applications", from http://www.iea-pvps.org/products/download/rep1_18.pdf).

A.2 XPS measurements

Precursors

On 4 precursors XPS was performed to reveal possible differences in composition and gradients between metal and ZnS precursors as well as between films on Si and Mo substrates, see Table A.1.

The compositional values from XPS differ strongly from those obtained by EDS. For example, for the metallic precursor seen in Fig. A.3a), the XPS result shows about 60% Cu, while EDS measurements give about 40%. Indeed is the EDS not calibrated either, but confirmed by several measurements and calculations (see chapter 3.2.2.1). For this reason, we do not use XPS measurements for the determination of absolute atomic percentages, since XPS in general is less exact for absolute composition measurements. However, the relative changes in composition can be used assuming all samples of the same material and for different sputtering depths give the same error.

In the following we compare 4 samples: A is a metal precursor on Si, B the same on Mo, C is a sulphur containing precursor on Si and finally D is the same on Mo. By this we can get an overview of the homogeneity of the precursors, and also study possible differences for different substrates.

In Fig. A.3a) we see sample A, a metal precursor on Si. Near the surface[1] a strong decrease of the Cu signal (almost down to 0) is accompanied by a similar strong increase of the Sn-signal. The Zn signal shows a strong increase at the very surface, but reaches a plateau very soon. These gradients indicate that the very surface is very Cu-poor and Zn-rich. A bit deeper, but still near the surface, the film appears Cu-poor and Sn-rich. Despite these gradients near the surface, the overall impression of the precursor is that the composition is very uniform within the film.

Not visible in this graph is that the film was almost oxygen free, only the surface showed a slight increase in signal intensity and indicates the presence of Zn- and Sn-oxides.

The next graph, Fig. A.3 b), shows a precursor from the same run as a but on molybdenum. Qualitatively – and to a certain extend also quantitatively – the picture shows

Substrate \Precursor type	Metallic	ZnS
Silicon	A	C
Molybdenum	B	D

Table A.1: Sample matrix used for XPS to study differences between metallic and ZnS precursors as well as precursors on the substrates silicon and molybdenum.

1 Unfortunately, it was not possible to determine the sputter depth. Sometimes it was sputtered through down to the substrate (which could be seen by an increase of the signal of the substrate material), but otherwise expressions like "near the surface" or "in the bulk" have to be understood relatively to the distance (indicated by the sputter time) that has been sputtered in the particular sample.

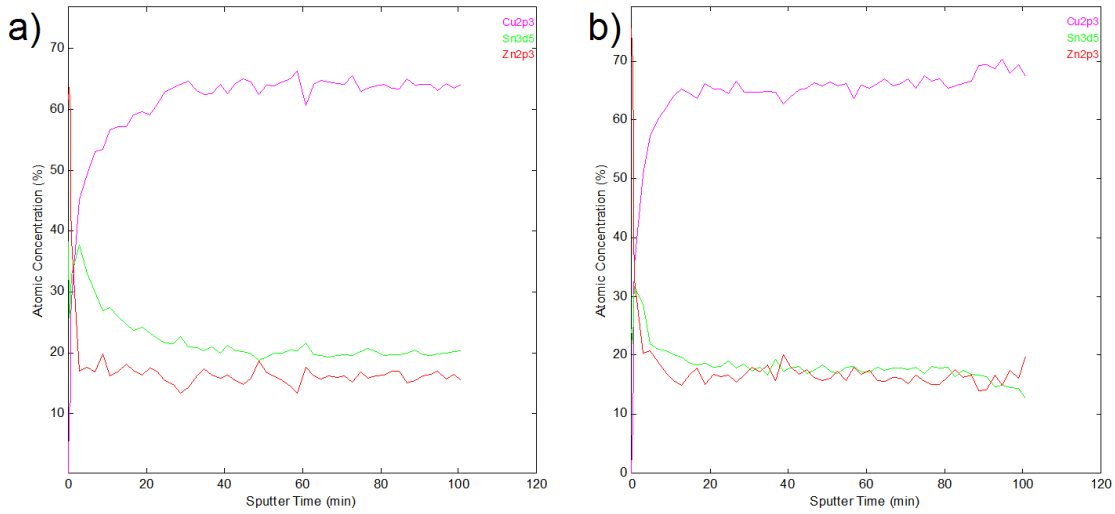

Figure A.3: a) Metal precursor on silicon substrate (sample A). The film shows uniform composition, only the surface has gradients (Cu-poor and Zn-rich). b) Metal precursor on molybdenum substrate (sample B). The film shows very similar composition to B (uniform composition besides at the surface).

the same result. Again the surface is Cu-poor and Zn- or Sn-rich, respectively; just the gradients start probably a bit closer to the surface. Except of that, this comparison indicates that precursors on Mo and on Si can be treated as equal, considering gradients and composition.

Sample c can be seen in Fig. A.4 a). Here, Si is used as a substrate, but the precursor is from the second sputter series, i.e. it contains sulphur. Again, apart from the surface, the elements Zn, Sn and here also S, show good homogeneity. Only Cu seems to reveal a slight decrease of some atomic percent towards the surface. At the surface, the Sn content increases rapidly. However, the Cu-, Zn- and S-concentration decreases, but in a minor degree than the Sn-increase. Hence, this sample has a Sn-rich surface and a quite homogenous bulk.

The last picture in this consideration (Fig. A.4 b)) shows the data of sample D, produced together with sample C but on Mo instead of Si. Note the different scale compared to Fig. A.4 a) due to a spike in the data caused by a measurement error. The overall impression of this sample is the same as for C: Zn, Sn and S lie on the same level at around 20%, while the Cu-concentration lies around 45% and decreases slightly down to roughly 40%. Again, the Sn content increases strongly very near the surface, connected with a decrease of the other elements. This comparison indicates (like for the other two samples), that precursors on Si and Mo can be treated as equal, both considering gradient and composition.

Not yet discussed, as it cannot be seen from these pictures where only the sputtered

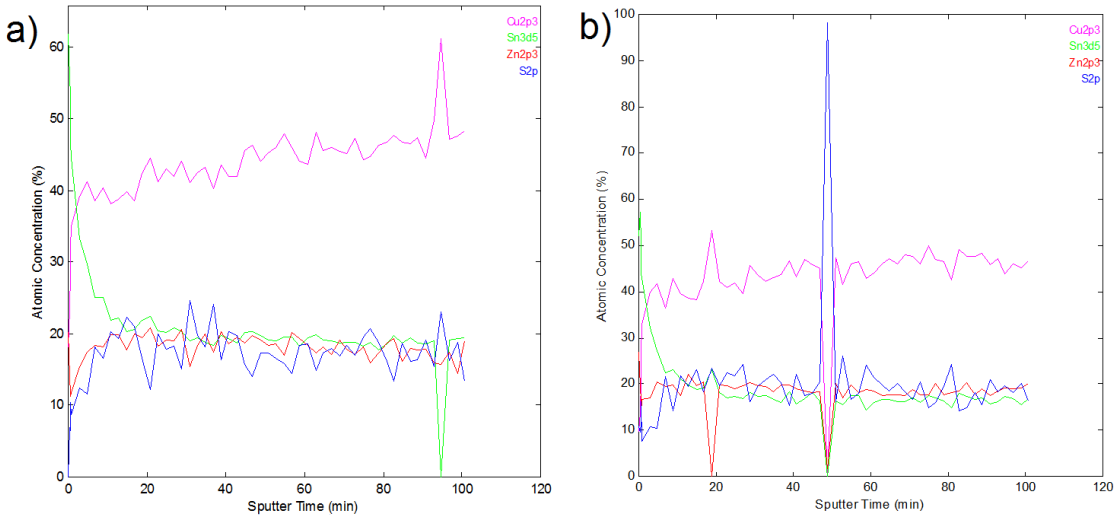

Figure A.4: a) ZnS precursor on silicon substrate (sample C). Except of the surface the composition is constant within the film. For Cu content there might be a slight decrease towards the surface, though. b)ZnS precursor on molybdenum substrate (sample D). The film shows very similar results to C in a).

elements are shown, is the content of oxygen. Two ZnS samples were studied and showed the same oxygen level. It turns out to be higher in the S-containing precursor through the whole film. This indicates that the ZnS-containing precursors are less dense than the metal one. That is not surprising, as Zn has an almost twice as high density than ZnS (Zn: 7,1 g/cm^3, ZnS: 4,1 g/cm^3; [23]). The higher porosity allows the oxygen to diffuse into the film even after finalizing the deposition.

Another aspect that can be observed is that the metallic precursors show Sn- and Zn-oxides at the surface, which can be seen from the shift of the elemental peaks. The peak position in XPS can be shifted by changes in chemical bonding environment of the atom. In this way compounds like in this case oxides can be determined.

The presence of oxides at the surface is not surprising as the samples have not been stored in vacuum, but should not have any strong impact on the sulphurization.

Molybdenum sulfide

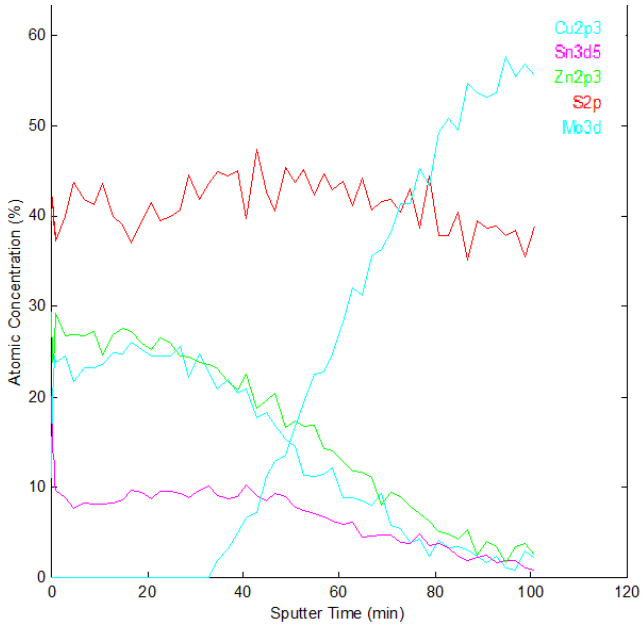

Figure A.5: XPS data showing the increase of the Mo-signal (light blue) attended by a decrease of the metal signals. The sulphur signal remains meanwhile almost the same and decreases only sligthly. That indicates the presence of molybdenum sulfide.

Acknowledgments

First of all I want to thank Prof. Marika Edoff, Dr. Mikhail Fonin and Prof. Giso Hahn, who offered me the possibility to do this thesis in Uppsala, for what I'm deeply grateful.

Furthermore I thank my supervisors Lotten Platzer–Björkman and Tomas Kubart for many fruitful discussions and supporting my work a lot. I thank Lotten for doing XPS, XRD and QE measurements, and Tomas for help with sputtering, EDS and searching for blueberries.

I thank Jonathan Scragg for helping me with SEM and for several useful discussions about CZTS and the ternary phase diagram.

Moreover I want to thank the whole group of the Ångström Solar Center for a nice year in a pleasant working atmosphere and a lot of '15 o'clock fikas'. In particular I want to bring out the help of Uwe Zimmermann for always answering all questions covering the range from physics to planting, and Sebastian Schleußner who helped me a lot with any concern in the stressful final period of my writing.

Manuel Brendle is acknowledged gratefully for troubleshooting Latex and proof reading my thesis.

Großer Dank gebührt vor allem meinen Eltern. Sie haben mich das ganze Studium über unterstützt und bei jeder Entscheidung hinter mir gestanden, und mir damit meinen Traum von Schweden erst möglich gemacht.

Und abschließend, aber bestimmt nicht als Letzter, möchte ich von ganzem Herzen Hanna danken, die sich nicht nur zwei Tage und Nächte um die Ohren geschlagen hat, um Fehler in der Diplomarbeit aufzudecken, sondern mir vor allem ganz viel Kraft und Halt in schwierigen Momenten gegeben hat!